UNSW Thesis:

Detection of Subsurface Cracking Depth through Electrical Resistivity Anisotropy

By

Anna-Katrin Greve

A THESIS SUBMITTED FOR THE DEGREE OF

DOCTOR OF PHILOSOPHY

Water Research Laboratory

School of Civil and Environmental Engineering,

The University of New South Wales, Sydney, Australia.

December 2009

Originality Statement

'I hereby declare that this submission is my own work and to the best of my knowledge it contains no materials previously published or written by another person, or substantial proportions of material which have been accepted for the award of any other degree or diploma at UNSW or any other educational institution, except where due acknowledgement is made in the thesis. Any contribution made to the research by others, with whom I have worked at UNSW or elsewhere, is explicitly acknowledged in the thesis. I also declare that the intellectual content of this thesis is the product of my own work, except to the extent that assistance from others in the project's design and conception or in style, presentation and linguistic expression is acknowledged.'

Signed:_____

Abstract

To date, an understanding of crack dynamics has been hampered by the lack of techniques to observe or monitor crack dynamics below the soil surface. This study introduces a new technique for the detection of subsurface cracks that relates the development of soil cracks to changes in the electrical anisotropy of the soil. Here electrical anisotropy is defined as the ratio of the apparent resistivity measured with the alpha and the beta square array. While measurements of electrical anisotropy have been carried out at the soil surface, here an electrode array is proposed that allows anisotropy measurements at regular depth intervals throughout a soil profile. Four strings of electrodes are installed vertically at the corners of a square so that square array measurements can be made on a series of coplanar electrode squares using one electrode from each of the four vertical strings.

Anisotropy responses to different crack scenarios were simulated numerically before measurements were carried out in the laboratory and in the field. In the laboratory anisotropy measurements were carried out in a sand filled lysimeter with a plastic sheet introduced to represent an electrically insulating crack. Measurements were then repeated in a cracking soil filled lysimeter. Finally, measurements were made at two field sites, where flood irrigated sorghum and cotton were grown on cracking soil. For the field measurements, a 3D electrical resistivity tomography routine was designed that could be run with the same electrode arrangement used for the anisotropy measurements. Time-lapse measurements of 3D electrical resistivity allowed tracking of water infiltration and gave information about the extent of soil cracking. This was then compared to the anisotropy results.

The numerical simulations, the laboratory and field measurements all demonstra-

ted that the lateral and vertical extent of cracking in a soil profile strongly influences the electrical anisotropy and that a well developed anisotropy profile allows determination of a cracking depth range. Soil moisture changes after crack closure only have a minor influence on the anisotropy as has the presence of sorghum and cotton roots. It is concluded that electrical anisotropy profiles are a valuable tool for monitoring crack dynamics within a soil profile.

Contents

List of Figures

List of Tables

Acknowledgements

There is a huge amount of people, without whom this study would have been significantly less enjoyable or not possible at all; a big 'thank you' to all of them!

In particular I would like to thank my supervisors Ian Acworth and Bryce Kelly for creating this opportunity and for their support along the way; Andrew McCallum, Bea Giambastiani and Gabriel Rau for being wonderful office mates and great supporters along the way; Martin Andersen for always having an open door; John Hart for lots of help and input into the design of the resistivity probes and the entire WRL team for creating a great work environment.

Furthermore, I had lots of help with field work in sun, mud, and rain, which was essential for this study. Thank you to Andrew, Sebastien and Amalia, field days would have been much longer and harder without you guys; and thank you to Ken and Sue Crawford for providing a home away from home for all of us. Access to field sites and support during field days was provided by the Eathers at the Maules Creek site and by Tony Nadelko and Anthony Ringrose-Voase at the ACRI site, thank you!

And of cause there are my loved ones, without whom this work would never have happened; my loved ones in Germany, who gave me the courage and support to go into the big world and find my way to this place; and my loved one in Australia without whom I never would have come here.

This study was funded by the Cotton Catchment Community CRC and the Cotton Research and Development Cooperation.

List of Publications

The following publications were produced as part of this research:

Greve, A.K., Acworth, R.I., Kelly B.F.J., 2010. Detection of soil cracks by vertical anisotropy profiles of apparent electrical resistivity. Geophysics (in press).

Greve, A.K., Andersen, M.S., Acworth, R.I., 2010. Investigations of soil cracking and preferential flow in a weighing lysimeter filled with cracking clay soil. Journal of Hydrology (Available online: DOI: 10.1016/j.jhydrol.2010.03.007).

Greve, A. K., Acworth, R. I., 3D cross-borehole resistivity tomography to monitor small scale soil moisture changes in the root zone. Submitted to Journal of Hydrology.

Kelly, B.F.J., Acworth, R.I., **Greve, A.K.**, Monitoring deep drainage beneath irrigated cotton using two-dimensional surface electrical resistivity tomography. Submitted to Journal of Applied Geophysics.

Acworth, R.I., **Greve, A.K.**, 2009. System, apparatus and method for measuring soil moisture content. International Patent Publication Number WO 2009/117784 A1.

Greve, A.K., Acworth, R.I., 2009. Monitoring soil moisture changes and deep drainage pathways, 37th IAH Congress 6-10 Sep. 2009, Hyderabad, India.

Greve, A.K., Acworth, R.I., 2009. Electrical resistivity methods to monitor soil moisture changes and deep drainage, Cotton Catchment Communities CRC Science Forum, 17-19 Aug. 2009, Narrabri, Australia.

Foley J., Silburn M., **Greve A.K.**, 2009. Resistivity imaging across native vegetation and irrigated vertosols of the Condamine catchment—a snapshot of changing regolith water storage, 19th World Congress of Soil Science, 1-6 Aug. 2010, Brisbane, Australia. Published on CD ROM.

Greve, A.K., Acworth, R.I., 2008. Monitoring depth of soil cracking in irrigated fields based on directional dependence of electrical current flow, XXXVI IAH Congress 26 Oct.-1 Nov. 2008, Toyama, Japan.

Greve, A.K., Acworth, R.I., Kelly, B.F.J., 2008. Monitoring soil moisture changes with 3D resistivity tomography, AGU, 89(23), Western Pacific AGU meeting, Cairns 28 Jul. - 1 Aug. 2008, Abstract H43A-04.

Greve, A.K., Acworth, R.I., 2007. Dynamics of soil cracking & borehole resistivity tomography, Cotton Catchment Communities CRC Science Forum, 8-9 Aug. 2007, Narrabri, Australia.

Chapter 1

Introduction

1.1 Background

Crop irrigation accounts for nearly 60 % of Australia's water consumption (Trewin, 2006a,b). The majority of irrigated agriculture is located on fine grained cracking soils as their high nutrient content and water holding capacity support high yielding crops and profitable farming. Due to the high clay content, irrigation on these soils was long assumed to be very efficient and the losses due to deep drainage were assumed negligible (Hearn et al., 1997; Vervoort et al., 2003). In recent years, evidence of deep drainage in cracking clay soils became widely accepted, yet estimates of its magnitude still vary. Silburn and Montgomery (2001) reviewed the available literature on deep drainage estimates in Australian cotton growing districts and indicated that it could be as high as 3 ML/ha per year. Smith et al. (2005) examined 79 flood irrigations on cracking clay soils in cotton growing areas of southern Queensland. Losses to deep drainage averaged 0.425 ML/ha per irrigation, representing an annual loss of up to 2.5 ML/ha throughout the growing season.

These large potential water losses, are an incentive to improve our understanding of deep drainage processes in cracking soils. Best management practise for irrigation includes the advice to reduce deep drainage by not exceeding the soils water deficit during an irrigation (Smith et al., 2005; Ringrose-Voase, 2008). However, in cracking soils a second deep drainage mechanism can occur that takes place at the opposite

end of the soil moisture spectrum. Preferential flow through soil cracks can rapidly move irrigation water into deep parts of the soil profile and can quickly transport solutes and agrochemicals through the unsaturated zone (Beven and Germann, 1982; Kosmas et al., 1991; Harris et al., 1994; Bronswijk et al., 1995; Lin and McInnes, 1995; Tuong et al., 1996). This not only reduces water use efficiency during irrigation, but also lowers the capacity of the unsaturated soil profile to store, adsorb, and transform potential pollutants before these reach surface or ground waters. To mitigate these problems and to allow the most appropriate irrigation scheduling, a sound understanding of crack dynamics is needed. So far, such an understanding has been fundamentally hampered by a lack of available techniques to observe or monitor crack dynamics below the soil surface.

While surface crack dynamics can be measured directly (Ringrose-Voase and Sanidad, 1996), *in situ* measurements of cracking depth have been limited to the digging of soil pits (Bouma and Dekker, 1978) or the insertion of wire or measuring tape into cracks (Zein el Abedine and Robinson, 1971; Tuong et al., 1996; Kishne et al., 2009). Soil pits clearly destroy the site and prohibit time lapse measurements. Measuring the cracking depth using wire or a measuring tape is labour intensive, disturbs the crack walls and becomes unreliable if the cracks divert from the vertical or the soil is too soft to provide noticeable resistance.

1.2 Scope of Work

The aim of this study is the development of a non destructive method to monitor crack development below the soil surface. To do so, a novel method is proposed and evaluated through a series of numerical modelling, laboratory and field experiments. The proposed method is based on DC resistivity measurements carried out with the square electrode array, which allow the monitoring of changes in directional dependence of current flow during crack growth. While square array measurements have successfully been used at the ground surface, this study introduces an electrode arrangement that allows square array measurements at regular depth intervals throughout

a soil profile. Based on these measurements, profiles of electrical resistivity anisotropy can be generated, which give information about the development of subsurface cracks.

First, the mechanisms of soil cracking and infiltration in cracked soil, which will be observed in the experimental sections of this study, are reviewed. This is followed by an introduction to previous work on crack detection through electrical resistivity measurements leading to the proposed method for crack detection in this study.

Throughout Chapters 3 and 4, the proposed method of crack detection through anisotropy profiles is assessed in numerical and laboratory studies. First the detection of simple crack arrangements consisting of one and two cracks is investigated, followed by the testing of the detectability of natural crack networks.

An effective evaluation under field conditions requires additional measures of the extent of soil cracking to compare to the results of the anisotropy profiles. As the lack of such methods is the very reason for this study, Chapter 5 describes the development of an additional indicator of subsurface soil cracking: 3D electrical resistivity tomography (ERT) that is carried out with the same electrode arrangement used for the measurement of anisotropy profiles. 3D ERT gives an indication of the extent of soil cracking in two ways. Time lapse series of 3D ERT images throughout an irrigation event allow tracking of preferential flow through soil cracks, which gives information about the extent of subsurface cracking. Furthermore, unusually high resistivities in an ERT image can be related to the presence of soil cracks, and unusually high resistivity changes during an irrigation can be related to crack closure. Finally, the techniques are applied in two field experiments described in Chapters 6 and 7.

In the field experiments, crack development in two different soils under two different crops (sorghum and cotton) is described. In addition to providing data sets collected under different conditions the two field experiments allow comparison with different sets of auxiliary data, which were collected at the two field sites. Results of the field experiments confirm the suitability of the proposed method for crack detection. Furthermore, it is shown that the proposed electrode arrangement can successfully be used to carry out 3D ERT, which allows monitoring of spatial and

temporal soil moisture variations within the root zone.

It is acknowledged that the presented thesis does not follow the conventional thesis structure. Rather than presenting the study with a single theory, methods and results section, the thesis is divided into chapters that describe the testing of the proposed method for crack detection under increasingly complex conditions. This format was chosen to convey the logic that was behind the succession of experimental setups, as results of the more controlled experiments in the earlier chapters lead to the experimental designs in the later chapters. While an introduction to the related literature and theory is given in Chapter 2, additional theory is introduced if it is needed to explain the reasoning for the experimental design in later chapters.

Chapter 2

Cracked Soil & Electrical Resistivity

2.1 Cracked Soil

2.1.1 Water Infiltration into Cracked Soil

Soil shrinkage was first investigated by Tempany (1917) and Haines (1923). Stirk (1954) pioneered work on water entry into cracked soil and concluded that cracking, severe enough to affect water entry, would not occur in continuously irrigated agriculture, as the soil water content would not get low enough to produce significant soil cracks. It might be due to this conclusion that much of our knowledge on preferential flow in cracked soils was derived under rainfall conditions and not during irrigation events. The importance of preferential flow in cracking soils during rainfall has been highlighted in several studies (Bouma et al., 1978; Hoogmoed and Bouma, 1980; Bouma, 1981; Beven and Germann, 1982; Van Stiphout et al., 1987; Bouma, 1990; Bronswijk et al., 1995; Tanton et al., 1996; Hendriks et al., 1999). All of these studies show that the importance of bypass flow increases with increasing rainfall intensity. Considering the high application intensities during a flood irrigation, this suggests significant preferential flow during flood irrigation of cracked soil. Indeed, Mitchell and Vangenuchten (1993) confirmed that water flowing into cracks during flood irrigation accounted for the majority of infiltrating water. During irrigation of two fallow fields, the crack filling water accounted for 63 and 58 % of the total infiltra-

(a) (b) (c)

Figure 2.1: Surface cracking in continuously irrigated agricultural plots.

ting water and for 74 % during irrigation of an alfalfa plot. Austin and Prendergast (1997) found that the infiltration during crack filling was inversely proportional to the antecedent soil water content and that 49 % of infiltrating water infiltrated within the first 60 seconds of water arrival. Yasuda et al. (2001) demonstrated that the water distribution after flood irrigation on cracked soils was highly variable, with only the upper few centimetres of a profile being homogeneously wetted, whereas deeper layers showed preferred wetting along preferential flow paths.

The mechanism of infiltration into cracked soil during rain or sprinkler irrigation is: initial absorption of the water by the soil prisms followed by deep penetration along vertical cracks and fauna channels as soon as the application rate exceeds the decreasing capacity of the soil prisms to absorb liquid. Once the liquid can not be absorbed by the soil, free water becomes available at the surface and starts flowing into the cracks (Bouma and Dekker, 1978). During flood irrigation, free water is immediately available, allowing instant flow into the cracks. The contact area between the by-passing flow and the soil matrix is only a small fraction of the total area of vertical macropores (Bouma and Dekker, 1978; Booltink and Bouma, 1993). This, combined with the low hydraulic conductivity in fine grained soils and the short contact time between by-passing water and the crack walls, leads to the conclusion that lateral infiltration into the soil pads through the crack walls is very small (Hoogmoed and Bouma, 1980; Bronswijk, 1988). Water movement in cracking soils occurs mainly in macropores whereas the soil solution within the micropores remains largely immobile (Bouma and Anderson, 1977; Steenhuis et al., 1988).

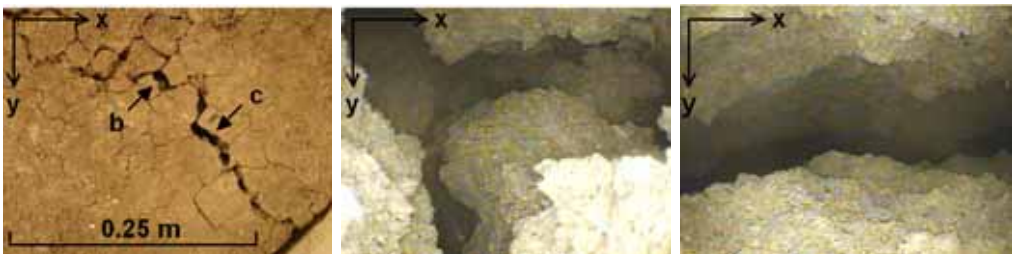

(a) (b) (c)

Figure 2.2: a: photograph of a 6 mm wide surface crack with the arrows pointing to two insertion points of a videoscope; b: photo taken with a videoscope at insertion point b at 450 mm depth; and c: another photo at the same depth with the videoscope inserted at point c.

With the knowledge that soil cracks, if present, strongly influence the infiltration during a flood irrigation, it becomes necessary to revisit the conclusion by Stirk (1954) that cracking severe enough to influence the water entry will not occur in continuously irrigated plots. A visit to any continuously irrigated plot on cracking soil within the Murray-Darling Basin in Australia, allows the observation of well developed surface cracks as shown in Figure 2.1. What is less easily observable is how far these cracks extend into the soil profile and hence how deep the water that enters them will flow into the soil. Greve et al. (2010) investigated soil cracks with a videoscope and showed that surface cracks of 6 mm reached through the entire investigated profile of 450 mm depth as shown in Figure 2.2. This significant depth of seemingly small surface cracks emphasises the potential of soil cracks as preferential flow paths and hence the importance of considering the formation of soil cracks during irrigation scheduling.

2.1.2 Formation of Soil Cracks

Soil cracks are formed due to soil shrinkage. Under unconfined conditions, swelling and shrinkage of a soil is assumed to be three dimensional and isotropic (Bronswijk, 1988). In deeper soil layers, overburden pressure modifies shrinkage and swell behaviour (Groenevelt and Bolt, 1972; Talsma, 1977) and will cause swelling to be primarily one dimensional. Here, soil alongside a crack will preferentially expand into the open

space of the void (White, 1972). Once the voids are closed or if no voids are present, stresses that built up due to further swelling are released by upward expansion of the soil. Such local upward expansion will result in shear planes between soil regions and hence in the formation of slickensides.

During soil drying one can distinguish between the following shrinkage phases (Haines, 1923; Stirk, 1954):

- Normal shrinkage: The soil aggregates remain fully saturated; thus the loss of water is equal to the decrease in volume.
- Residual shrinkage: Air enters the aggregate pores; therefore the loss in water is greater than the decrease in volume.
- Zero shrinkage: The soil aggregates have reached their densest form, no more shrinkage occurs and further loss of water is offset by an increase of air in the aggregates.
- Sometimes a fourth shrinkage stage occurs in the field - structural shrinkage: This occurs in very wet soils when water is lost from large pores. In this stage the shrinkage is negligible while water loss can be very high.

If the shrinkage stress exceeds the local tensile strength of the soil, the soil fractures. The stress along the fracture concentrates at the tip of the crack causing the crack tip to propagate until the stress is reduced below the local tensile strength of the soil (Freud, 1998). The distribution of tensile strength in the soil and the stresses due to shrinkage of the material are non-homogeneous and their interaction greatly influences the location and orientation of the resulting cracks. Many factors have been named to directly or indirectly influence tensile strength and shrinkage behaviour and thus the width, shape, depth and distribution of resulting cracks. The tensile strength in soils increases with the specific surface area of the resulting crack walls (White, 1972). As crack walls consisting of fine grained material have a larger specific surface area than walls consisting of larger grains, the tensile strength is higher in finer grained soils (Gill et al., 2004). Soil moisture content was also found to influence a soil's tensile

strength, with an increase in moisture content resulting in decreased resistance against fracture (Johnston and Hill, 1944; Murdoch, 1993). Several authors (Groisman and Kaplan, 1994; Colina and Roux, 2000a; Chertkov, 2000; Shorlin et al., 2000) have reported that the final crack spacing is essentially controlled by the thickness of the cracking layer, which is determined by the drying depth (White, 1972). In thick layers a larger shrinkage region is needed for the layer to reach the critical stress for fracture. Different crack depths and spacing's in the field result in several small surface soil prisms to be joined together at their base to form larger prisms in the subsurface (White, 1970). Lecocq and Vandewalle (2002) observed that fast drying favours crack nucleation rather than deformation for relaxation of the shrinkage stress. Therefore, fast drying soil should develop a larger number of small cracks while slow drying results in fewer and larger cracks. Plant root systems can influence soil cracking due to plant specific water abstraction patterns in the root zone (Johnston and Hill, 1944) and a plants canopy can influence the drying rate by protection from direct sunlight (White, 1970). Lima and Grismer (1992) and Waller and Wallender (1993) observed that the width and total area of cracks increased with the soil salinity and Sleeman (1963) reported that cracks are wider spaced in Ca-saturated clays than in Na-saturated clays. Colina and Roux (2000a) reported that the time of the first crack appearance and of the end of crack development are directly proportional to the sample thickness. Discordance exists about whether cracks reappear in the same location as in previous desiccation periods. Based on field observations, White (1970, 2001) affirms the reappearance of cracks. He argues that the location of cracks is determined by differences in tensile strength and cracks will reform along planes of weakness. During closure of cracks the tensile strength at the crack location is reduced even further by the pressure that is created once the crack walls move towards each other. The pressure pushes coarse grains from the crack walls back into the soil matrix and smoothes the crack walls. In the next drying period the formation of a new crack at the same location is more likely because the energy used for fracture opening is lower as if the crack had to go around individual gains. Another factor favouring

crack reappearance according to White (2001) is that cracks at depth, that did not close during wetting, due to limited moisture application, act as a template for the formation of new cracks. Waller and Wallender (1993) confirmed the reappearance of cracks in an experiment in an irrigated field while Wells et al. (2003) reported that the crack locations during simulated rainfall changed between desiccation periods. Greve et al. (2010) suggested that these seemingly contradictory observations might be due to the different types of water applications, they observed that flood irrigations favoured crack reappearance, while simulated rainfall resulted in alternating crack locations.

The complexity of soil and moisture parameters that influence crack formation in natural conditions has so far prevented the development of a widely accepted model to simulated crack development and particularly cracking depth. Chertkov and Ravina (1998) developed a probabilistic model to predict the geometry of steady state crack networks that develop after long drying periods. This approach requires the maximum cracking depth as an input parameter. Chertkov (2000) estimated this maximum cracking depth of a steady state crack network based on the spacing of the surface cracks. To allow the simulation of transient crack network characteristics, several recent studies have focused on modelling the shrinkage characteristics of a soil (Chertkov and Ravina, 2000; Chertkov, 2003; Boivin et al., 2004; Peng and Horn, 2005; Boivin et al., 2006; Cornelis et al., 2006; Chertkov, 2007; Boivin, 2007). However, the step from successful simulation of soil shrinkage to the simulation of crack network development within a heterogeneous soil profile under vegetation still has to be made. Progress in this field has so far been hampered by the lack of field data and a lack of available field techniques to monitor crack dynamics below the soil surface. Improving our understanding of crack dynamics, requires an *in situ* method to monitor subsurface cracks in the field.

2.2 Crack Detection with Electrical Resistivity

2.2.1 Electrical Resistivity Tomography

Measuring the flow of electrical current through the subsurface can provide rapid and useful information about physical and chemical properties of the soil. Soil electrical resistivity is a function of a variety of parameters including: grain shape, size and mineralogy of the soil solids, porosity, pore size distribution, pore connectivity, water content, soil solution electrical resistivity and temperature. Soil fractures also alter the resistivity of a material, so that resistivity measurements are a promising method to monitor crack development in the subsurface.

In the electrical resistivity method, a low frequency alternating current is applied to the ground and the potential difference between two points is measured. The current (I) is applied by 2 electrodes (C_1 and C_2) and the resulting voltage (ΔV) is measured between a second pair of electrodes (P_1 and P_2). The apparent electrical resistivity (ρ_a) is obtained by multiplying the resistance ($R = \Delta V/I$) by a geometric factor (K), which accounts for the relative distances of the C and P electrodes, both to each other and to the ground surface.

The apparent resistivity that is measured with the four electrodes is a weighted average of the electrical resistivities in the region through which the current travels. A problem of non-uniqueness arises from the fact that an infinite number of resistivity combinations can give rise to the same ρ_a. To limit the non-uniqueness, a large number of overlapping measurements are taken and interpreted simultaneously. By sequentially applying currents and measuring potentials at different locations and over different distances a variety of ρ_a values are measured, which reflect the variation of the electrical resistivity in the subsurface. To determine the true resistivity distribution in the subsurface, these multiple ρ_a are then inverted by an iterative inversion and forward modelling process (Loke, 1996-2004). A further reduction of the non-uniqueness is achieved through the use of inversion constraints, such as the smoothness constraint in Occams inversion (deGroot Hedlin and Constable, 1990),

which aims at finding the smoothest possible solution that still fits the data within a predefined error threshold.

Electrical resistance measurements have long been used in the material sciences to investigate crack growth in metal. For a constant current in a metal, the voltage drop across the crack plane is measured and related to the growth of single (Johnson, 1965; Saxena, 1980) or multiple fractures (Tada et al., 1997). More recently this approach has been extended to detect crack formation in concrete (Reza et al., 2004).

In environmental science, crack detection has been focused on fractures in hard rock. Here fracture detection has mainly occurred indirectly by investigating the migration of solute plumes. Slater et al. (1997) used cross borehole measurements in a coastal limestone during salt water intrusion. By monitoring resistivity changes relative to the background they were able to locate the flow pathways through the lime stone fractures. Rugh and Burbey (2008) used time lapse surface measurements to monitor the migration of a saline tracer in a fractured rock aquifer and showed that the geologic structures had a significant effect on groundwater recharge in the investigation area. Nimmer et al. (2007) carried out surface and cross borehole resistivity tomography to detect the dilution of a conductive potassium chloride plume during injection of tap water in a fractured rock. They found that surface measurements were useful for detecting the general pattern of water movement. However, surface measurements could not distinguish between individual fractures and fracture zones, as cross borehole ERT was able to do.

Resistivity measurements have also been used to detect preferential flow in soils, which can give indirect information about soil cracking. Daily et al. (1992) successfully used cross borehole tomography to monitor the wetted regions of two infiltration plumes in a complex environment that included cracks. Binley et al. (1996) carried out time lapse electrical resistivity tomography (ERT) and used pixel break through curves (BTC) to determine preferential flow paths of an electrolyte tracer in an undisturbed soil column. If the resistivity distribution of a soil column is monitored over time, the sequences of inverted ERT images of each image pixel can act as a tracer BTC. A time

sequence of ERT images was also used by Slater et al. (2000), who derived a travel time distribution out of the first arrival times in each pixel and thus were able to track preferential flow in a soil column. The work was then extended by Slater et al. (2002) to estimate the fluid conductivities in pixel BTC. Ever since, ERT has been a popular tool for monitoring and quantifying flow and transport characteristics in soil (Looms et al., 2008; Koestel et al., 2008, 2009; Batlle-Aguilar et al., 2009; Deiana et al., 2007).

Direct detection of fractures through ERT has so far been limited to the laboratory. LaBrecque et al. (2004b) used 3D ERT to monitor dry and wet cracks between wet limestone blocks in the laboratory. They found that even though the abrupt changes in bulk resistivity in a fractured system are contrary to the smooth changes expected in an Occams inversion, the location of cracks could still be detected. Yet none of the different electrode spacings allowed interpretation of the shape of the cracks and cracks that were close to each other could not be separated. Dry cracks were easier to detect, as the resulting resistivity anomaly relative to the wet limestone was higher than that caused by wet cracks. Samouelian et al. (2003) carried out 2D surface resistivity measurements in a soil block. They used a minimum electrode spacing of 1.5 cm and found that even small structures such as millimetre cracks cause a significant change in resistivity distribution, yet due to the smoothness constraint in Occams inversion and due to the loss in resolution with depth, they failed to determine the depth of cracking. To improve the detection of crack dimensions in inverted resistivity images, Tabbagh et al. (2007) introduced an inversion approach based on the methods of moments, which provides an interesting alternative to Occams inversion.

Another approach was introduced by Samouelian et al. (2004), who avoided the ambiguity introduced by inversion routines. Rather than detecting soil cracks in inverted resistivity images, Samouelian et al. (2004) used the ratio between the apparent resistivities measured with the square-α and the square-β surface array as a measure of the directional dependence of current flow induced by soil cracks. This seems to be a very promising approach and is discussed in detail in the following section.

2.2.2 The Anisotropy Index

In the square array configuration, which was first introduced by Habberjam (1967), the two current and two potential electrodes that are used to measure the electrical resistivity are arranged to form a square. As in every four electrode configuration, there are 24 (factorial 4) possible arrangements for the electrodes within this square (Carpenter, 1955). However, as swapping the subscripts of P_1 and P_2 or C_1 and C_2, and interchanging the current and potential electrodes does not alter the magnitude of the measured resistance (Carpenter and Habberjam, 1956), only three of the 24 electrode arrangements are considered to be independent. These three arrangements are, by convention, called the α, β, and γ arrays (Figure 2.3). Following this convention ρ_a measured with the α, β, and γ arrays are in the following referred to as ρ_{a_α}, ρ_{a_β} and ρ_{a_γ}. To demonstrate the influence that a soil crack will have on each of these three ρ_a values, the nature of electrical current flow is examined below.

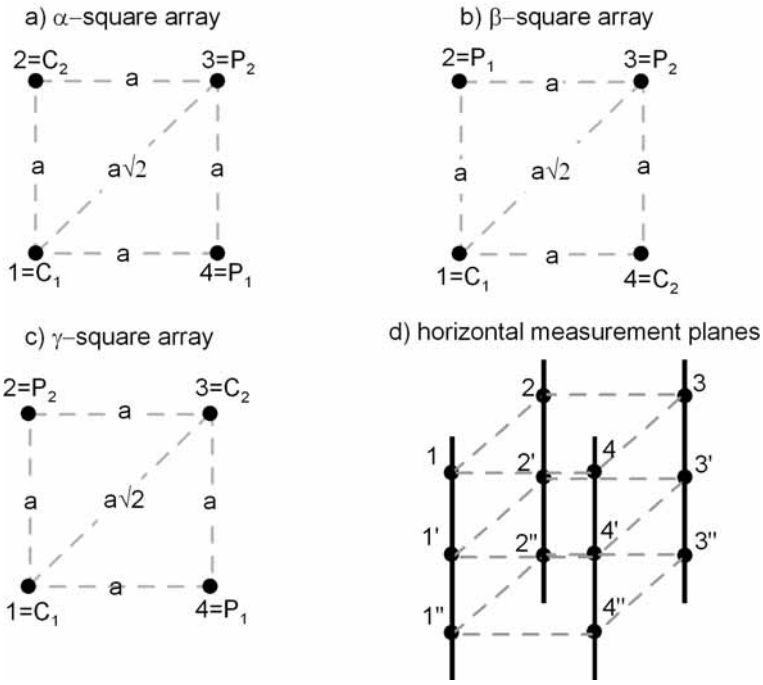

Figure 2.3: a-c: Plan view of a square array with alpha, beta, and gamma configuration; d: Schematic of horizontal measurement planes between the four electrode strings.

In homogeneous and isotropic ground, current flows radially from the source in all directions, forming a spherical surface at each distance. If the current source is

located near the ground surface, the current distribution needs to be corrected for the interface with the non conducting air, as demonstrated in Appendix A. For clarity, the formulations below are made for electrodes that are not influenced by the ground surface. The current density J, at any spherical surface at a distance r from a current source of strength I is therefore

$$J_r = \frac{I}{4\pi r^2}, \tag{2.1}$$

so that Ohm's Law written in terms of the resistivity ρ rather than the conductivity gives the electrical field E as

$$E_r = J_r \rho = \frac{I\rho}{4\pi r^2}. \tag{2.2}$$

The potential ϕ (or voltage) at a distance r from the current electrode is given by the integral of E_r between r and infinity:

$$\phi = \int_r^\infty E_r dr = \frac{I\rho}{4\pi r}. \tag{2.3}$$

Adopting the conventions that $\phi_{x,y}$ is the potential at electrode position x due to a C electrode at position y, and that $\rho_{a_{x,y}}$ is the apparent resistivity in the measurement volume that influences the potential at electrode position x due to the C electrode at position y, the total potential at P_1 and P_2 can be defined. With reference to Figure 2.3a, the potential at P_1 in electrode position 4, due to the current source C_1 at electrode location 1 and the current sink C_2 at location 2 is

$$\phi_{4,1} - \phi_{4,2} = \frac{I}{4\pi}\left(\frac{\rho_{a_{4,1}}}{a} - \frac{\rho_{a_{4,2}}}{a\sqrt{2}}\right). \tag{2.4}$$

Following the same conventions the total potential at P_2 on electrode position 3 (Figure 2.3a) is

$$\phi_{3,1} - \phi_{3,2} = \frac{I}{4\pi}\left(\frac{\rho_{a_{3,1}}}{a\sqrt{2}} - \frac{\rho_{a_{3,2}}}{a}\right). \tag{2.5}$$

Most measuring systems measure the potential difference ($\triangle\phi$) between two potential electrodes. This is the sum of the individual potentials caused by the current source

and sink and can be written as:

$$\triangle\phi_\alpha = (\phi_{4,1} - \phi_{4,2}) - (\phi_{3,1} - \phi_{3,2}) = \frac{I}{4\pi}\left(\frac{\rho_{a_{4,1}}}{a} - \frac{\rho_{a_{4,2}}}{a\sqrt{2}} - \frac{\rho_{a_{3,1}}}{a\sqrt{2}} + \frac{\rho_{a_{3,2}}}{a}\right) \tag{2.6}$$

for the alpha array in Figure 2.3a, as:

$$\triangle\phi_\beta = (\phi_{2,1} - \phi_{2,4}) - (\phi_{3,1} - \phi_{3,4}) = \frac{I}{4\pi}\left(\frac{\rho_{a_{2,1}}}{a} - \frac{\rho_{a_{2,4}}}{a\sqrt{2}} - \frac{\rho_{a_{3,1}}}{a\sqrt{2}} + \frac{\rho_{a_{3,4}}}{a}\right) \tag{2.7}$$

and for the beta array in Figure 2.3b, and as:

$$\triangle\phi_\gamma = (\phi_{4,1} - \phi_{4,3}) - (\phi_{2,1} - \phi_{2,3}) = \frac{I}{4\pi}\left(\frac{\rho_{a_{4,1}}}{a} - \frac{\rho_{a_{4,3}}}{a} - \frac{\rho_{a_{2,1}}}{a} + \frac{\rho_{a_{2,3}}}{a}\right) \tag{2.8}$$

for the gamma array in Figure 2.3c. Recognising that $\rho_{a_{x,y}} = \rho_{a_{y,x}}$, it can be seen in Equation 2.9 that $\triangle\phi_\beta$ and $\triangle\phi_\gamma$ sum to $\triangle\phi_\alpha$ (terms in $\triangle\phi_\beta$ and $\triangle\phi_\gamma$ that cancel out are highlighted in red):

$$\triangle\phi_\beta + \triangle\phi_\gamma = \frac{I}{4\pi}\left(\frac{\rho_{a_{2,1}}}{a} - \frac{\rho_{a_{2,4}}}{a\sqrt{2}} - \frac{\rho_{a_{3,1}}}{a\sqrt{2}} + \frac{\rho_{a_{3,4}}}{a}\right) + \frac{I}{4\pi}\left(\frac{\rho_{a_{4,1}}}{a} - \frac{\rho_{a_{4,3}}}{a} - \frac{\rho_{a_{2,1}}}{a} + \frac{\rho_{a_{2,3}}}{a}\right)$$

$$= \triangle\phi_\alpha = \frac{I}{4\pi}\left(\frac{\rho_{a_{4,1}}}{a} - \frac{\rho_{a_{4,2}}}{a\sqrt{2}} - \frac{\rho_{a_{3,1}}}{a\sqrt{2}} + \frac{\rho_{a_{3,2}}}{a}\right). \tag{2.9}$$

The fact that $\triangle\phi_\beta$ and $\triangle\phi_\gamma$ sum to $\triangle\phi_\alpha$ can be utilised to check the quality of the collected data by calculating the tripotential error:

$$E_{tp} = \frac{R_\alpha - (R_\beta + R\gamma)}{R_\alpha}. \tag{2.10}$$

In isotropic and homogeneous ground, $\rho_{a_{x,y}}$ is independent of the electrode positions, so that the four terms that make up $\Delta\phi_\gamma$ in Equation 2.8 ($\frac{\rho_{a_{4,1}}}{a}$, $\frac{\rho_{a_{4,3}}}{a}$, $\frac{\rho_{a_{2,1}}}{a}$, and $\frac{\rho_{a_{2,3}}}{a}$) are all equal and $\Delta\phi_\gamma$ therefore reduces to zero. Inserting $\Delta\phi_\gamma = 0$ into Equation 2.9, gives $\triangle\phi_\alpha = \Delta\phi_\beta$ for isotropic homogeneous ground. However, if inhomogeneities are present or if the ground is anisotropic, $\rho_{a_{x,y}}$ varies with the electrode positions, so that in most cases $\triangle\phi_\gamma \neq 0$ and $\triangle\phi_\alpha \neq \Delta\phi_\beta$. In inhomogeneous or anisotropic ground, the measured resistances ($R_\alpha = \frac{\Delta\Phi_\alpha}{I}$ and $R_\beta = \frac{\Delta\Phi_\beta}{I}$) and the ap-

parent resistivities for the total measurement volume influencing the alpha and beta measurement (ρ_{a_α} and ρ_{a_β}), will therefore differ.

While it is recognised that ground heterogeneity and anisotropy can also be detected by measuring ρ_a with collinear electrode arrays rotated at their centre, it has been shown that the square array is more sensitive to subsurface heterogeneity than collinear arrays (Habberjam, 1972; Darboux-Afouda and Louis, 1989; Lane et al., 1995; Busby and Jackson, 2006), which makes it uniquely suitable for the potential detection of soil cracks.

Taylor and Fleming (1988) introduced the apparent resistivity ellipsoid, which is generated by rotating an electrode array (square or collinear) around its centre and plotting the measured apparent resistivities in a polar coordinate system. The shape of the generated apparent resistivity ellipsoid gives information about the geological strike direction. Taylor and Fleming (1988) generated apparent resistivity ellipsoids over hard rock and showed that for measurements that are representative of a formation, the electrode spacing needs to be larger than the mean fracture spacing. If fracture joints are present in the rock, and if the electrode spacing exceeds the joint spacing, the azimuthal resistivity peak measured with a square array is orthogonal to the direction of the greatest connectivity of the conducting fracture system. If the electrode spacing does not exceed the joint spacing, the azimuthal resistivity peak is orthogonal to the prominent joint set. Due to the paradox of anisotropy, which states that for a collinear array the true resistivity parallel to strike is measured by the apparent resistivity orthogonal to strike (Keller and Frischknecht, 1966), the azimuthal resistivity peak measured with a collinear array would be rotated by 90° compared to that measured with the square array. Since the work by Taylor and Fleming (1988), directional dependence of surface measurements has been used in a variety of studies to detect strike and fracture direction in hard rock (Ritzi and Andolsek, 1992; Said Attia al, 1994; Lane et al., 1995; Boadu et al., 2005; Busby and Jackson, 2006).

Watson and Barker (1999, 2005) showed that the use of a rotating Wenner offset array allows to differentiate between true anisotropy and subsurface heterogeneity.

Over true anisotropic ground the measured resistivity will only vary with direction of the electrode array and not with its location, as would be the case over heterogeneous ground. As shown by Samouelian et al. (2004) the resistivity measured over a cracked soil surface varies with both, the azimuthal direction of the electrode array and its location on the ground surface. This clearly shows that a cracked soil as a whole is heterogeneous and not anisotropic. However, Samouelian et al. (2004) introduced the ratio of R_α and R_β as the anisotropy index (AI), with an AI of unity indicating homogeneous ground and a deviation from unity highlighting inhomogeneity. As the presence of a soil crack results in an anisotropic alteration of the electrical field, it is most likely going to cause the AI to deviate from 1. Samouelian et al. (2004), who employed surface square arrays on a soil block, used these AI deviations to detected the formation of surface cracks.

In this study, the use of square array measurements is extended from surface measurements to a series of subsurface measurements throughout a soil profile. To emphasise the connection to the work by Samouelian et al. (2004), the term anisotropy index is maintained in this thesis. However, to avoid confusion it needs to be clarified that here the word anisotropy purely relates to the directional dependence of the resistivity measurement and does not aim to describe the soil body as a whole.

To allow a series of subsurface square array measurements, an electrode arrangement is proposed that consists of four electrode strings that are installed vertically in the subsurface forming a series of coplanar horizontal electrode squares between them (Figure 2.3d). With this electrode arrangement, the AI can be measured at each electrode depth, which leads to the collection of an AI depth profile (AIP). Before the ability of AI depth profiles to monitor subsurface crack dynamics is evaluated in the following Chapters, a quick note on the AI definition used in this study needs to be made. An AI deviation due to soil cracking can result in AI values $>$ or $<$ 1. To allow easier visual comparison between anisotropy profiles the AI values for this study are limited to ≤ 1; if the ratio of R_α and R_β is > 1, the inverse ratio is used. While this convention facilitates comparing the magnitudes of AI deviations,

it results in loss of information about the dominant fracture direction. Hence, a crack running from north to south would result in the same AI response as a crack running from east to west. To allow a distinction between these two scenarios, the true AI (AI_{true}), which can be $>$ or $<$ 1, is introduced.

Chapter 3

Anisotropy Response - Simple Cracks

The following Chapter describes a series of numerical simulations as well as a laboratory study that evaluate the suitability of anisotropy profiles for monitoring crack scenarios consisting of one or two cracks. The numerical simulations show that, except for two distinct crack scenarios, the presence of cracks is clearly reflected in an anisotropy profile and that the depth of a single crack is directly related to the depth of the *AI* deviation within the *AIP*. Next a laboratory study is described, in which cracks were simulated by introducing a plastic sheet into a sand profile. Results from the laboratory study show that the conclusions from the numerical simulations also hold true for real data sets incorporating measurement errors and background inhomogeneities.

3.1 Numerical Study

3.1.1 Methods

Numerical simulations were carried out with *Res3Dmodx64* (Loke, 2009b), a finite difference forward modelling program. *Res3Dmodx64* simulates the resistance that would be measured with a user defined electrode arrangement over a user defined subsurface resistivity distribution. The program is based on the classic finite difference code described by Dey and Morrison (1979), which solves the 3D potential distribution

due to a point current source in a 3D half space.

During forward modelling, *Res3Dmodx64* uses two resistivity blocks between adjacent electrodes and 10 buffer blocks to the side of the model. To simulate AI profiles, a subsurface model consisting of 11 x 11 dummy electrode positions in 12 horizontal model layers is generated. Four boreholes were located at electrode positions: 3,3; 3,9; 9,3 and 9,9, which contained electrodes at every model layer. The 12 model layers had a constant separation of half the distance between the dummy electrodes within each layer. This arrangement resulted in a perfect cube (with 1.2 m side length) between the four boreholes. A schematic of the generated subsurface model is shown in Figure 3.1. To test the modelling technique an initial simulation with all model blocks set to 10 Ωm was carried out. As the AI profile derived from this simulation had the expected values of 1 for homogeneous soil, the simulations were continued for different crack settings.

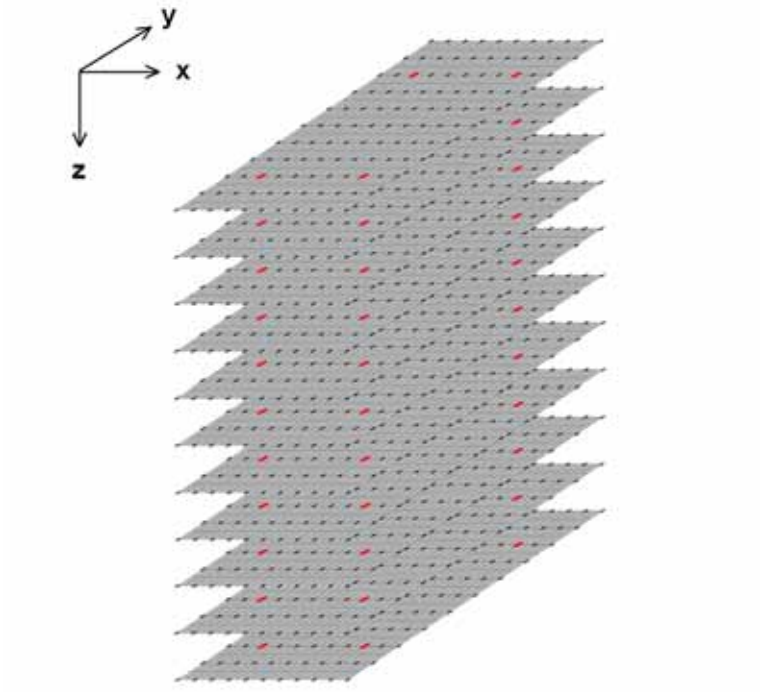

Figure 3.1: Schematic of the model setup for the numerical simulations (red points denote borehole electrodes; black points denote dummy electrodes).

A model block containing a crack was simulated by setting its resistivity to 100,000 Ωm while the remaining resistivity blocks were kept at 10 Ωm to simulate the conduc-

ting soil matrix. Firstly, the anisotropy response due to a single crack running parallel to the y-axis was investigated. Simulations were run with the crack varying in depth, length, width and location. Secondly, simulations including a second crack that was oriented orthogonal to the initial crack were carried out. The length and location of the second crack was altered and the anisotropy response was calculated. Thirdly, the anisotropy response due to a crack running in a diagonal direction through the modelling area was simulated. The diagonal crack was varied in depth, length, width and location. After simulations due to a perfectly diagonal crack, the same set of simulations was repeated for a crack intersecting the modelling area at an angle of 65° and 75°. Fourthly, the resistivity contrast between the crack and the soil matrix was reduced. A reduction of the resistivity was achieved in two ways: Firstly, by reducing the resistivity of the model block that contained the crack to 100 Ωm instead of 100,000 Ωm and secondly by creating an intermittent crack, where every second crack containing model block was set to the matrix resistivity of 10 Ωm.

Finally, the AI deviation due to gradual resistivity changes within the entire soil matrix, which could occur in a natural soil profiles, were simulated. Resistivity values between 10 and 50 Ωm were randomly distributed in each model layer and simulations were run for five different resistivity arrangements. After simulations without any cracks, a centred crack running parallel to the y-axis was added on top of the randomly distributed resistivity variations.

3.1.2 Results and Discussion

Several versions of anisotropy indexes will be defined and used in this section. For the reader's convenience these indexes are summarised in Table 3.1.

index	AI definition	defined on page
AIP_0	profile without a crack	23
AIP_{max}	profile with crack through entire depth	23
$AIP_{0.6}$	profile with crack to 0.6 m depth	23
$AI_{max_{avg}}$	AI value averaged over profile depth of AIP_{max}	23
AI_{true}	true AI before normalisation to ≤ 1	19

Table 3.1: Summary of anisotropy indexes used in this section

Selected simulation results for a single crack running parallel to the y-axis are shown in Figure 3.2. It can be seen that the depth of the AI deviation is directly related to the depth of cracking. The array of AIP curves in Figure 3.2a lies between the AI profile that was measured in a non cracked model (AIP_0), and the AI profile measured for a crack intersecting the entire model depth (AIP_{max}). With increasing electrode depth, the region below the crack increasingly contributes to the current conduction, which results in the gradual, rather than a sharp, reversion of the AIP to AIP_0.

A slight increase in the AI deviation occurs if the crack location is moved from the centre of the array in model column 10 towards the boreholes, which is shown in Figure 3.2b for AIP_{max}. The AI response due to a change in the crack location increases the closer the crack moves towards the probes. While AIP_{max} forms a straight line if the crack is located in the centre of the array, a curvature is introduced if the crack location shifts towards the probes. The AI response, including the introduced curvature of AIP_{max}, is identical, regardless of whether the move from the centre is towards the left or the right of the modelling area.

The crack length of a single crack is strongly related to the resulting anisotropy response. Figure 3.2c shows the AIP_{max} for cracks of different length, which were centred in the modelling area. If the crack intersected the entire model domain, the mean AI value over the profile depth ($AI_{max_{avg}}$), is 0.0003. A reduction in crack length causes a gradual increase of $AI_{max_{avg}}$ towards 1. The strong influence of the crack depth and length on the AIP shows that the AIP is directly related to the horizontal and vertical extent of the anisotropic alteration in the electrical field caused by the crack.

Figure 3.2d shows the influence of crack width on the AI. Two crack depths are selected for display, a crack that intersects the entire measuring profile of 1.2 m and hence results in AIP_{max}, and a 0.6 m deep crack that results in $AIP_{0.6}$. It can be seen that an increase in crack width only slightly increases the AI deviation.

Selected results for the simulation of the AI response due to two orthogonal cracks

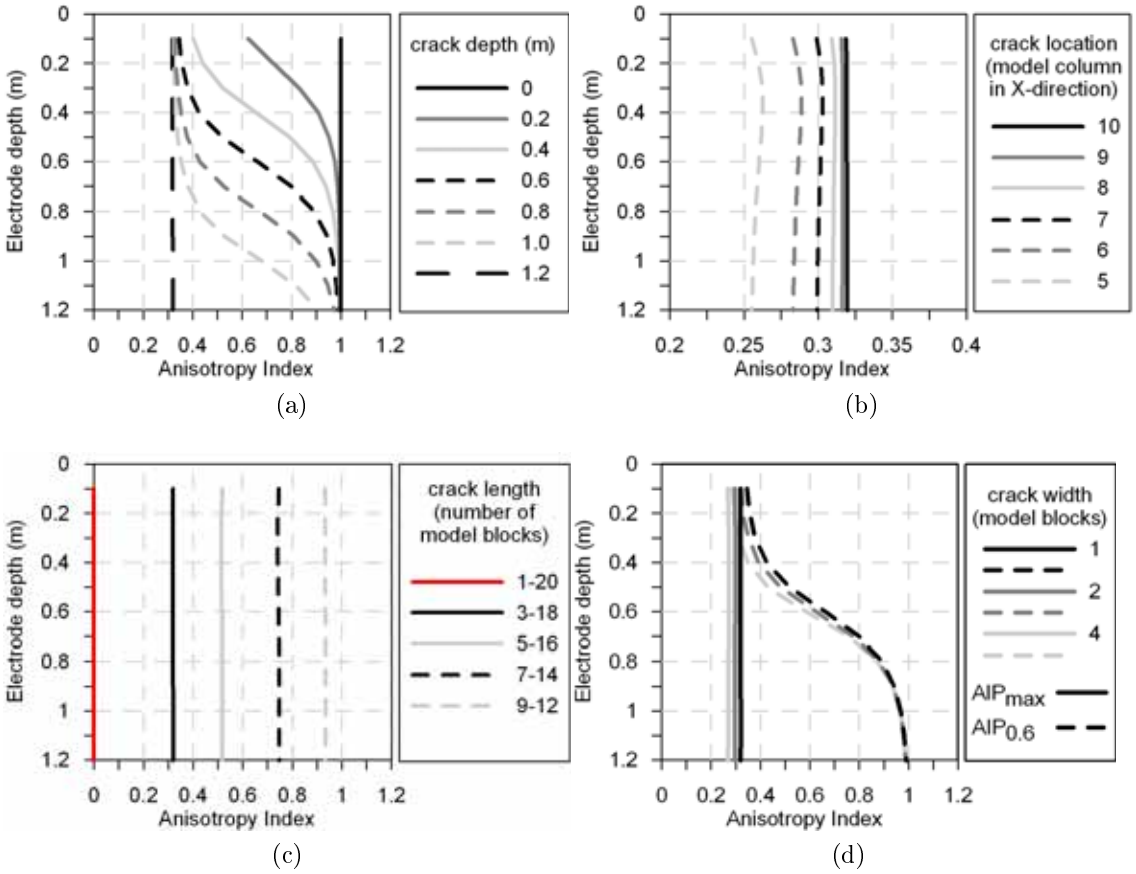

Figure 3.2: Selected AI responses simulated for a square array with 1.2 m side length, due to a single crack that runs parallel to and is centred along the y-axis (unless differently indicated the crack has a length of 16 model blocks); a: AIP for a crack in the centre of the modelling area at different crack depth; b: AIP_{max} for a crack moving from the model centre towards the probes. Crack location is expressed as the x coordinate of the model blocks containing the crack; c: AIP_{max} for a crack of different length; d: AIP_{max} and $AIP_{0.6}$ for a crack with varying width.

are shown in Figure 3.3. Adding an orthogonal crack reduces the AI deviation of the initial crack. The reduction of the AI deviation is largest if the two orthogonal cracks are of identical length and intersect in the centre of the the modelling area. In this case the AI deviation is completely removed and the $AI_{max_{avg}}$ becomes 1 indicating homogeneous conditions. However, as soon as one of the orthogonal cracks is offset from the centre or if the two cracks differ in length, an AI deviation occurs. As in Figure 3.2b, a curvature of AIP_{max} results if one of the cracks is located close to the edge of the modelling area (Figures 3.3b and c).

A diagonal crack that intersects the modelling area at 45° does not affect the AI, no matter where the crack is located or how long or how wide it is. Habberjam (1975)

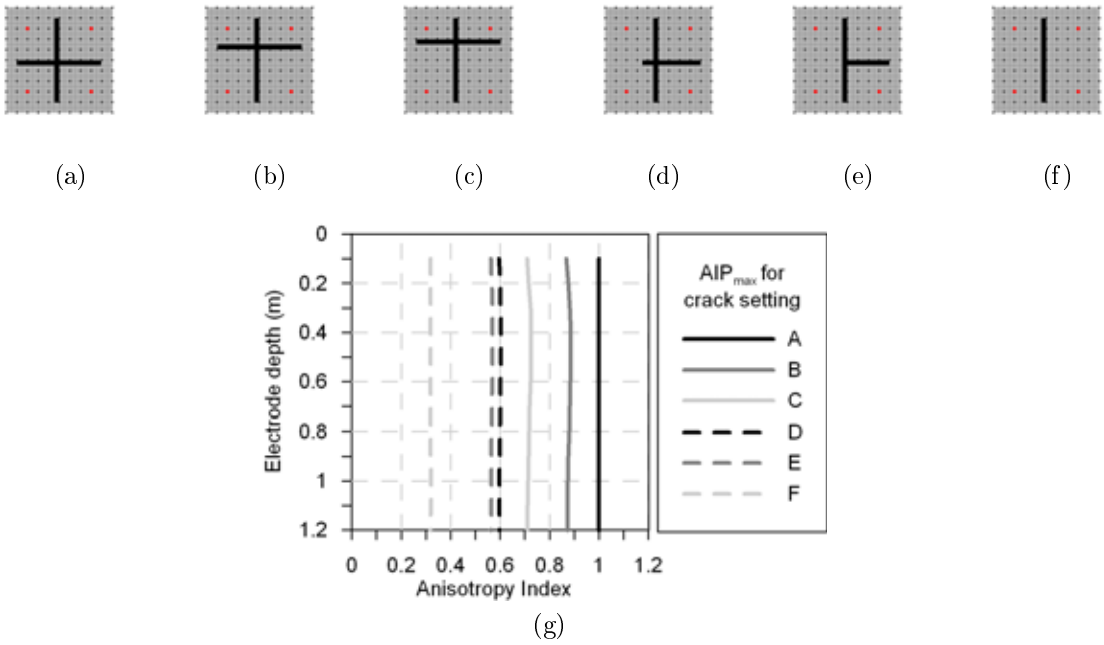

Figure 3.3: a-f: Selected crack settings with two orthogonal cracks as well as with a single crack (red points denote borehole electrodes; black points denote dummy electrodes); g: AIP_{max} simulated for a square array with 1.2 m side length due to the crack settings A-F.

called this inability to detect structures that intersect the square array at 45° the basic inadequacy of the single square array. This inability was also demonstrated by Samouelian et al. (2004), who showed that cracks with a preferential orientation close to 45° resulted in an AI close to 1. However, the simulation results show that as soon as the crack diverts from 45° an AI deviation is introduced. Figure 3.4 shows the AI response due to selected crack scenarios involving diagonal cracks. The AIP for a single diagonal crack shows an increased AI deviation the steeper the crack is intersecting the model area, resulting in a gradual increase in the deviation from no deviation at 45° to a maximum deviation for a crack that runs parallel to one of the axes. This dependence of the measured resistivities used to calculate the AI on the crack angle, is used in the apparent resistivity ellipsoid (Taylor and Fleming, 1988) to determine the strike of fracture systems in hard rock.

Figures 3.4c-e show a diagonal crack intersecting a base crack that runs parallel to the y-axis. A diagonal crack at 45°, which by itself does not cause an AI deviation, decreases the AI deviation caused by the base crack. The AI deviation is further

reduced if the angle of the diagonal crack relative to the initial crack is $> 45°$ (Figure 3.4d). As we have seen in Figure 3.3a, this reduction becomes maximal and $AI_{max_{avg}}$ becomes 1, if the two cracks intersect each other at 90°. On the other hand, if the diagonal crack has an angle of $< 45°$ (relative to the base crack) the AI deviation of the base crack is increased (Figure 3.4). This behaviour can be explained by examining AI_{true}. By itself, the diagonal crack in Figure 3.4d results in $AI_{true} > 1$, while the diagonal crack in Figure 3.4e results in $AI_{true} < 1$. If added to the base crack with an $AI_{true} < 1$, the crack in Figure 3.4d with an $AI_{true} > 1$ reduces the AI deviation of the base crack, while the crack in Figure 3.4e with an $AI_{true} < 1$ further increases the AI deviation of the base crack. By themselves, the two orthogonal cracks in Figure 3.3a produce AI_{true} that are the inverse of each other. Superimposed on each other the two orthogonal cracks result in an AI_{true} of 1, which is the product of the AI_{true} values of the two individual cracks. Unfortunately this simple relationship between the AI_{true} values of the two individual cracks and the AI_{true} of both cracks together is an exception.

The AI deviation caused by the five different random resistivity variations between 10 and 50 Ωm were moderate compared to the deviations caused by the simulated crack scenarios. The largest AI deviation caused by these random variations resulted in an $AI_{max_{avg}}$ of 0.83. The AI deviation of the crack that was introduced on top of the background variations was reduced slightly in comparison to the same crack over homogeneous ground, regardless of whether the background inhomogeneities resulted in an $AI_{true} >$ or < 1. Instead of an $AI_{max_{avg}}$ of 0.32 the crack now caused an $AI_{max_{avg}}$ between 0.48 and 0.58 for the five random background variations.

A reduction in the resistivity that was assigned to the crack reduced the resulting AI deviation. A crack with a resistivity value set to 100 Ωm instead of 100,000 Ωm caused an $AI_{max_{avg}}$ of 0.58, instead of 0.32. Further reduction of the AI deviation occurred if the crack was intermittent. A crack that only had every second model block set to 100,000 Ωm, while the other model blocks maintained the matrix resistivity of 10 Ωm, resulted in an $AI_{max_{avg}}$ of 0.86 instead of 0.32 for the non intermittent crack.

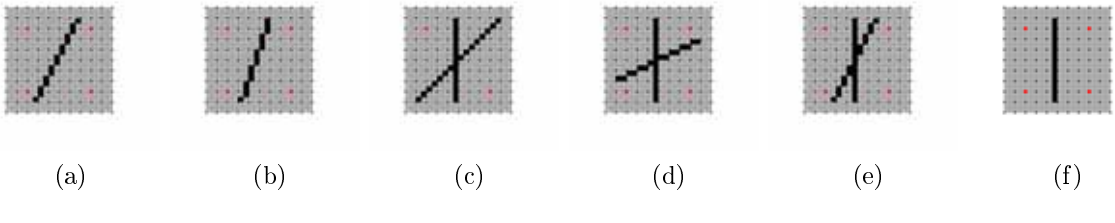

(a) (b) (c) (d) (e) (f)

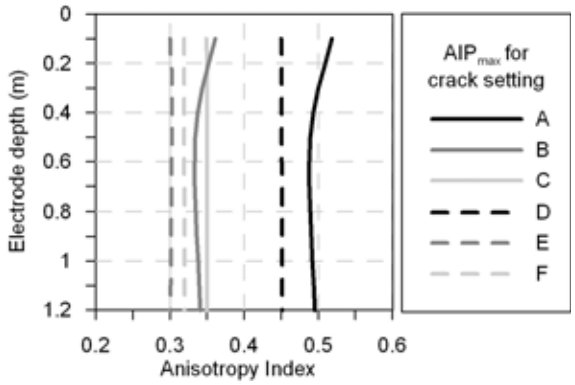

(g)

Figure 3.4: a+b: Single diagonal crack intersecting the modelling area at 65° and 75°, respectively; c-e: Diagonal cracks running at angles of 45°, 25° and 65° relative to the modelling area, which intersect a second crack that runs parallel to the y-axis; f: Single crack running parallel to the y-axis for comparison; g: AIP_{max} simulated for a square array with 1.2 m side length due to the crack settings above (in a-f: Red points denote borehole electrodes; black points denote dummy electrodes).

The curvature that was introduced to the AIP curves, if the crack location moved close to the model border can be attributed to border effects. The curvature was not observed for simulations in a model area with an additional 20 model cells in the x and y direction. However, as the differences between $AI_{max_{avg}}$ for AIP curves with and without a curvature were negligible, the occurrence of border effects do not influence the major conclusions.

3.1.3 Conclusions from the Numerical Study

Theoretical calculations show that the AI deviation of a single crack is a function of its location, depth, length and orientation. For crack scenarios with two intersecting cracks, the AI deviation additionally becomes a function of the intersection point and the intersection angle of the two cracks. The numerical simulations have confirmed that soil cracking and a variation in cracking depth of simple crack scenarios can be

detected by anisotropy profiles with the exception of two specific crack scenarios. No AI response was caused by diagonal cracks intersecting the modelling area at 45° and by two orthogonal cracks of identical length and width intersecting at the centre of the modelling area. However, these two scenarios are very unlikely to occur in natural crack systems and each slight variation from these two settings is accompanied by an anisotropy response. Their existence therefore does not compromise the suitability of anisotropy profiles for crack detection.

3.2 Laboratory Study

To further validate the suitability of using anisotropy profiles for detecting cracks, controlled measurements were undertaken in the laboratory. The major variables controlled include water salinity, sediment type, crack geometry and depth.

3.2.1 Methods

A set of four electrode strings was constructed to allow square array measurements in coplanar measurement squares in 50 mm depth intervals. Each electrode string consisted of 12 ring shaped brass electrodes (38 mm diameter), which were consecutively pushed onto a plastic tube (10 mm diameter), followed by a 50 mm long piece of plastic tube (20 mm diameter) to maintain the inter electrode spacing. Each electrode was connected to an individual insulated wire. The wires were lead through the centre of the inner plastic tube to the top of the probes, where they were bound into a cable that terminated in a 32 pin connector (two electrode strings to one connector).

The strings were positioned in a cylindrical weighing lysimeter (inner diameter 1300 mm, depth 650 mm), which was filled with a 50 mm deep layer of river gravel followed by 600 mm of beach sand. To allow free drainage of excess water, the entire lysimeter was tilted at 3.5° and a 28 mm diameter hole was cut into the lowest part of its wall (Figure 3.5). Once in place, the electrode strings formed a horizontal electrode square with a side length (a) of 550 mm at each electrode depth, with the first electrode

of each string located at the sand surface and the last electrode located at 550 mm. This electrode arrangement forms a cube fitted to the lysimeter dimensions with the same relative geometry used in the numerical simulations described in Section 3.1. The saturated sand profile was drained before the strings were positioned into four hand dug holes. After the probes had been positioned, the holes were back filled and the sand profile was again saturated.

To estimate the magnitude of possible border effects in the lysimeter, a *Res3Dmodx64* model with the dimensions of the sand lysimeter was generated. The model consisted of 12 model layers, each consisting of 28 x 28 model blocks, which contained 15 x 15 dummy electrode positions (2 model blocks between each dummy electrode). The electrodes of the square array were located on electrode positions 5,5; 5,11; 11,5 and 11,11. Three simulations where run, to simulate the AI profile due the three crack settings, which were later simulated in the sand lysimeter (Figure 3.6). Simulations were run for a crack that intersected the entire depth of the profile.

The physical resistivity measurements in this study were carried out with an ABEM SAS4000 / ES10-64C package, which allows any electrode combination for measurements to be pre-programmed and run automatically. A measurement protocol that measured the resistance with the alpha, beta and gamma square array at each electrode depth, was programmed and uploaded on the ABEM terrameter. Below this measurement routine is referred to as the square protocol.

Next, a 10 mm thick rectangular plastic sheet (870x450 mm) was inserted between the four electrode strings. Being non conducting, the plastic sheet simulated an air-filled crack. The sheet was inserted lengthwise to form sheet position 1 and crosswise to form sheet positions 2 and 3 (Figure 3.6a). At each position the sheet was inserted to 100, 150, 300, and 450 mm and the square protocol was run for each insertion depth. Furthermore, measurements were carried out without any plastic sheet inserted before and after each sheet setting. Finally, the quality of the acquired resistance measurements was determined based on the tripotential error (Equation 2.10 on page 16) and the AI was calculated for each electrode depth.

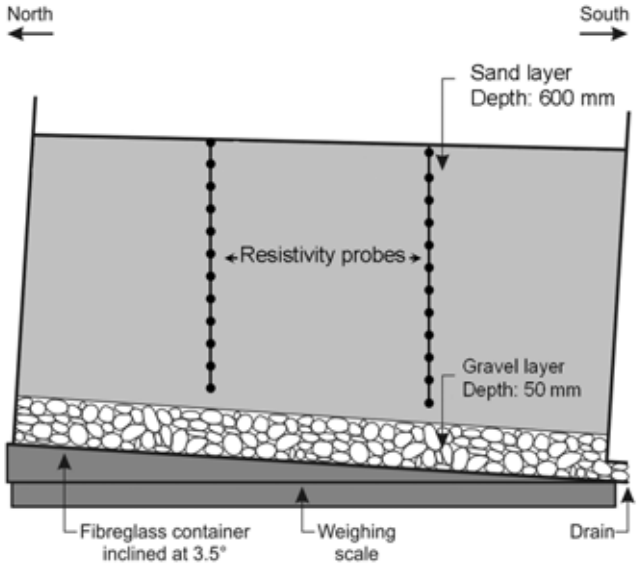

(a)

Figure 3.5: Schematic cross-section of the sand filled weighing lysimeter.

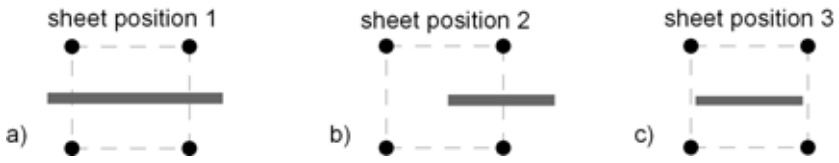

Figure 3.6: Birds-eye view of the three positions of the plastic sheet used in the sand lysimeter.

3.2.2 Results and Discussion

The plastic sheet, being an insulator, caused an alteration of the electrical field similar to an air-filled soil crack. Figure 3.7a shows the *AIP* for sheet position 1 (Figure 3.6) at the four insertion depths. Also shown are the changes in background inhomogeneity that are highlighted by the *AIP* without the plastic sheet measured before and after the measurements with sheet position 1.

Background heterogeneities in the sand profile are most likely due to a variation in salt and moisture distribution, as well as to bulk density variations of the sand profile, which was obtained from an ocean beach. Furthermore, the slight tilt of the lysimeter base and any deviations from a perfect measurement square between the resistivity probes might also contribute. Measurement errors on the other hand are not likely to affect the background inhomogeneities, as the tripotential error (Equation 5) was < 2 % for all measurements. The observed changes in the background heterogeneity,

before and after the measurements with sheet position 1, can be accounted to changes in the salt distribution and/or the bulk density during insertion and repositioning of the plastic sheet.

As for the simulated data in Section 3.1, a direct relation between the sheet insertion depth and the depth of AI deviation is evident. A comparison of the data set collected in the lysimeter and the corresponding simulated data set is shown in Figure 3.7b. Relative to the simulated data, the collection of AIP curves from the lysimeter experiment is shifted towards the left of the graph, showing a greater AI deviation. Furthermore, the lysimeter AIP curves for a crack depth of 0.10 and 0.15 m show a moderate kink at a depth of 0.3 m, which is in contrast to the AIP curves of the simulated data that steadily revert towards AIP_0. Both the shift towards the left of the graph and the kink at 0.3 m can be attributed to the background inhomogeneity in the sand lysimeter. In addition, the differences in the resistivity contrasts between the sand and the plastic sheet, and the matrix and crack resistivity in the simulated model could have added to the observed differences. The apparent resistivity measured with the square array in the lysimeter varied between 0.3 and 0.6 Ωm for measurements without the plastic sheet, while the numerical simulations were carried out with a homogeneous matrix resistivity. Furthermore, the resistivity that was chosen for the crack affected model blocks of the numerical simulation (100,000 Ωm) is only an approximation of the infinite resistivity of an air-filled crack; as is the resistivity of the plastic sheet. As shown in Section 3.1, both the resistivity contrasts between crack and matrix as well as the background inhomogeneities have an affect on the AIP.

Figure 3.8 shows the anisotropy profile for sheet positions 1, 2, and 3 (Figure 3.6), which intersect 2, 1, and none of the sides of the electrode square, as well as the background anisotropy without a plastic sheet that was measured after the measurements with sheet position 3. The influence of the different sheet positions on the AI deviation is similar to the numerical results for varying crack length in Figure 3.2c on page 24. The sheet has the highest influence on the AIP if 2 sides

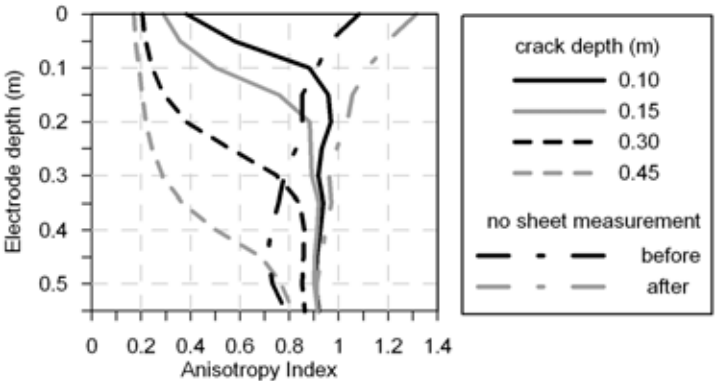

(a)

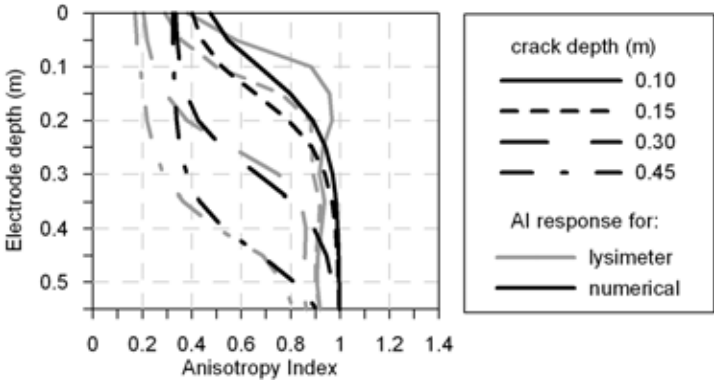

(b)

Figure 3.7: a: Anisotropy profiles measured with a square array with 550 mm side length at sheet position 1 for different insertion depth as well as the background inhomogeneity measured without a sheet before and after the measurements with sheet position 1; b: Anisotropy profiles measured in the sand profile as well as the anisotropy profiles from the numerical modelling for the corresponding depth intervals.

of the measurement square are intersected by the plastic sheet, while the influence is smallest if no side is intersected. Samouelian et al. (2004) reported similar observations and noted that a crack, which does not intersect the plane between P_1 and P_2 has a reduced influence on the AI. However, Figure 3.8 shows that even if the plastic sheet does not intersect any side of the electrode square, its presence is still clearly detected by a deviation of the AI compared to the background anisotropy profile. The presence of the background inhomogeneity shows that rather than investigating the AI deviation from 1, its deviation from a non cracked soil scenario should be investigated.

The numerical simulations that were run to estimate the border effects showed no curvature and hence no signs of border effects in the generated AI_{max} profiles. It is

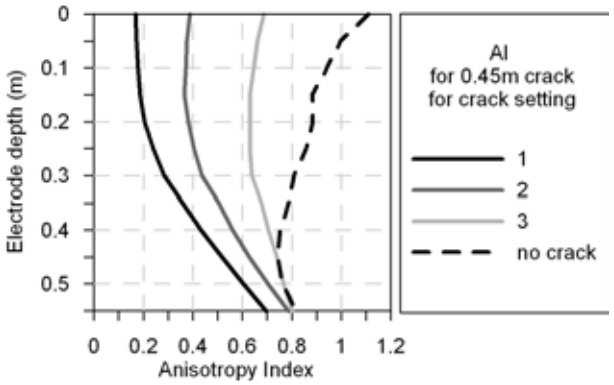

Figure 3.8: Anisotropy profiles measured with a square array with 550 mm side length at insertion depth of 450 mm for sheet positions 1, 2, 3, and without any plastic sheet.

therefore assumed that border effects due to the lysimeter walls were insignificant.

3.2.3 Conclusions from the Laboratory Study

This section demonstrates that anisotropy profiles can detect the presence and depth of soil cracks in experimental data sets even with the noise from measurement errors and background inhomogeneities. In experimental data sets, the background inhomogeneities can be significant and need to be monitored and incorporated into the interpretation. For crack detection, a measured AI deviation should be compared to the AI measured under non cracked conditions, rather than to an AI of 1.

Soil cracks are significantly more complex than the simple crack scenarios that have been investigated here and a successful method for crack detection needs to be able to detect cracks in a range of arrangements relative to the square array. Chapter 4 therefore examines the possibility of crack detection with anisotropy profiles for the complex fracture networks that form in soils.

Chapter 4

Anisotropy Response - Natural Soil Cracks

Crack networks that form in soil are significantly more complex than the simple crack scenarios studied in Chapter 3. To determine the AI response due to these complex crack structures a numerical and a laboratory study was carried out. In the numerical study, the AI response due to crack structures derived from crack photographs was simulated. The results confirmed that AI deviations are suitable to detect cracks, even if the cracks have complex structures and show no directional dependence. Following the numerical study, a laboratory experiment is described. Here, the anisotropy profiles in a lysimeter filled with cracking clay soil were monitored during two drying and irrigation events. The results of the laboratory study confirm that anisotropy profiles are an excellent tool for monitoring soil cracking as it is the crack dynamics and not soil moisture changes that dominate the AI response.

4.1 Numerical Study

4.1.1 Methods

Two lysimeters, identical to the one described in Section 3.2.1 on page 28, were filled with cracking clay soil. Lysimeter A was filled with soil from the Coleambally irriga-

tion area in southern New South Wales, Australia. The soil had sand, silt, and clay fractions of 20, 40, and 40%, respectively, with illite being the dominant clay mineral. Lysimeter B was filled with soil from Breeza in northern New South Wales, which had sand, silt, and clay fractions of 16, 20, and 64% respectively; montmorillonite made up 90% of the clay fraction. Before the soil was placed in the lysimeter it was thoroughly mixed while dry and water was added until it had a paste like consistency. Once in the lysimeter, the soil was flushed with 500 mm of tap water (EC: 20 mS/m) to leach out residual salts. To reinstate the aggregate structure of the soil it was re-wetted and left to dry during multiple separate water application and drying periods. The soil in Lysimeter A went through a total of 15 water applications (tap water) and drying periods within four years, while soil B went through 18 water applications and drying periods within six years. The construction of the two lysimeters was carried out by Dr Justin Bell.

Following the initial set up of the two lysimeters a digital camera was mounted 1.45 m above the soil surface to collect images of the surface crack network. Four sets of two lights mounted on a frame around the lysimeter rim briefly illuminated the soil surface from 4 directions each time a picture was taken. Illumination from four directions avoided shadows over the uneven soil surface, which would have created noise during image processing.

Soil A was exposed to a further three irrigation and drying periods while soil B was exposed to another two. During the irrigation periods ∼60 L (∼46 mm) of tap water were evenly applied to the soil surface with a watering can followed by a drying period of 3 to 4 weeks. The surface crack networks that had formed by the end of the drying periods were used as templates for the cracks in the numerical simulation. The digital colour images from the overhead cameras were first converted into intensity images and then further processed into binary images to highlight the cracks. Differences in soil colour prevented the use of a single grey threshold for the conversion from an intensity image to a binary image. Instead the segmentation threshold was chosen individually for each image and each location x within that image, similar to the

method described by Vogel et al. (2005). The segmentation threshold was based on the local mean, which was calculated in a 51x51 pixel window centred at point x. If the original grey level at point x was darker than the mean times 0.9 the pixel was identified as "crack" and given a black pixel, otherwise it was set to "no crack" with a white pixel.

Next, the size of the binary image was reduced to 166 x 166 pixels using a nearest neighbour filter and the image was converted to a model file which could be read in by *Res3Dmodx64* as a subsurface model. The model file consisted of 5 constant depth layers, each layer consisting of 166 x 166 resistivity blocks, with the electrodes of the square array located in blocks 25,25; 141,25; 25,141 and 141,141. The upper three layers contained the crack network that was captured in the surface image, while the lower 2 layers were crack free. During the image conversion, each of the binary image pixels was converted into a model block, which was set to 0 for a matrix pixel and to 1 for a crack pixel (Figure 4.1). The size of the model layers, and hence the resolution of the utilised binary image, was set to use the entire available number of model blocks in *Res3Dmodx64*. The scale of the model was chosen to simulate the AI response due to a 30 mm deep crack network, measured with a surface electrodes square with a side length of 450 mm. The surface electrode spacing was chosen to be large in comparison to the crack spacing to allow representative AI measurements (Taylor and Fleming, 1988), while still leaving sufficient space between the measurement area and the border of the modelling domain.

The conversion from a colour image to a binary image was carried out in *Matlab* (MathWorks, 2007), while the conversion from the binary image to the *Res3Dmodx64* model file was carried out in *Python* (Python, 2008).

For each final crack image the total surface area of the cracks (A) and the estimated crack spacing (λ) was determined. The estimated crack spacing was obtained following the approach described by Colina and Roux (2000b). In *Matlab*, a fine grid was drawn over the crack image and the intersections between cracks and grid lines were counted. To calculate λ, the number of intersections was then divided by the total length of

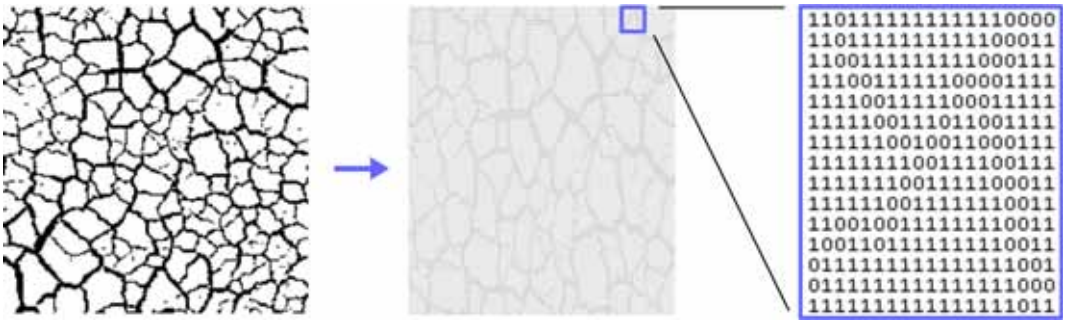

Figure 4.1: Conversion of the black and white crack images into a model layer for *Res3Dmodx64* consisting of 1s and 0s.

the grid lines. Thus λ is the average length in cm after which a random straight line over the soil surface would in average intersect a crack. Colina and Roux (2000b) note that λ can only be compared to the typical size of a soil aggregate if the aggregates have a regular size and shape.

4.1.2 Results and Discussion

The five crack networks that were used for the *Res3Dmodx64* simulation are shown in Figure 4.2. Resolution of these images was limited by the maximum number of model blocks in *Res3Dmodx64*. A comparison with the original colour photographs, which were the base for these black and white images (Figure 4.3), shows that the main features of the crack network were well captured in the black and white images even with resolution restrictions. Visual comparison of the images shows that the surface cracks that formed in soil B (Figures 4.3d and e) are wider than those in soil A (Figures 4.3a-c). Wider surface cracks in soil B are also indicated by a significantly larger crack area, while the crack spacing shows less severe differences. The average crack area for the surface crack network in soil B is ∼2.4 times larger than the average area measured in soil A; while the average estimated crack spacing in soil B (43 mm) is only slightly lower than that of the crack networks formed in soil A (49 mm).

The simulation results in Table 4.1 demonstrate that AI deviations are also caused by natural crack networks with random structure. However, a clear relationship between features of the crack networks in Figure 4.2 and the resulting AI values is not evident. The simulated AI at the surface of the crack network varied from 0.47 to

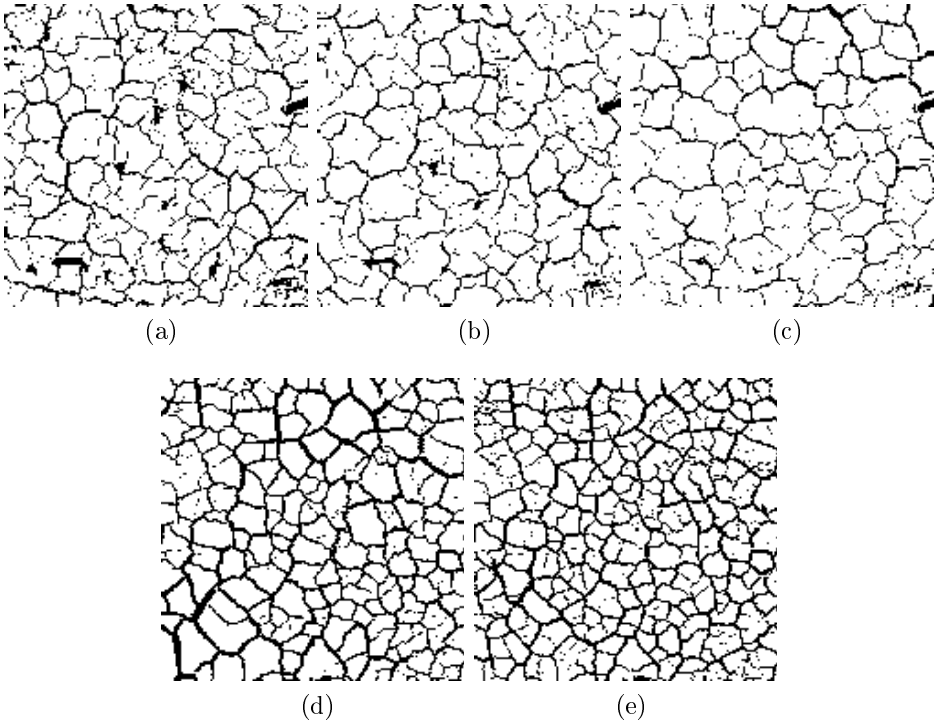

(a) (b) (c)

(d) (e)

Figure 4.2: Black and white crack images (166X166 pixels) that were turned into model layers of 166 x 166 model blocks and read in to *Res3Dmodx64* to simulate the resulting AI; a-c: Soil A, irrigation 1-3; d+e: Soil B, irrigation 1+2 (frame width of images: 0.65m).

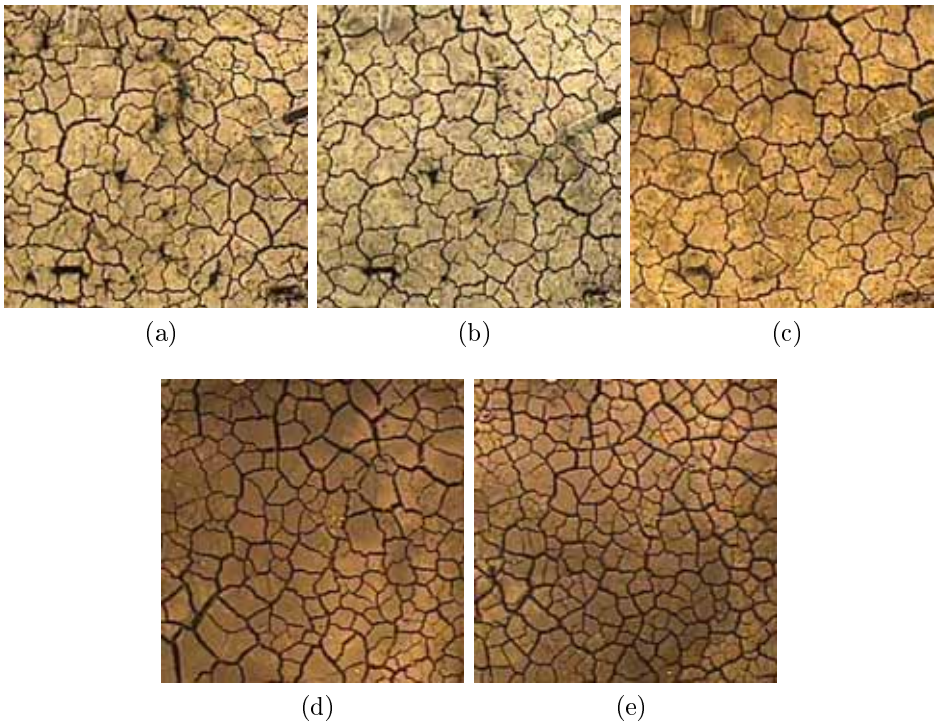

(a) (b) (c)

(d) (e)

Figure 4.3: The original colour images before processing that were the base for the black and white images in Figures 4.2; a-c: Soil A, irrigation 1-3; d+e: Soil B, irrigation 1+2 (frame width of images: 0.65m).

0.75 (Table 4.1). Both the maximum and minimum AI values were simulated in the crack networks that formed in soil B, which confirms the findings in Section 3.1 that the crack width has a negligible influence on the AI. This is logical considering that as long as two crack walls do not touch, an air-filled crack does not conduct current, regardless of its width. Changes in crack width therefore have a negligible influence on the electrical field. Furthermore, the fact that the largest and smallest AI deviation were both measured in soil B suggests that the AI is, if at all, only weakly influenced by the crack spacing.

It is known from Section 3.1 that the magnitude of the AI deviation caused by a single crack is a function of its location, depth, length, and orientation. If two cracks are intersecting, the point of their intersection and the intersecting angle further influence the AI deviation. Extending these findings to natural soil cracks suggests that the AI responses shown in Table 4.1 are a function of the location, length and orientation of the collection of cracks as well as of the location of their intersection points and their intersection angles. All cracks in this simulation had a depth of 30 mm, in natural crack systems the varying depth would also contribute to the AI deviation. In view of the AI dependency on all these variables and considering the multiple cracks, intersection points and angles of the crack networks in Figure 4.3, the lack of a simple relationship between features of the crack networks and the AI is not surprising.

The different AI responses of the crack networks that formed during consecutive drying periods within the same soil, together with a visual comparison of the crack images in Figure 4.3 is in accordance with the alternating surface crack networks observed by Wells et al. (2003) as opposed to crack reappearance of surface cracks (White, 1970; Waller and Wallender, 1993; White, 2001).

4.1.3 Conclusions from the Numerical Study

Natural crack networks without any directional dependence result in AI deviations. The magnitude of this deviation is a function of the location, depth, length and

Table 4.1: Anisotropy index simulated for a square array with 450 mm side length at the soil surface due to a 30 mm deep crack system for the crack networks shown in Figures 4.2a-e.

image ID (Fig. 4.2)	crack network	*AI*
a	soil A: drying period 1	0.48
b	soil A: drying period 2	0.70
c	soil A: drying period 3	0.70
d	soil B: drying period 1	0.75
e	soil B: drying period 2	0.47

orientation of the collection of cracks as well as of the location of their intersection points and their intersection angles. Crack width and crack spacing have no significant influence on the *AI*.

4.2 Laboratory Study

4.2.1 Methods

The set of four resistivity strings (see description in Section 3.2.1) was installed in the lysimeter with soil B, and the anisotropy response in the 450 mm deep profile of cracking soil was measured (refer to Section 3.2.1 for the lysimeter set up and Section 4.1.1 for a description of the soil filling procedure).

Installation of the electrode strings took place 14 days after a water application brought the soil back to its field capacity (309$\pm$5 L). At this stage, the soil was soft while not too sticky, which were perfect conditions for augering. The set of electrode strings was arranged in vertical holes that were positioned on the corners of a 500 mm sided surface square. Just as in Section 4.1., the size of the surface square was chosen to assure a balance between a large electrode spacing in comparison to the crack spacing, while not moving the resistivity probes too close to the lysimeter border. The holes were hand augered with a 40 mm diameter spiral auger. To assure vertical augering the auger was held in place by a wooden plank with a circular notch, which was fixed onto the lysimeter brim. All augered material was collected and worked into a putty textured soil water paste, which was used to cover the strings before they

were inserted into the augered holes. Covering the strings resulted in a tight fit of the electrodes in the augered holes and assured good contact with the soil matrix. Only 9 of the 12 electrodes on each string were inserted into the profile, with the first of these nine located at the soil surface and the last located at 400 mm depth.

Once the electrode strings were installed, the soil in the lysimeter was brought back to its field capacity by adding 10 L of tap water with a watering can. Next, the soil was left to dry for 12 weeks, while the square protocol was run weekly. After the drying period, the soil was again brought to field capacity by adding 70 L (54 mm) of tap water within 90 minutes. Throughout the water application and for an additional 90 minutes, photos of the soil surface were taken every 2.5 minutes and the square protocol was run every 5 minutes. Potential drainage water was collected at the lysimeter outlet over a 48 hour period following the irrigation. The quality of the acquired resistance measurements was determined based on the tripotential error (Equation 2.10 on page 16) and the AI was calculated for each electrode depth.

4.2.2 Results and Discussion

Changes in the anisotropy profiles measured during the drying and irrigation period are shown in Figure 4.4. Throughout the drying period, the AI deviation from its initial value, close to 1, increased, with the largest change in AI occurring at the top of the profile. With progressive drying, increasingly deeper layers of the profile showed a change in the AI, which is consistent with the increased downward extension of a crack network during drying (Johnston and Hill, 1944).

Due to soil shrinkage, one of the electrodes at the soil surface lost contact in the fourth week of drying. For the rest of the drying period the AI at the top of the profile could not be determined. Contact was re-established as soon as water was added to the soil and a tripotential error of ≤ 5 % indicated good data quality for the rest of the measurements.

Similar to the drying period, the changes in the AI were largest at the top of the profile and progressed downwards during the irrigation (Figure 4.4b). This is

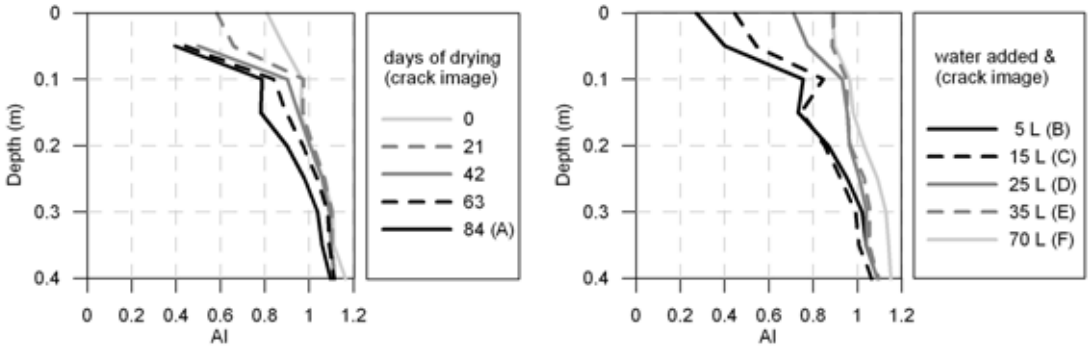

(a) (b)

Figure 4.4: Anisotropy profiles measured in the clay soil with a square array of 500 mm side length; a: During drying in three week intervals; b: During water application, the plotted anisotropy profiles were taken at the same time than the surface crack images shown in Figure (4.5), reference to the corresponding surface crack image is given in the legend.

consistent with the mechanism of infiltration of low intensity rainfall into cracked soil (Bouma and Anderson, 1977), with water flowing into cracks and reaching deeper soil layers once the infiltration capacity of the soil surface is exceeded. Throughout the water application, the AI profile returned to its initial state before the drying period. Differences between the initial AI profile and the AI profile at the end of the irrigation were less than 2 %, which is within the range of measurement error.

The observed changes in the anisotropy profile clearly show that drying and wetting of the soil profile influence the AI. To determine whether it is actual soil cracking or purely a variation in soil moisture that influences the AI, the development of the surface crack network needs to be examined. In the absence of other information, it is assumed that subsurface cracks are a continuation of the surface crack network and that subsurface crack dynamics are thus related to surface crack dynamics.

The majority of the surface cracks were established within the first 5 days of drying. Thereafter, only minor new surface cracks developed, while the present cracks slightly increased in width throughout the next 10 days, before the surface crack network became stagnant. With onset of the water application the surface cracks started to close with crack closure being complete after the application of 35 out of 70 L (Figure 4.5).

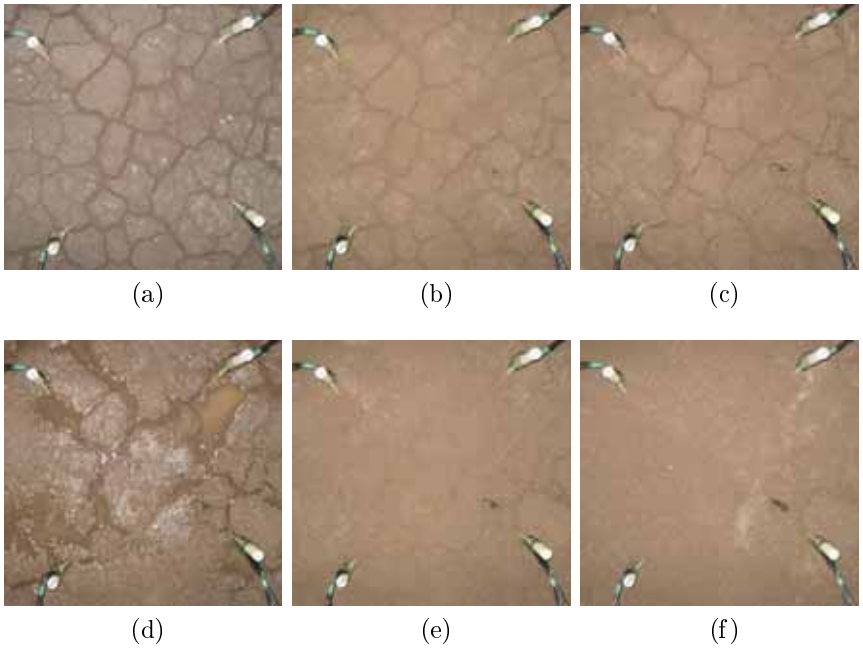

Figure 4.5: Surface crack network throughout the water application; a: Immediately before the irrigation; b: 6 minutes into irrigation, 5 L applied; c: 20 minutes into irrigation, 15 L applied; d: 32 minutes into irrigation, 25 L applied; e: 45 minutes into irrigation, 35 L applied; f: End of irrigation after 90 minutes, 70 L applied.

A comparison of Figures 4.4 and 4.5 shows that the main AI change during the irrigation occurred before the crack were closed, with the application of a further 35 L after crack closure resulting in only minor AI changes. As only 1.9 L of drainage occurred, the majority of this water must have been taken up by the soil. A further increase in soil moisture during the application of these 35 L after crack closure is also indicated by the decrease of the mean ρ_a measured with the square array from 36 Ωm to 31 Ωm. This is a significant change, considering that the mean ρ_a for the dry soil before the irrigation was only 44 Ωm.

The fact that no further change in AI occured during this increase in soil moisture, indicates that soil moisture changes after crack closure have a negligible influence on the AI. The observed soil crack dynamics were inevitably accompanied by soil moisture changes, however as soil moisture changes after crack closure had a negligible influence on the anisotropy profile, it is concluded that it is crack dynamics and not soil moisture change that dominates the AI.

AI deviations measured at the top of the soil profile were larger than those simu-

lated in Section 4.1 for crack networks forming in the same soil. This difference is most likely due to an increased cracking depth in the experimental data compared to the numerical model, which had 30 mm deep cracks. The AI deviations in agricultural fields, where certain crops can cause a preferential crack direction along the rows (Johnston and Hill, 1944), could be even stronger than the deviations reported in this section.

4.2.3 Conclusions from the Laboratory Study

Even though the crack networks forming in soils are significantly more complex than a single crack like resistor, the observations demonstrate that soil crack dynamics have a dominating influence on the anisotropy index. The changes in the index are most significant during surface crack closure and negligible thereafter. The observed soil crack dynamics were inevitably accompanied by soil moisture changes, however as soil moisture changes after crack closure had a negligible influence on the anisotropy profile, it is concluded that it is the dynamic behaviour of the cracks and not the changes in soil moisture that dominate the AI.

Chapter 5

Electrical Resistivity Tomography

After confirming the suitability of an anisotropy profile to detect soil cracking in the laboratory, its suitability needs to be tested under field conditions. In the uncontrollable environment of an agricultural plot, additional measures of the extent of soil cracking are needed to allow comparison with the results of the anisotropy profiles. With the lack of reliable methods to determine cracking depth in soils being the very reason for this investigation, the development of such additional measures becomes a necessary part of this study.

The present experimental set up consists of four subsurface electrode strings that could also be used to carry out 3D electrical resistivity tomography (ERT). Time lapse collection of ERT images during an irrigation event should allow the monitoring of water infiltration into the soil and thus the detection of potential preferential flow paths, which could be related to the extent of cracking. Furthermore, highly resistive regions in the ERT images collected in dry cracked soil, could give an indication of the extent and depth of cracking. ERT can therefore be used as an independent method to check the AI results, while it conveniently can be carried out with the same equipment that is used to measure anisotropy. To do so, an ERT measurement routine that utilises the same electrode set up that is used for the collection of the anisotropy profiles needs to be created.

5.1 Design of an ERT Measurement Routine

5.1.1 ERT image appraisal

The term 'resistivity tomography' refers to resistivity explorations with electrodes that surround the area of interest (Shima and Sakayama, 1987). While traditional methods use a relatively small number of measurements collected on a single line using a single electrode pattern (for example Acworth, 1999), electrical resistivity tomography (ERT) employs the collection of large, high density data sets using flexible electrode set ups (Slater et al., 1997; LaBrecque et al., 2004a). ERT allows any combination of surface, surface-borehole or borehole-borehole measurements to be made. By moving away from the standard surface measuring routines, a huge number of possible electrode configurations is introduced. The design of a suitable measurement sequence thus becomes an important part of an ERT survey. Commercially available measuring equipment such as the ABEM SAS4000 / ES10-64C package that was used for this study, allow any combination of measurements to be pre-programmed and run automatically. The problem then becomes one of deciding which particular combination is most beneficial.

An ideal measurement routine would measure all independent electrode configurations (Xu and Noel, 1993) at one moment in time. The next best option is a realistic compromise between acquisition time and an optimised selection of electrode combinations. Optimising the addressed electrode combinations in a measuring routine requires a measure of quality for the measurement results and the inverted resistivity model. Recently, there has been considerable work in developing appropriate methods for image appraisal: such as the calculation of sensitivity maps; linear approximations of parts of the model resolution matrix (MRM); or determining the volume of investigation (VOI) (Park and Van, 1991; Ramirez et al., 1995; Oldenburg and Li, 1999; Alumbaugh and Newman, 2000; Furman et al., 2002, 2003, 2004; Dahlin and Zhou, 2004; Stummer et al., 2004; Wilkinson et al., 2006; Oldenborger et al., 2007).

The sensitivity, which mathematically is expressed by the Frechet derivative (Mc-

Gillivray and Oldenburg, 1990), measures the influence of a certain region on the overall ρ_a measurement. The sensitivity of an image region is a function of the total electrical current that flows through the region, with high sensitivities indicating that a large fraction of the electrical current flows through the region and that the region will hence strongly influence the measurement. While sensitivity has been used to guide the selection of addressed electrode combinations (Furman et al., 2002, 2003, 2004) it does not contain any information about the data and modelling error nor about the influence of the inversion settings on the final solution. This information is included in the MRM and the VOI.

The MRM defines the area over which the inverted resistivity values in the image are averaged and ideally would be an identity matrix to indicate that averaging occurs only over one pixel. The VOI as defined by Oldenborger et al. (2007) on the other hand, is calculated by using two different starting models for an inversion. For each model cell the VOI is calculated by taking the ratio of the difference between the two inversion results and the difference between the two starting models. High VOIs indicate large differences between the two inversion results and hence poorly resolved cells, while small VOIs result from similar inversion results, which indicate well resolved data. An advantage of the VOI is that it is computationally inexpensive and in contrast to the MRM, can be calculated without any linear approximations. Miller and Routh (2007) demonstrated that the MRM and the VOI give similar information about the image resolution.

5.1.2 Selection of Electrode Configurations

For this study, the electrode configurations are limited to cross borehole measurements between the four probes, which leads to the collection of data along the six possible measuring planes between the four corners of the measurement square (Figure 5.1). Measurements involving electrodes on all four probes were not used due to their low signal strengths; and measurements with all four electrodes in one borehole were also not incorporated as these are susceptible to disturbance from the wires in the probes

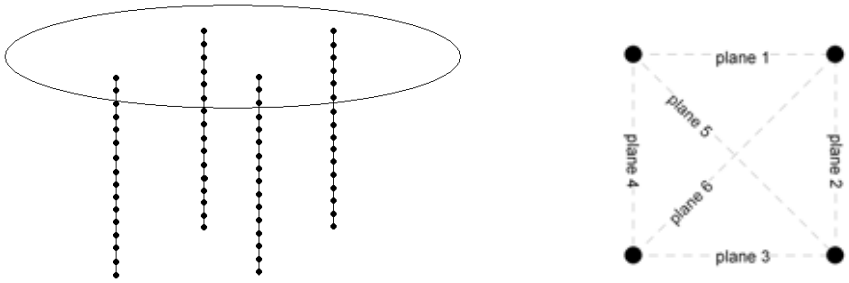

(a) (b)

Figure 5.1: Electrode arrangement on four vertical strings that are installed in the corners of a surface square.

and are thus very noisy (Acworth and Jorstad, 2006). As recommended by Bing and Greenhalgh (1997, 2000), dipole-dipole measurements with C_1 and P_1 on one probe and C_2 and P_2 on the other were chosen for this study.

Next, the spacings between the current and potential electrodes as well as the depth differences between the active electrodes on both electrode strings were selected. Following the approach of Furman et al. (2002, 2003, 2004), the sensitivity distribution within a homogeneous subsurface for all possible spacings and depth differences were simulated. An electrode string separation of 550 mm and an electrode separation on the strings of 75 mm were chosen for the simulations. Current electrodes were located above the potential electrodes during all simulations. Simulations were carried out with *Res2Dmod* (Loke, 2002), which allows separate calculation of the sensitivity distribution resulting from one electrode combination at a time. To batch process the task of sensitivity modelling, a *Python* script was written to create individual *Res2Dmod* input files for the 1282 electrode combinations that, considering the discussed restrictions, were possible between two strings consisting of 16 electrodes each. Sixteen electrodes per string were chosen to make optimum use of the possible 64 electrode connections of the ABEM SAS4000 / ES10-64C package. To overcome the lack of an automated read in function in *Res2Dmod*, a *Visual Basics* script was created to automate the use of the graphical user interface of *Res2Dmod* for reading

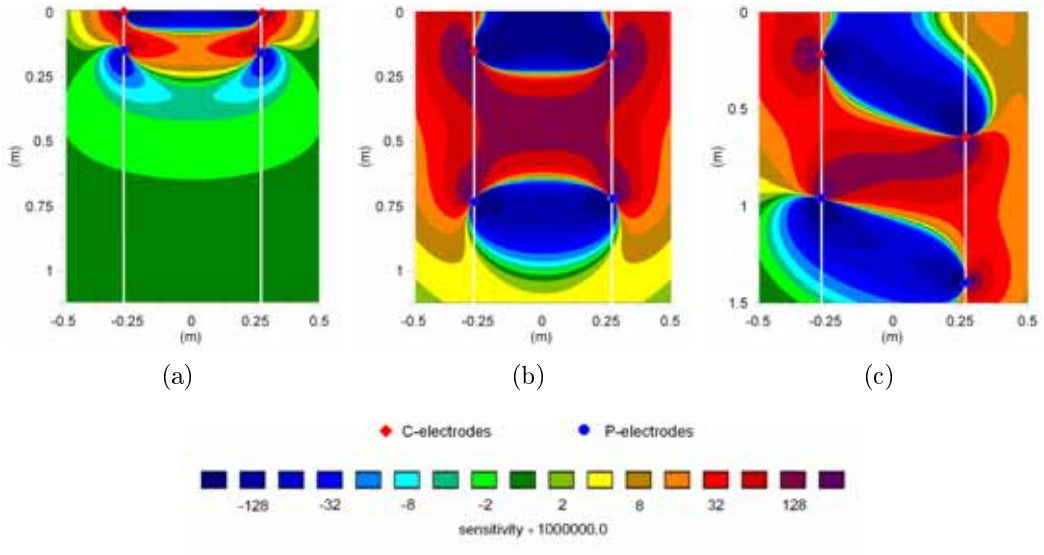

(a) (b) (c)

(d)

Figure 5.2: Selected sensitivity distributions due to individual electrode arrangements (electrode strings and active electrodes in white); a: Inter electrode spacing of 15 mm, no depth difference between electrodes on opposite strings; b: Inter electrode spacing of 600 mm, no depth difference between electrodes on opposite strings; c: Inter electrode spacing of 600 mm, 300 mm difference between electrodes on opposite strings.

the input file, modelling the sensitivity distribution and saving the results.

A selection of the simulated sensitivity distributions is shown in Figure 5.2. In general, the smaller electrode spacings resulted in high sensitivities close to the electrode strings and showed lower sensitivities towards the centre of the two strings. Larger spacings on the other hand resulted in more evenly distributed sensitivities.

In addition to a high accumulative sensitivity of the selected electrode configurations it is important that the resulting sensitivities are homogeneously distributed throughout the measurement domain to avoid over or under representation of image regions. To facilitate the selection of the most sensible electrode configurations, a quality indicator (Q) was chosen and the possible electrode arrangements were ranked accordingly. Q was based on the mean sensitivity in the area between the two probes as well as on the standard deviation of the sensitivity within this area, and was calculated as

$$Q = \overline{S} - S_{RMS}, \tag{5.1}$$

where $\overline{S}$ is the arithmetic mean of the sensitivity of the model cells between the two electrode strings and S_{RMS} is the corresponding standard deviation. According to the quality indicator, electrode arrangements with 3 to 7 times the minimum electrode spacing (75 mm) between current and potential electrodes, and depth differences of 0 to 5 electrode spaces between the active current electrodes on both electrode strings were favourable.

The ABEM SAS4000 / ES10-64C package allows measurements with a maximum of four channels. To make full use of these measuring capabilities, the final selection step for the electrode combinations was to assure that the selected electrode combinations could be arranged in four channels. This meant electrode combinations were selected so that for each current electrode pair the potential was measured between four (or a multiple of four) potential pairs.

Based on these considerations two measurement protocols were selected. A short protocol (216 measurements in 3.5 minutes), which was designed for ERT measurements during irrigation events when resistivity changes occurred rapidly and a long protocol (2784 measurements 45 minutes) for a higher resolution surveys during more stable resistivity conditions.

In practise, the current flow, and thus the sensitivity distribution and image resolution, is influenced by the resistivity inhomogeneities in the subsurface. Theoretical considerations can therefore never give the true sensitivities and image resolutions, which makes testing of the selected electrode arrangements under field conditions necessary. Before the two selected measurement protocols could be further refined and tested in the field, robust resistivity probes for field use needed to be designed and installed. The probe design and field installation are described in Section 5.2 and 5.3, before the field testing of the electrode arrangements is described in Section 5.4.

5.2 Construction of Probes

In contrast to surface electrode set ups, cross borehole electrode strings, which allow the collection of AI and ERT profiles, are not commercially available. Furthermore

the unique environment of the cracking clay soils and the relatively small area of investigation calls for a unique design of the electrode strings. Throughout this study the electrode string design was successively advanced due to trial and error insights about the necessary design criteria required for field work under dynamic and chemically aggressive soil conditions. A summary of the lessons that were learned from previous string designs is included in Appendix B.

Here, the final string design that was used in the two field experiments is described. For use in the field two sets of strings were constructed, they consisted of 16 ring shaped electrodes each, with an inter electrode spacings of 75 mm for the short field set and an inter electrode spacing of 100 mm for the long field set. All electrodes (Figure 5.3a) had a diameter of 38 mm and were made from stainless steel grade 316, which provides a good balance between corrosion resistance and material related measurement error (Labrecque and Daily, 2008). Strings were assembled from the bottom up. Electrodes were consecutively pushed onto an insulating fibreglass (15 mm diameter) core followed by a piece of clear plastic tube (20.5 mm inner diameter, 22,5 outer diameter), which maintained the 75 mm and 100 mm electrode separation (Figure 5.3b). Each electrode was connected to an individual insulated wire. The wires were lead along the probe between the fibreglass core and the clear plastic tube through holes in the electrode rings (also Figure 5.3b). At the top of the probe, the wires were bound into a cable that terminated in a 32 pin connector (2 probes to each connector). Once assembled, the probes were waterproofed by filling the void around the wires with silicon (Figure 5.3c). Controlled silicon filling was facilitated by the clear outer tube of the strings.

5.3 Probe Installation

5.3.1 Borehole Spacing

To successfully carry out ERT between two boreholes, a suitable borehole spacing needs to be chosen. The best image resolution for cross borehole measurements is

(a) (b) (c)

Figure 5.3: a: Stainless steel electrode rings (38 mm diameter); b: Two individual electrodes pushed onto a fibreglass rod and separated by clear plastic tube; c: Waterproofing of probes by filling the void around the wires with silicon.

generally found for measurement planes with the smallest width to height ratio and ratios of 0.50 to 0.75 have been recommended to maintain high image resolution (LaBrecque et al., 1996; Slater et al., 1997; Bing and Greenhalgh, 2000). In addition, for the small scale measurements used in this study, care must be taken not to violate the assumption of point current sources during the inversion routine (Loke, 1996-2004). The assumption of point electrodes is only valid if the spacing between the current sources is sufficiently large compared to the size of the electrodes. The bore hole separation, should therefore result in ratios between the electrode diameter and the electrode separation that are commonly used in surface measurements, while at the same time the hole separation should result in a width to height ration that maintains high image resolution between the probes. Next to assuring successful ERT measurements, the borehole spacing needs to be large in comparison to the crack spacing to assure representative AI measurements Taylor and Fleming (1988).

The square arrangement of the electrode probes (Figure 5.1) results in two different width to height ratios (one ratio for planes along the side of the square and one for the diagonal planes through the centre of the square). To facilitate the selection of a suitable side length of the measurement square, the sensitivity distribution between two boreholes in a homogeneous half space was simulated for a variety of borehole spacings. Simulations were run in *Res2Dmod* for the short selection of electrode arrangements with the short field probes. Borehole spacings between 0.3 and 1.1 m were used in the simulation, which is equivalent to a width to height ratio of 0.25 to

0.90 for the short field probes.

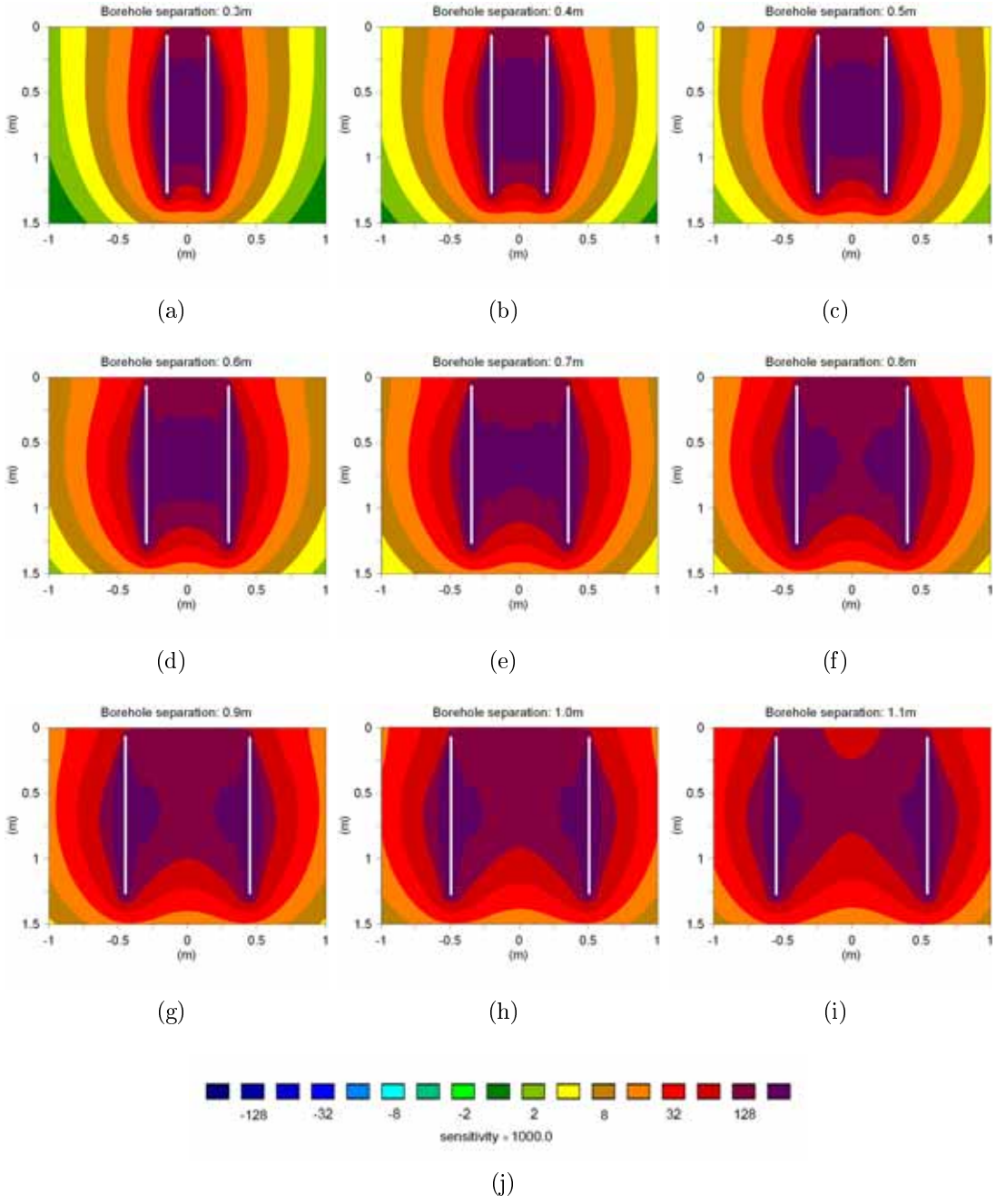

Figure 5.4: Sensitivity distribution in a homogeneous half space simulated for the short probe set at borehole spacings from 0.3 m to 1.1 m.

Based on the simulation results (Figure 5.4), a measurement square with a side length of 550 mm was chosen for the short field probes, which resulted in a probe separation along the diagonal of the square of 780 mm. Correspondingly the chosen measurement square for the long probes had a side length of 730 mm. Figure 5.4 shows that these measurement squares resulted in comparably high sensitivities in

the centre of the image, while the ratio of the electrode diameter to the smallest possible current electrode spacing of 550 mm remained in a range that is typically encountered in surface measurements. The same ratio between the electrode length and probe separation would be encountered during surface measurements with an electrode spacing of 2 m and an electrode insertion depth of 0.14 m.

The error that results in the calculation of ρ_a, due to the diversion of the current electrodes from a point source, can be estimated following the approach used by Day-Lewis et al. (2006). They calculate a geometric factor for the true dimensions of the current electrodes (K_{true}), which, if compared to the geometric factor of a point current source (K_{point}), gives an indication of the resulting error during the forward modelling of the inversion routine. To calculate K_{true} the area of the current electrode is discretized into a series of near point electrodes and a geometric factor is calculated for each of these near point electrodes. According to the fraction of the initial current source that the discretized near point electrode represents, the resulting geometric factors are then multiplied with a fraction between 0 and 1, before K_{true} is calculated as the sum of the geometric factor fractions. For the short and long probes, the difference between K_{point} and K_{true} for the smallest electrode spacing used in the measurement routine is 1.91% and 1.04%, respectively. As this difference is below the recommended maximum measurement error for time lapse series of 3 to 5% (Miller et al., 2008), it is concluded that the error introduced due to the violated point assumption is insignificant.

In addition, the selected side lengths for the long and short probes are large in comparison to the average crack spacing that was observed in the clay soils in Chapter 4 (∼40-50 mm). The selected borehole spacings are therefore also suitable for AI measurements.

5.3.2 Probe Insertion into the Soil

Vertical positioning of the probes is even more important during the field experiment. Firstly, because the longer probes increase the position error that results from sub

vertical probe installation and secondly because the inversion routine used for ERT requires accurate determination of the distances between the electrodes (Oldenborger et al., 2005).

The holes for probe installation in the field were augered with a hand held 40 mm diameter spiral auger as done for the soil lysimeter experiment in Section 4.2 on page 40. To assure vertical augering the auger was held in place by a levelled tripod guide (Figure 5.5a). The augered material was collected and worked into a putty textured soil water paste (Figure 5.5b), which was used to cover the probes to assure a tight fit of the probes in the augered holes. Before the probes were pushed into the holes the walls of the auger holes were wetted and softened. This allowed smooth insertion of the probes, which favoured good electrical contact between the electrodes and the surrounding soil matrix. Using a soil paste from the augered material as fill material ensured a minimal resistivity contrast between the augered holes and the soil matrix, and hence minimal borehole effects (Nimmer et al., 2008). To monitor the electrical contact between the soil and electrodes, the measurement error throughout the irrigation period was investigated. Measurement error was determined by stacked as well as by reciprocal measurements. The stacked error was calculated as the standard deviation from six stacks, which is six repeat measurements. The reciprocal error on the other hand is based on the concept of reciprocity (Carpenter and Habberjam, 1956), which states that swapping the electrodes between C and P makes no difference to the measured resistance. Here the reciprocal error is defined as the relative difference between two reciprocal measurements.

5.4 Field Testing of the ERT Measurement Routine

Once the electrode strings were assembled and installed in the field, the short and the long electrode selection made in Section 5.1.2 could be further refined and tested.

(a) (b) (c)

Figure 5.5: a: Tripod guide to hold spiral auger in place during augering; b: Mixing of augered material into patty textured paste to cover electrode strings; c: An electrode string ready to be inserted into the augered hole.

5.4.1 Refinement of Electrode Configurations

In addition to an optimised selection of electrode arrangements, a good ERT measurement routine needs to minimise electrode polarisation. Electrode polarisation occurs due to charge accumulation at the interface between the current electrodes and the less conducting ground. Dahlin (2000) showed that the electrode polarisation can be magnitudes larger than the induced signal and can take tens of minutes to decay. Measuring the potential difference with a charged up electrode can introduce significant measurement error. Even though modern equipment is very efficient in correcting for charge accumulation (Merriam, 2005), one should avoid direct reuse of a current electrode as a potential electrode in a measuring sequence. It should be noted that electrode polarisation errors are a particular problem in fine-grained silts and clays that have significant cation exchange capacity. Most fertile soils used for agricultural production are high in clay and silt content. Therefore this problem is widely encountered (but frequently not recognised) in the use of electrical resistivity techniques for agricultural investigations.

To minimise errors due to electrode polarisation, the minimum time interval between reusing a current electrode as a potential electrode was determined. This was done using the concept of reciprocity (Carpenter and Habberjam, 1956). A measu-

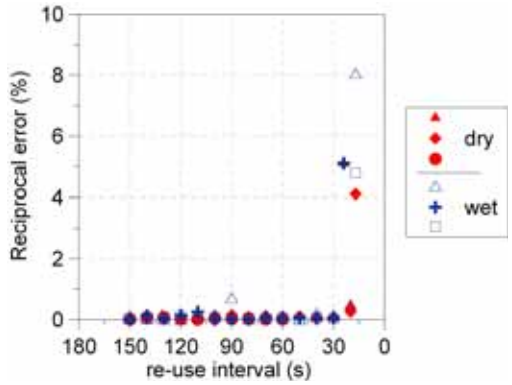

Figure 5.6: Investigation of electrode charge up effects: Reciprocal error in dry and wet soil for different time intervals between reusing a current electrode as a potential electrode. Shown are three replicate measurements for each soil condition.

rement protocol with waiting periods of 6 to 300 seconds between reciprocal measurements was generated and run three times in dry and in wet soil conditions in the field, where resistance between 0.1 and 13.2 Ω were measured. The resulting reciprocal error (Figure 5.6) showed an increase for waiting periods of less than 30 seconds. Consequently, the selected electrode configurations were arranged to ensure at least 30 seconds between reuse of a current as a potential electrode. This was achieved by positioning the current electrodes above the potential electrodes and moving the electrodes downwards during the measurements.

5.4.2 Image Resolution

Once the measurement protocols were finalised, the short and long protocol were run in the field and their volume of investigation (VOI) (Oldenborger et al., 2007) was calculated in *Res3Dinvx64* (Loke, 2008). This allowed assessment of the ERT image resolution for the two protocols under field conditions.

Figure 5.7 shows the VOI for the short and long protocols respectively. Two x-z slices are shown for each protocol, the first slice is cut between probe one and two while the second slice is cut in the centre of the model area. For both protocols, high VOI indices indicate that low model reliability was found next to the probes. This can be explained with the large variation in bulk resistivity in this area, which are introduced by the different building materials of the probes and the probe soil

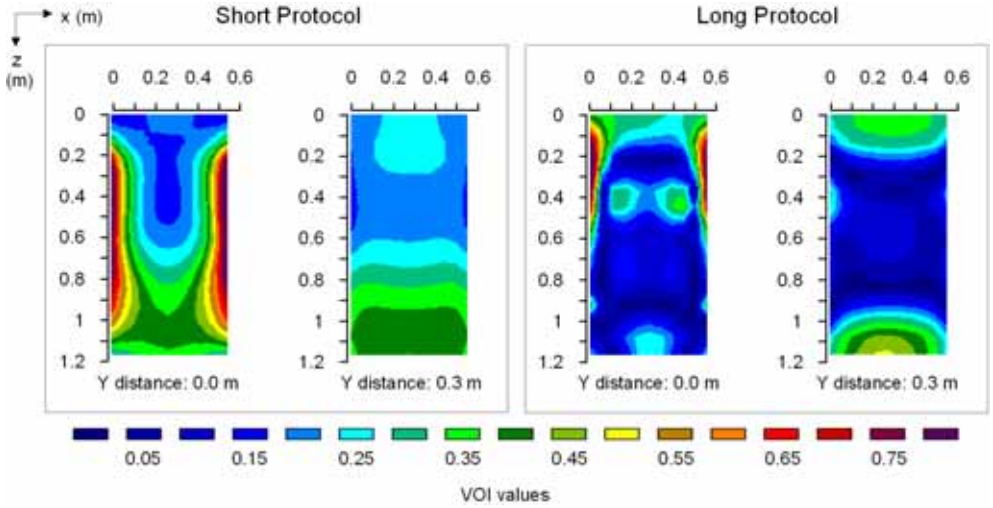

Figure 5.7: Volume of investigation indices for the short and long protocol, illustrated on x-z slices between probes 1 and 2 and in the centre of the modelling area

interface. Due to the greater number of data points in the long protocol, the VOI indices are lower, indicating a higher model reliability. Oldenburg and Li (1999) and Oldenborger et al. (2007) used a critical value of 0.2 to distinguish between high and low resolved areas. Following this approach gives high resolved areas throughout the majority of the model area for the long protocol, and if the area immediately next to the probes is excluded, for about half of the model area of the short protocol. Inverted resistivity values obtained outside these regions have a lower reliability.

For ρ_a measurements undertaken during the application of water, short collection times are crucial and the errors introduced by bulk resistivity changes during the measurement are not well understood (Slater et al., 2002). The VOI indices for the short protocol could be improved if more data points were collected instantaneously; more collection channels could improve the model resolution without increasing the measurement time. However, for this research it is believed that a satisfactory compromise between model resolution and data collection time was achieved for the short protocol. For measurements during transient processes the approach suggested by Zhe et al. (2007) of measuring the potential at all non current electrodes simultaneously could be a very efficient method for improving the model reliability. However, such equipment is not available for field use at present.

Chapter 6

Field Measurements in Sorghum

Field measurements were carried out in the growing season 2007/08 in a sorghum field planted on cracking soil. The aim of this experiment was to determine whether the relationship between surface soil cracking and AI deviation that was observed in the cracking soil in the lysimeter is also valid under field conditions. In addition to the measurement of anisotropy profiles, 3D electrical resistivity tomography (ERT) data were collected. The inverted ERT images gave information about the occurrence of preferential flow, and the presence of highly resistive zones highlighted the extent of cracking. Comparison of the anisotropy profiles and the ERT data confirmed the relationship between cracking depth and depth of AI deviation, which had been observed for simple cracks in Section 3.1 and 3.2. In addition to qualitative crack information, a field AI profile does allow the determination of a cracking depth range.

6.1 Methods

6.1.1 Field Measurements

For the growing season 2007-08 the short field set of resistivity strings, with an inter electrode spacing of 75 mm, was installed at a field site 25 km south east of Narrabri, NSW. A location map and a map of the field site are shown in Figure 6.1. The resistivity probes were installed in a section of the southern field, which has a loamy

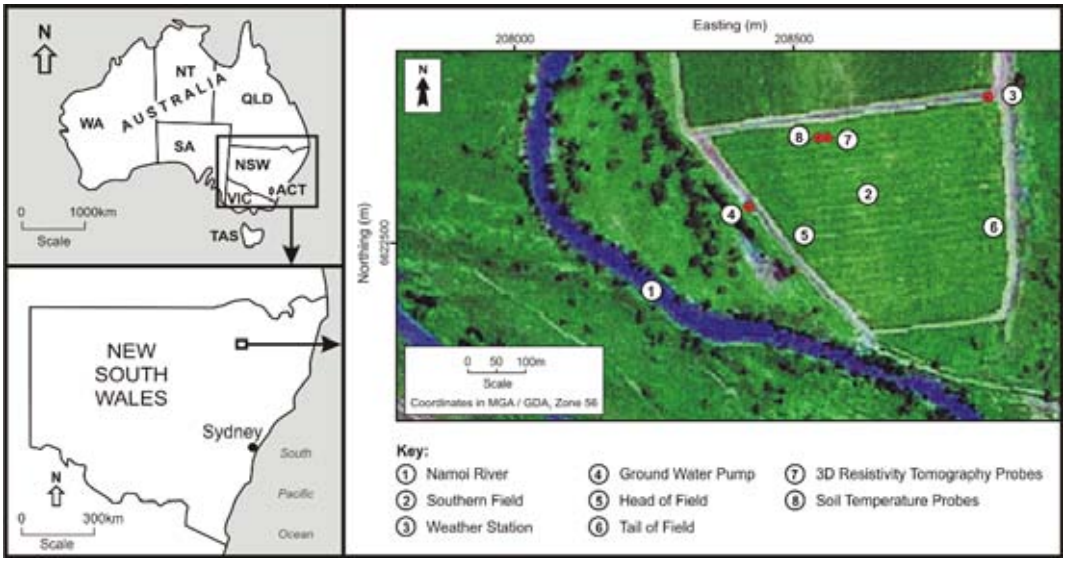

Figure 6.1: Fieldsite adjacent to the Namoi River in NSW, Australia

clay top soil. Grain size determinations on soil samples of the first two meters of the profile gave a composition of 41 to 49 % clay, 20 to 21 % silt, and 31 to 41 % of sand. Drilling logs indicate that the silt content in the profile decreases at depth greater than 2 meters, while the sand content increases. Starting at 4 meters depth, sand and gravel is introduced into the profile.

After a pre-irrigation, the southern field was planted with *Pioneer Bonus MR* grain sorghum on the 5th and 6th of October 2007. Planting was carried out in 1 m spaced rows with a target plant population of 200 000 plants per hectare. Installation of the resistivity probes took place on the 1^{st} of November 2007, 20 days after plant germination.

Installation of the probes took place as described in Section 5.3. The strings were installed forming a square with a side length of 550 mm, with the first and last electrode of each string located at 30 mm and 1155 mm, respectively. The measurement square was centred around a row of plants with the sides of the square parallel to and orthogonal to the plant rows (Figure 6.2).

The sorghum at the field site was irrigated twice in the monitored season. During an irrigation event every second row was flooded for 12 hours, ten rows at a time. This resulted in an irrigation duration of 11 days for the 14.8 ha field, which consisted of 440 rows. Irrigation of the rows containing the resistivity probes took place on the

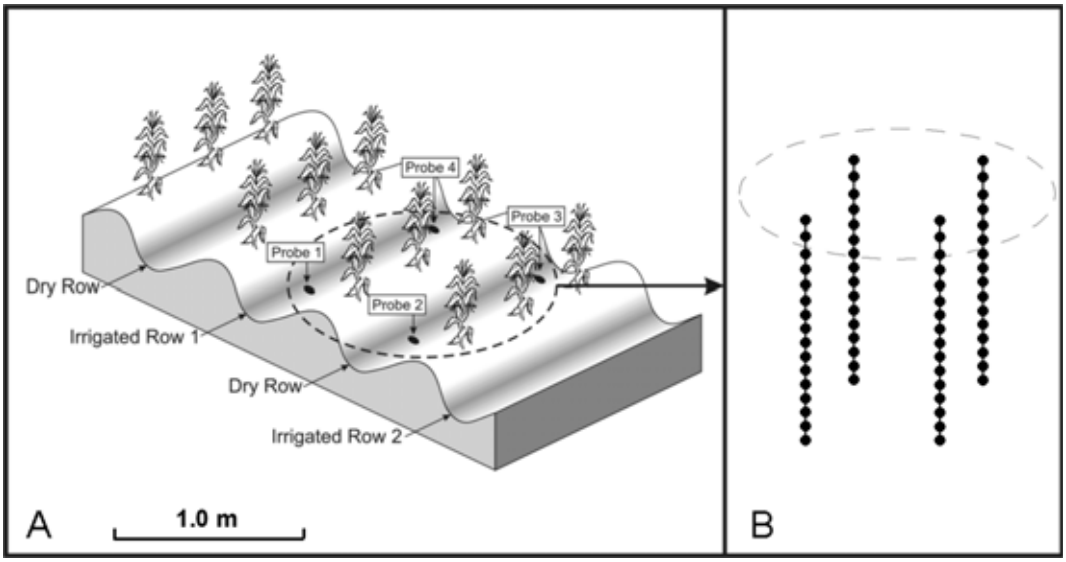

Figure 6.2: Resistivity probe location in the field

15/11/2007 from 07:00 to 19:00 and on the 2/12/2007 from 10:30 to 22:30.

The groundwater that was used for irrigation had an EC of ∼45 mS/m and was pumped at an average rate of 18 L/s. Even application of the entire pumped water during an irrigation event, not taking into account channel water losses, would have resulted in a water application of 100 mm. However, observations made during irrigation showed that the water was not applied evenly between the head and tail ditch and that water was lost to tail runoff.

In addition to these two irrigation events, a third watering took place on the 15/01/2008, two weeks before the sorghum was harvested. Surface cracks of up to 30 mm width indicated significantly drier soil conditions at the onset of this watering than before the previous two irrigations, where surface cracks did not exceed a width of 2 mm. For this third irrigation a two row wide application area was confined with two soil walls, which were located 5 m up and down gradient of the electrode strings. From 16:20 to 19:00, 2200 L of water were pumped from the side ditch of the field onto the 20 m^2 area. The applied water had been pumped from the ground 3 days prior to the application and hence had an increased temperature compared to the freshly pumped ground water for irrigations 1 and 2. Due to the cracked soil condition, the applied water did not entirely remain in the confined area, as some water was lost into the cracks and reached soil outside of the confinement. To minimise water losses

into the cracks, the first 200 L were pumped at a rate of 200 L/h before the pumping rate was increased to 1200 L/h for the remaining 2000 L. Uniform application of the entire applied water would have resulted in an water application of 110 mm.

The short, the long, and the square protocol were run once before the onset of the irrigation and immediately after the irrigation when the water stopped flowing. After the irrigation, the three protocols were run every 2 hours for the first 24 and every 4 hours for the next 24 hours, using a time lapse setting on the instrument. During an irrigation event, when continuous change in soil bulk resistivity was expected, the short protocol (3.5 minutes) was run every 20 minutes in time lapse setting. To minimise the measurement time for the short protocol run during the irrigation, the instrument was set to record a single potential difference. By contrast, for all other measurements, 4 four potential differences were recorded.

To investigate the downward movement of irrigation water, soil temperature was measured every 15 minutes at 150, 300, 450, 850, and 1200 mm depth using a probe comprising individual HOBO Water Temp Pro v2 sensors. The probe with the temperature sensors was located 2 m up-gradient of the resistivity probes in the same crest as the probes. A weather station was located at the field site shown in Figure 6.1, which recorded rainfall using a tipping bucket gauge as well as air temperature and other climate variables.

6.1.2 Data Inversion

The collected ρ_a data were inverted with *Res3Dinvx64* to determine the most likely subsurface resistivity distribution which gives a model response that agrees with the measured ρ_a values. *Res3Dinvx64* uses a finite difference model of the subsurface. During the inversion the model resistivities in the finite difference grid are automatically adjusted so that the response of a forward model converges towards the measured data (Loke and Barker, 1996). To limit the problem of non-uniqueness, which arises from the fact that an infinite number of model resistivity distributions can give rise to the same measured data, *Res3Dinvx64* uses a smoothness constraint. This constraint

aims to find the smoothest possible solution that still fits the data within a predefined error threshold. The default smoothness constraint used by *Res3Dinvx64* is the least square or L_2 smoothness constraint, which aims at minimising the square of the spatial resistivity changes in the inverted bulk resistivity model (deGroot Hedlin and Constable, 1990). For a subsurface with sharp boundaries, as in cracked soil, Loke et al. (2003) recommend the use of L_1 or blocky inversion, which aims at minimising the absolute changes in model resistivity. They note that the use of L_2 inversion under these conditions smears out the boundaries and results in too low and too high inverted resistivity values. However, the blocky inversion caused unstable inversion results for the recorded apparent resistivity distributions, which manifested itself in meaningless time series results. Therefore the smoothness constrained inversion was used, and the resulting smearing of sharp resistivity boundaries were accepted.

The inversion routine was set to use the Gauss-Newton method rather than the faster quasi Gaus-Newton method. The Gauss-Newton method re-calculates the sensitivity matrix at each iteration step, which, as Dahlin and Loke (1998) have shown, is superior for narrow vertical structures and large resistivity contrast, which both occur in cracked soil. Based on the balance between stability and model resolution, a block size of 0.5 x 0.5 the minimum electrode spacing has been recommended (Sasaki, 1992; Shima et al., 1996) and was hence used in this study. The data were inverted in a constant depth layer model (Loke, 2008) with the default flatness filter. Data points with a measurement error of ≥ 3 % were excluded from the inversion.

Res3Dinvx64 assigns one resistivity value to each model cell, which includes the assumption that the resistivity does not show any directional dependence. A violation of this assumption, which could easily occur in cracked soil, might cause artifacts in the inverted image (Kim et al., 2006). Within a model block that contains a crack, the resistivity parallel to that crack would differ to the resistivity orthogonal to the crack. This anisotropy can be included in the inversion routine by use of a resistivity tensor instead of a scalar (LaBrecque et al., 2004b; Herwanger et al., 2004; Kim et al., 2006). However, inversion routines that allow the use of a resistivity tensor are

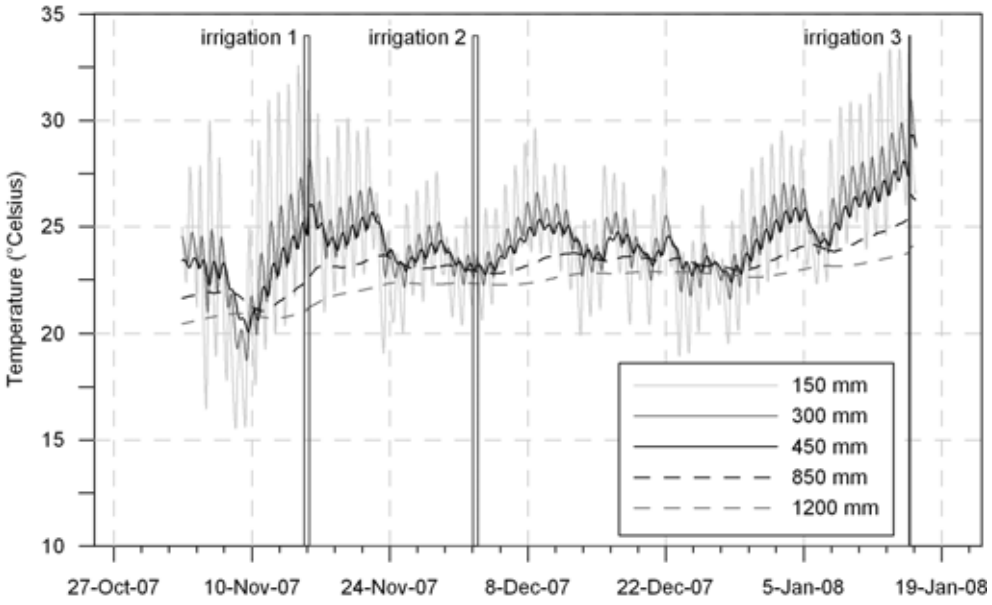

Figure 6.3: Soil temperature at different depths throughout the growing season 2007/08.

not yet commercially available. Furthermore, incorporating the temporal and spatial anisotropy variations that occur in a cracking soil, is an inversion challenge that has not yet been met. Keeping these limitations in mind, the use of *Res3Dinvx64* was considered acceptable for the goals of this research.

The soil temperature data measured next to the resistivity probes show daily temperature fluctuation to a depth of 450 mm (Figure 6.3). In time lapse analysis, the influence of temperature on the resistivity must be considered (Mansoor, 2007). Therefore a temperature correction is carried out after completion of the inversion, taking into account the daily and seasonal soil temperature changes shown in Figure 6.3.

Hayley et al. (2007) have shown that, for the temperature range relevant to near surface measurements, a linear approximation of the temperature dependence shows a good fit with observed data and report a resistivity decrease of 1.8 to 2.2 % with each degree rise in Celsius. Similar values have been reported in other studies (Coleman and Hendrix, 1949; Campbell et al., 1949; Rinaldi and Cuestas, 2002). In the absence of other information a 2 % decrease in resistance with every degree increase in temperature is thus assumed and the data are corrected to a standard temperature

	Irrigation 1		Irrigation 2		Irrigation 3	
stacked error (%)	dry soil	wet soil	dry soil	wet soil	dry soil	wet soil
mean	0.11	0.16	0.09	0.12	0.19	0.08
1st quartile	0.01	0.03	0.01	0.02	0.02	0.01
median	0.05	0.08	0.04	0.06	0.05	0.03
3rd quartile	0.13	0.20	0.12	0.13	0.09	0.10

Table 6.1: Mean, first, second and third quartile error for measurements made during the three irrigation events, separated for dry and wet soil conditions.

of 25° Celsius. A linear approximation of soil temperature was obtained for the depth of each model layer utilising the measured soil temperature at 150, 300, 450, 850 and 1200 mm as well as the air temperature measured at the weather station. The resistivities of the model cells were then corrected to 25° Celsius using the temperature for the corresponding time and depth.

The inverted and temperature corrected data were plotted with *EarthVision* (Graphics, 2009), which allowed interactive 3D data visualisation. Minimum tension griding was used to interpolate between the model blocks of the inverted model.

6.2 Results and Discussion

The average error (recorded by the ABEM SAS4000) for all protocols run during each of the three irrigation events is shown in Table 6.1, separated for dry and wet soil conditions. The majority of the data points have a measurement error below 0.5 %, and the recommended repeatability error for time lapse series, of 3 to 5 %, (Miller et al., 2008) is only exceeded for a few data points during measurements in the very dry soil before irrigation 3. Here, the exclusion of measurements with a stacked error of more than 3 % led to the exclusion of 40 out of 2784 measurements for the long protocol and 4 out of 216 measurements for the short protocol, which is less than 2 % of the measurements. Except for the very dry soil conditions before irrigation 3, the stacked error decreases throughout the growing period, which could be due to improved settling of the soil around the probes over time (LaBrecque et al., 1996).

The third quartile error for the dry soil before irrigation 3 shows the lowest value

of third quartile errors in the list, which highlights that the increased mean error is due to a few measurements with large errors, while the remaining data points show high repeatability. These few high errors are most likely due to bad electrode contact with the soil of a particular electrode due to soil shrinkage. Indeed, all of the excluded measurements involve at least one electrode which is located at the top of a probe where the maximum amount of shrinkage occurs. The mean reciprocal error for the three irrigation events is 1.4 times larger than the mean stacked error for the three irrigation events. This moderate difference between stacked and reciprocal error indicates low systematic measurement errors. Good data quality is also indicated by the tripotential error (Equation 2.10) which was $\leq$5 % for all measurements with the square array. The low stacked, reciprocal and tripotential errors indicate that the probe design and probe installation procedure were successful in establishing electrical contact between the electrodes and the shrinking soil.

Figures 6.4a-d show the inverted resistivity distribution before irrigations 1, 2, and 3 as well as for a moist soil profile after an irrigation event. The corresponding anisotropy profiles are shown in Figure 6.4f. The resistivity of a soil profile is a function of a variety of soil parameters (refer to Section 2.2). However, as the resistivity changes that were observed throughout this experiment were directly related to drying and irrigation events, it is reasonable to assume that they are dominated by soil moisture changes and potentially by subsequent changes in the extent of soil cracking. A comparison of Figure 6.4f and Figures 6.4a-d suggests a relationship between the soil moisture and the AI deviation, with a decrease in soil moisture relating to an increase in the AI deviation. This relationship is not surprising, as the formation of shrinkage cracks is directly related to soil drying, and it confirms the observations made in the soil lysimeter experiment in Section 4.2, where the AI deviation increased throughout the soil drying period.

The relationship between the deviation of the anisotropy profile and the degree of surface cracking that was observed in the soil lysimeter experiment is also evident under field conditions. The observed width of surface cracks before irrigations 1

and 2 varied between 1 and 2 mm, while surface cracks of a width of up to 30 mm were observed before irrigation 3. This is consistent with the measured AI profiles. Before irrigations 1 and 2, the AI deviation relative to the moist soil profile is minor within the first 480 mm and negligible at greater depth, while the AI deviation before irrigation 3 is well established throughout the entire measuring depth except at the last measuring point at 1155 mm.

To advance the conclusions made in Chapter 3, it is necessary to investigate whether the relationship between the total crack depth and the depth of the AI deviation, which was observed for the single crack like resistor, is also valid for crack networks in natural soils. To do so, the AI results need to be compared to additional indicators of the maximum depth of cracking, such as the changes in inverted resistivity throughout the irrigation events (shown in Figures 6.5, 6.6 and 6.7). Tracking the infiltration of the irrigation water in the inverted images allows the detection of potential preferential flow paths, and is hence an indicator of the extent and depth of cracking.

The propagation of the bulk resistivity change during irrigations 1 and 2 differs to the propagation observed during irrigation 3. During irrigations 1 and 2 the resistivity change is entering the model area from the west (the head of the field) and is propagating down gradient along the irrigated furrow, which runs at the south (left) of the plant row, as well as downwards into the profile. Additionally, the change also spreads laterally from the irrigated furrow into the plant row and towards the non irrigated furrow at the north of the image. While some preferential flow through small shallow cracks might have taken place during irrigation 1 and 2, the wetting process during these two irrigations appears to be dominated by matrix flow.

During irrigation 3, where the furrows to both sides of the plant row are flooded, the resistivity changes occur from the bottom upwards. This indicates that water flowed into the soil cracks, resulting in crack filling and crack closure from the bottom up. Such infiltration behaviour is typical for an 'internal catchment' in cracked soil as described by Van Stiphout et al. (1987). The soil at the top of the profile would

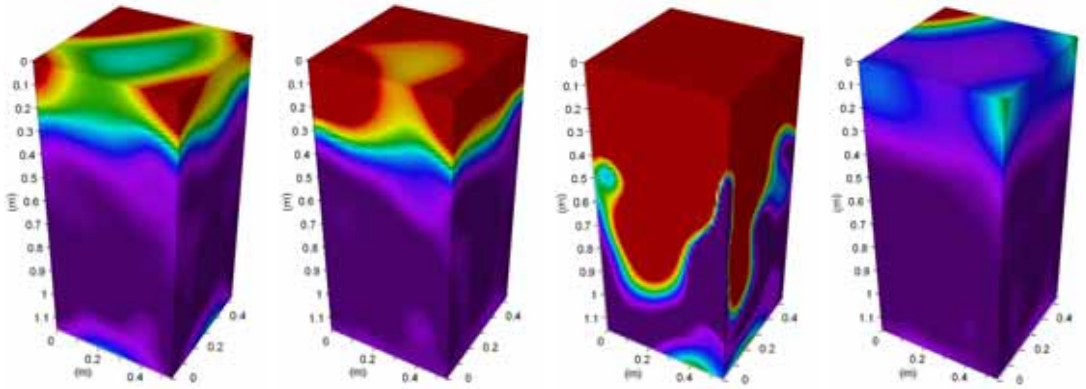

(a) (b) (c) (d)

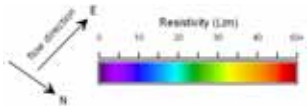

(e)

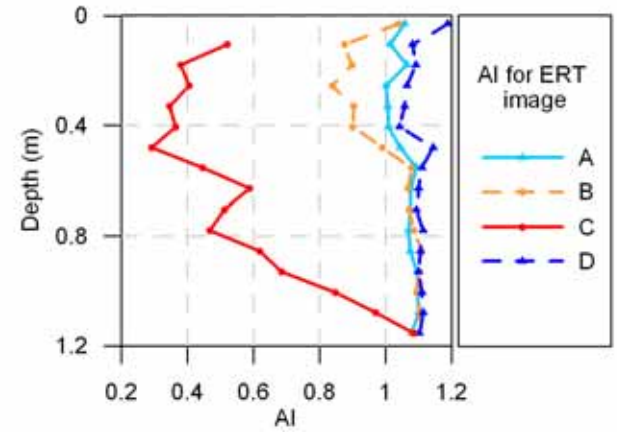

(f)

Figure 6.4: a-d: Inverted 3D resistivity distribution before irrigations 1, 2, 3, and for moist soil after an irrigation event, respectively; e: Resistivity legend for a-d; f: Corresponding anisotropy profiles.

have taken up some of the water that is flowing past. However, this soil moisture change is not detected, as the presence of the cracks in the soil are dominating the soil's resistivity response. The bulk resistivity at the top of the profile is only reduced once the cracks at this depth are closed or at least are filled with water.

Cracks throughout the soil profile are not the only potential pathway for preferential flow. Other soil voids, such as worm holes or plant root channels do also provide pathways for water flow (Beven and Germann, 1982). However, as the pre-irrigation soil moisture content (indicated in the inverted resistivity images collected before the three irrigation events) is significantly lower before irrigation 3 and as the surface cracks before irrigation 3 were significantly wider, it is reasonable to assume that soil cracks were the dominating paths for the preferential flow during irrigation 3. The two different infiltration behaviours between irrigations 1 and 2, and irrigation 3, emphasise the increased extent and depth of cracking before irrigation 3. This is also shown in the increased AI deviation in Figure 6.4f.

Another indicator of cracking depth can be obtained by investigating the high resolution images that were collected with the long protocol (Section 5.1) before and after each irrigation event. The smoothness constraint in the inversion hampers the exact location of individual cracks in the inverted resistivity images (Samouelian et al., 2003). However, zones with very high resistivity anomalies are likely to be affected by soil cracks and can thus give information about their extent and depth.

Figures 6.8a-c shows the areas of the inverted resistivity model that have a bulk resistivity of >100 Ωm before irrigations 1, 2, and 3. With the typical bulk resistivity range in clays ranging from 2 to 100 Ωm (Sharma, 1997), this threshold was chosen to localise areas of the soil that are likely to be affected by soil cracking. Figures 6.8d-f shows the areas of the inverted model that went through a resistivity change of more than 100 Ωm during irrigations 1, 2, and 3. As such resistivity change exceeds the typical resistivity range for clays it is assumed that these areas were affected by crack closure.

Both methods used to determine crack affected areas from the ERT data give

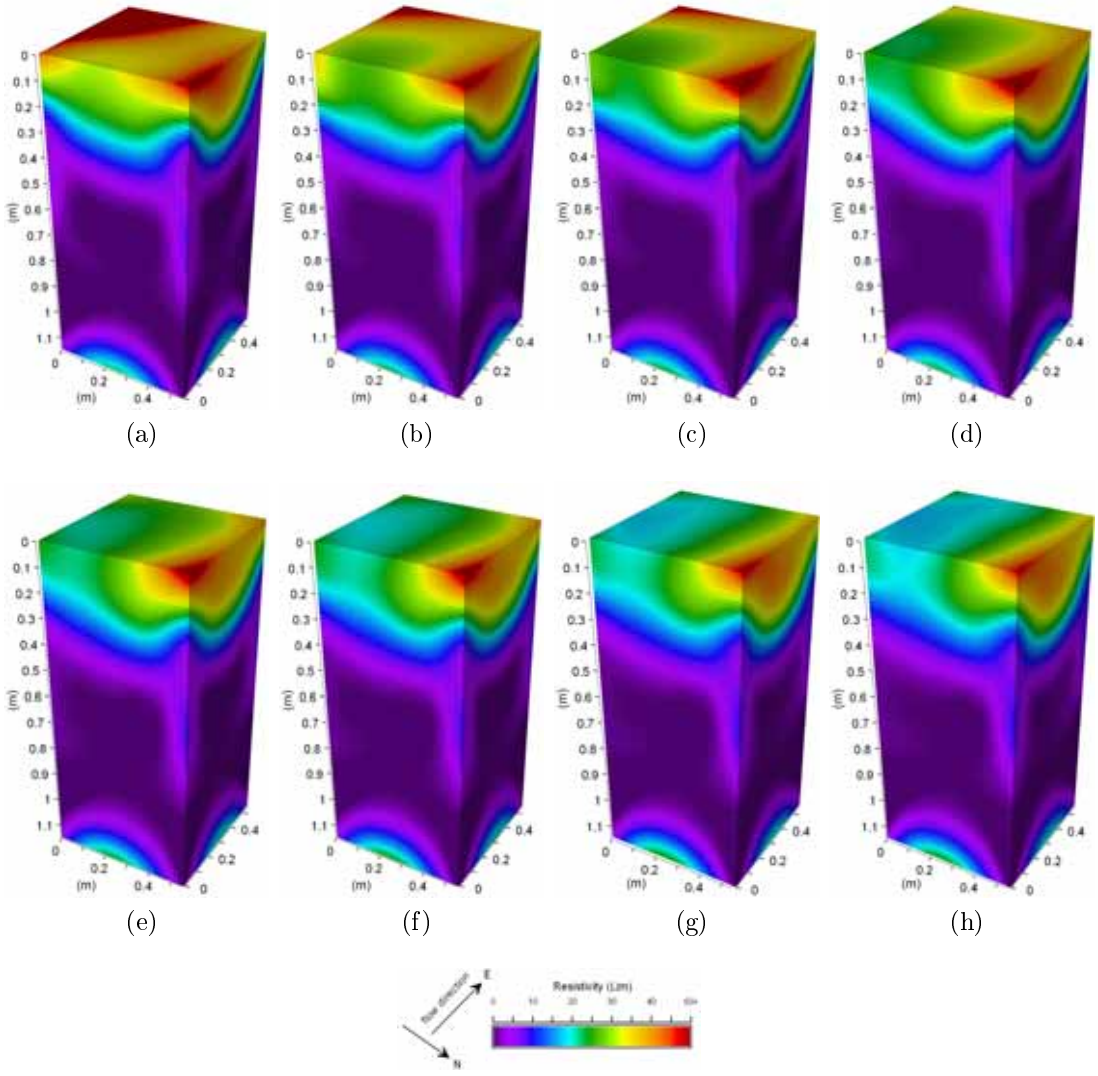

Figure 6.5: 30 minute steps of a time lapse series throughout irrigation 1 taken with the short protocol. Image a shows the resistivity distribution in the sampling interval before irrigation water arrived at the probes (Note: The irrigated furrow is at the left of the image).

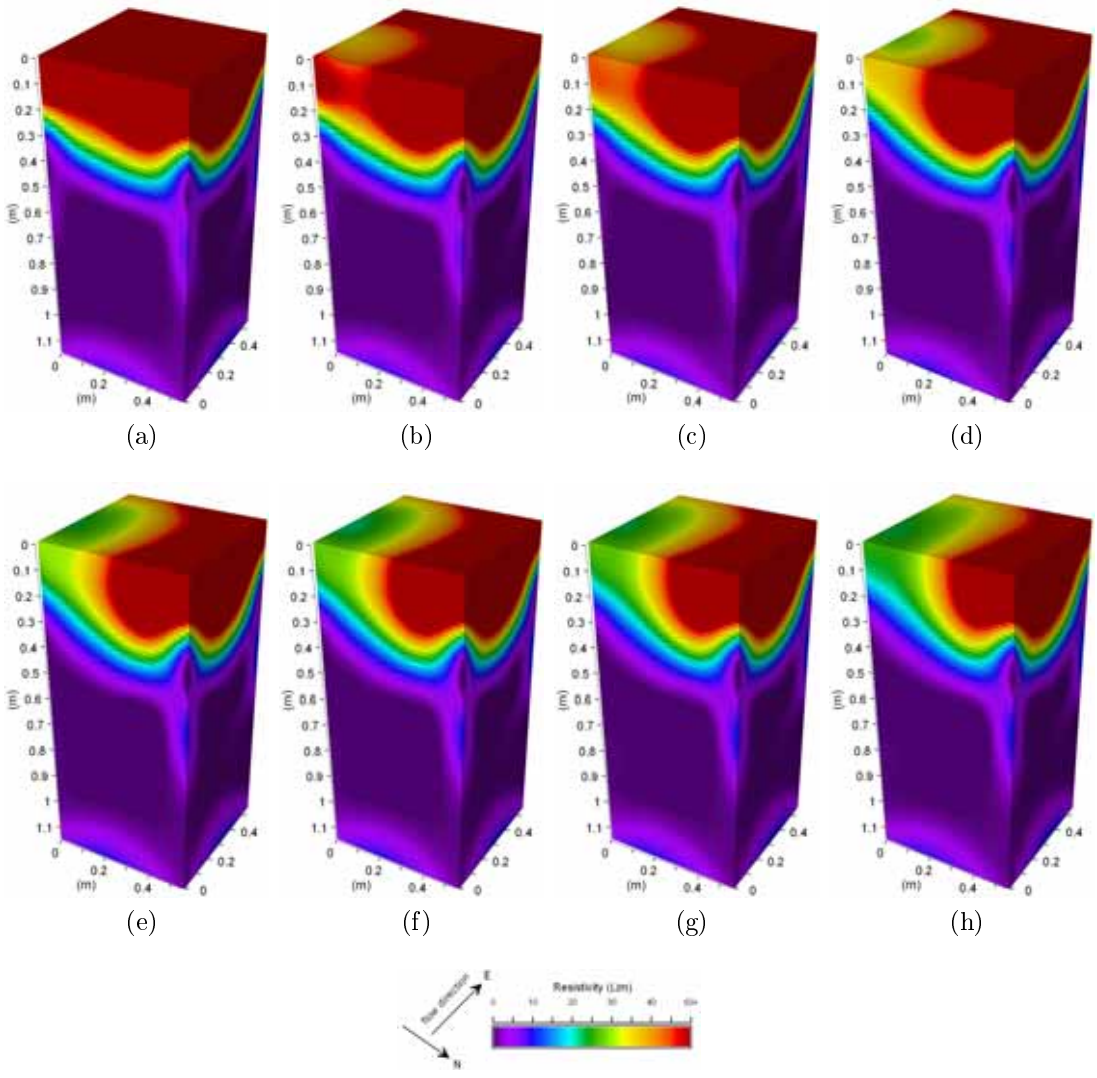

Figure 6.6: 30 minute steps of a time lapse series throughout irrigation 2 taken with the short protocol. Image a shows the resistivity distribution in the sampling interval before irrigation water arrived at the probes (Note: The irrigated furrow is at the left of the image).

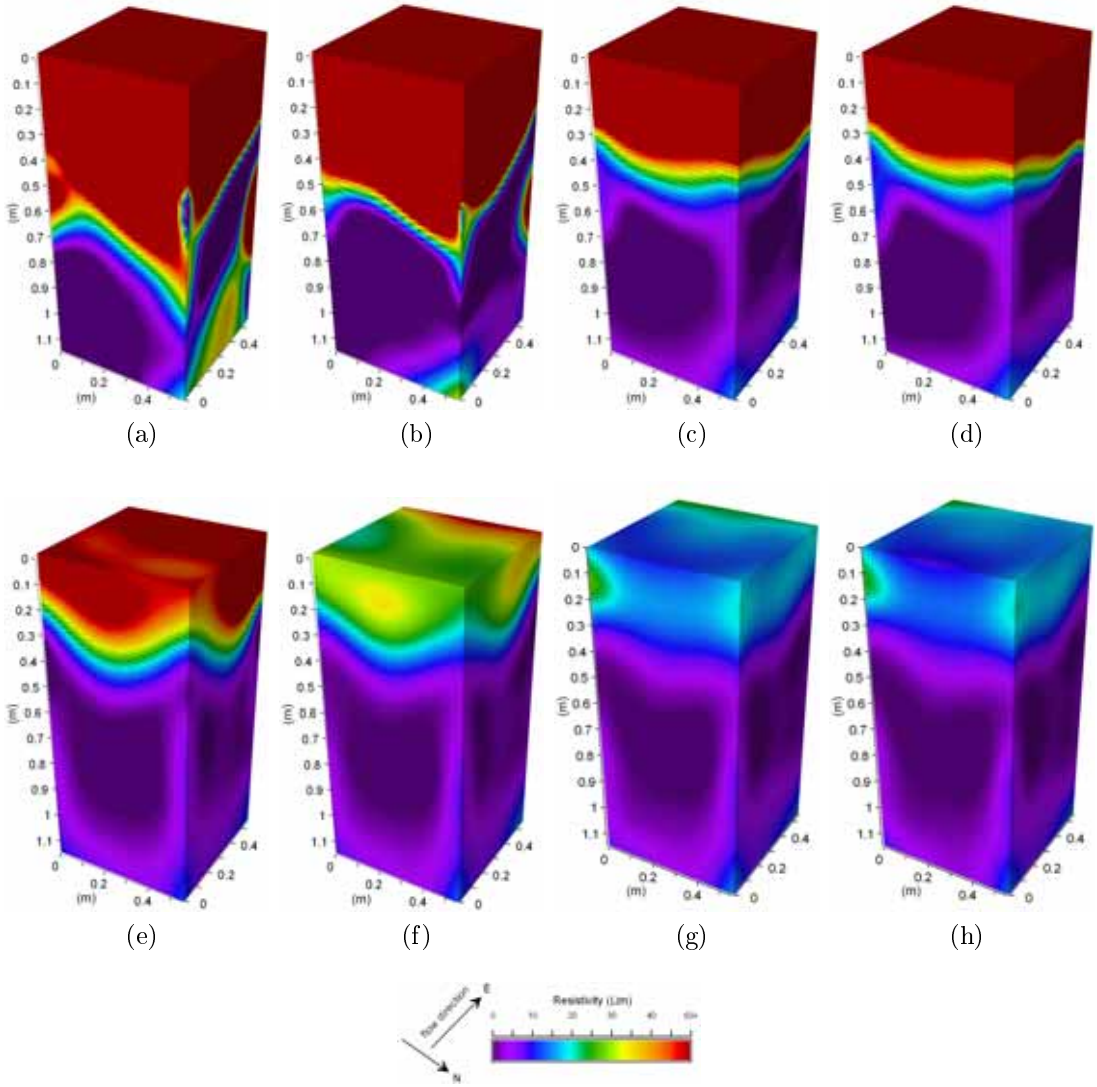

Figure 6.7: 20 minute steps of a time lapse series throughout irrigation 3 taken with the short protocol. Image a shows the resistivity distribution before water was pumped into the confined area around the probes (Note: The irrigated furrow is at the left of the image).

similar results, except that the area of crack closure is consistently smaller than the crack affected area before the irrigation events. This difference can be explained by the choice of resistivity threshold, as a resistivity change of >100 Ωm is less likely to occur than an absolute resistivity of >100 Ωm. This dependence of the crack affected area on the chosen threshold, highlights that the inverted resistivity does not provide a measure of true crack dimensions but rather a relative indicator of the extent of cracking at different soil stages.

The crack affected area (Figure 6.8) increases in depth and lateral extent from irrigation 1 to 3, which is consistent with the increasing AI deviation in Figure 6.4f. In Sections 3.1 and 3.2, it was shown that cracks that do not intersect the electrode square have a reduced impact on the AI. Considering the small lateral extent of the crack affected area before irrigation 1 it is not surprising that the AI deviation before irrigation 1 was only minor (Figure 6.4f). The lateral extent of the crack affected area is larger for irrigation 2, which is reflected by an increased AI deviation (Figures 6.8 and 6.4f). Both the crack affected area and the AI deviation in the anisotropy profile are largest for irrigation 3, where the crack affected area forms horizontally isolated deep reaching zones (Figures 6.8c and f), which are not present for irrigations 1 and 2. As deeper cracks are wider spaced (Groisman and Kaplan, 1994; Colina and Roux, 2000a), the inversion routine is capable of separating them in the inverted resistivity model, whereas the shallower closer spaced cracks appear as a continuous entity. The vertically and horizontally isolated cracking zone at ∼1 m in Figures 6.8c and f, is located at the border of the modelling area and is thus most likely due to a crack that diverts from the vertical and enters the model area at this particular depth.

The anisotropy profile before irrigation 3 (Figure 6.4f) is significantly more complex than the AI profiles in Chapter 3. Multiple cracks of altering depth, length, and orientation, as in a cracked soil profile, result in increasingly complex anisotropy profiles with multiple local minima and maxima. To identify crack scenarios that cause local maxima and minima of the AIP, numerical simulations were carried out using the same model dimensions as described in Section 3.1. The following crack

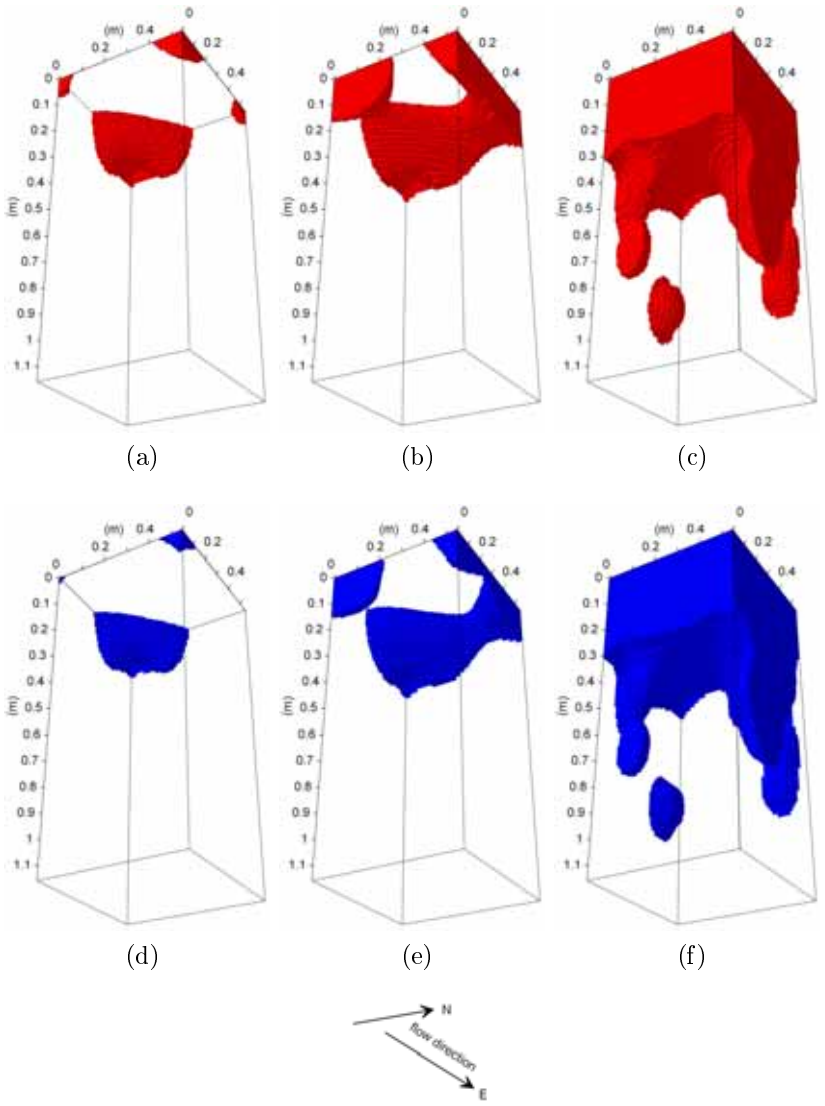

Figure 6.8: Crack affected image areas (view: diagonally upwards); a-c: Areas with a bulk resistivity of 100 Ωm before irrigations 1,2, and 3 respectively; d-f: Areas where a bulk resistivity change of 100 Ωm occurred during irrigations 1,2, and 3 respectively (Note: The lower small isolated hemisphere is protruding from the x,z plane).

scenarios were identified to cause local minima and maxima: bridging of cracks at certain depth, cracks entering the modelling area at depth, individual cracks terminating, and alteration of a cracks orientation at depth. Depending on the other cracks in the profile, each of these four identified crack scenarios has the potential to create either a local maximum or a local minimum.

While the collected data did not allow the determination of the exact cause of each of the turning points in the *AIP*, two points of significance could be identified. The first point is the depth where the *AI* deviation ends and the *AI* value returns to values that indicate homogeneous conditions, such as the *AI* of the moist soil in Figure 6.4f. It is reasonable to assume that this point lies within crack free soil, so that it hereafter will be referred to as the maximum cracking depth. Before irrigations 1 and 2 this maximum cracking depth is 555 mm and before irrigation 3 it is 1155 mm (Figure 6.4f). The second significant point in an anisotropy profile is the last pronounced maximum of the *AI* deviation. As an inhomogeneity needs to be present at a particular profile depth to cause a local maximum, we know that the last maximum lies within cracked soil. It will hereafter be referred to as the minimum cracking depth. In the anisotropy profile collected before irrigation 3, the minimum cracking depth is 780 mm (Figure 6.4f). Before irrigation 1 and 2 the minimum cracking depth cannot clearly be identified as the *AI* deviation before these two irrigations is not very pronounced. The true cracking depth lies somewhere between the minimum and maximum cracking depth, which for irrigation 3 is between 780 and 1155 mm. This complies with the maximum depth of the crack affected area in Figures 6.8c and f of $\sim$1050 mm.

Even though both the collection of anisotropy profiles and the collection of 3D ERT images utilise the same instrumentation, their results can be seen as independent from each other, as inverted 3D resistivities measured with the dipole-dipole array are not related to the directional dependence of current flow, which is expressed by the anisotropy profiles. The complementary nature of these independent methods strengthens the interpretation. However, as the inverted resistivity should not be

taken as a measure of the true crack dimensions, comparison of the AI results with an additional measure of cracking depth would further support the interpretation. Figure 6.9a shows the temperature changes that were recorded during irrigation 3. A sudden temperature change at 300, 450, and 850 mm depth, which occurred at the time the water application rate was increased to 1200 L/h, indicates the arrival of irrigation water at these depths. A rise in temperature is also detected at 1200 mm, however it is significantly less pronounced than the rise at 300, 450, and 850 mm. This indicates that if water arrived at 1200 mm, it was significantly less than the amount of water that arrived at the other measuring depths. With the lack in temperature gradient between the upper soil and the 33 °C warm irrigation water, the temperature response due to water arrival is less pronounced at the top of the profile. The fast arrival of irrigation water at 850 mm indicates preferential flow and thus a cracking depth of >850 mm, which confirms the range of cracking depth obtained from the anisotropy profile.

Figures 6.9b and c, show that no sudden temperature change occurred during the application of the freshly pumped ground water, which had a temperature of ∼21°C when it arrived at the resistivity probes. A damping of the temperature curve at 150 mm occurred during irrigation 2, which could be taken as an indication of water infiltration. This depth corresponds with the infiltration depth indicated in the time lapse image series in Figure 6.6 and also with the depth of the crack affected area for irrigation 2 as indicated by Figures 6.8b and e. The lack of a temperature response during irrigation 1 (Figure 6.9b) could be attributed to the reduced infiltration depth indicated in Figure 6.5 and Figures 6.8a and d.

In this experiment, an additional factor that could have caused inhomogeneity are the growing roots of the sorghum plants. This additional inhomogeneity, if present, should be reflected in changes of the AI values in the anisotropy profiles that were collected in the moist, non cracked soil, 24 hours after each of the three irrigation events. However, the anisotropy profile returned to a very similar profile (within a 5 % tolerance) after all three irrigation events. As water filled soft roots have resistivities

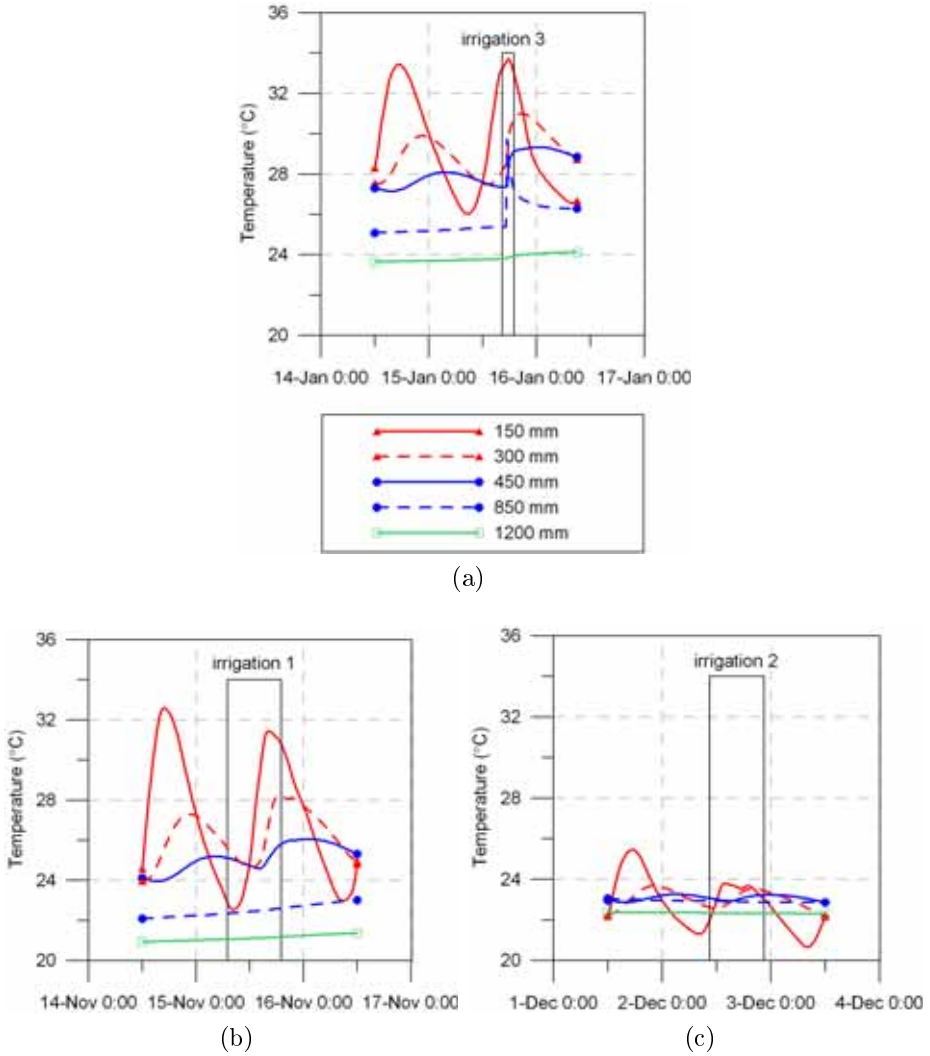

Figure 6.9: Temperature changes in the soil profile during the three irrigation events; a: Irrigation 3; b: Irrigation 1; c: Irrigation 2.

of a similar range compared to clay soils (Sharma, 1997; Hagrey, 2007), the negligible influence of the sorghum roots is not surprising. It is therefore concluded that cracks that open and close were the dominant cause of AI changes in the profile.

6.3 Conclusions

This chapter demonstrates that anisotropy profiles are an excellent tool for determining cracking depth not only in the laboratory, but also in the complex environment of an agricultural field. In addition to the collection of anisotropy profiles, the extent of soil cracking was independently assessed by 3D electrical resistivity tomography as well as by measuring changes in soil temperature that are caused by water movement

through the cracks. Results of the three different methods were consistent with each other, which increases the confidence in each of the applied methods. Furthermore, it was shown that a well developed anisotropy profile allows the detection of a cracking depth range, which extends the use of anisotropy profiles from a qualitative to a quantitative crack analysis. As changes in the sorghum root system throughout the growing season had only a minor influence on the index it can be concluded that also in a field setting, it is the soil cracks that cause the changes in anisotropy profiles.

Chapter 7

Field Measurement in Cotton

A second set of field measurements was carried out in the growing season 2008/09 in a cotton field at the Australian Cotton Research Institute (ACRI), 20 km north west of Narrabri, New South Wales, Australia. These measurements provide a second data set collected on a different soil and under a different crop with different irrigation needs to verify the results obtained in Chapter 6. At this case study site, additional soil moisture and drainage data were recorded with neutron probes and a lysimeter, allowing comparison with alternative methods. Furthermore the soil in the experimental plot had been well described by Ringrose-Voase and Nadelko (2006), which gave increased insight during the interpretation of the resistivity data.

7.1 Methods

The experimental plot at the ACRI site (Figure 7.1) was under a cotton-wheat rotation. Minimum tillage was used with stubble retention and permanent beds. From head to tail ditch, the plot is ∼200 m long, with furrows running approximately from east to west. Soil characterisation was carried out in a 2 m deep pit that was dug by backhoe about 20 m west of the lysimeter location shown in Figure 7.1 (Ringrose-Voase and Nadelko, 2006). The upper 1.2 m of the profile were found to have clay, silt and sand fractions of 60, 14, and 25 % respectively. Below 1.2 m the clay fraction decreased to 50 %, with the silt and sand fractions increasing to 20 and 30 % respec-

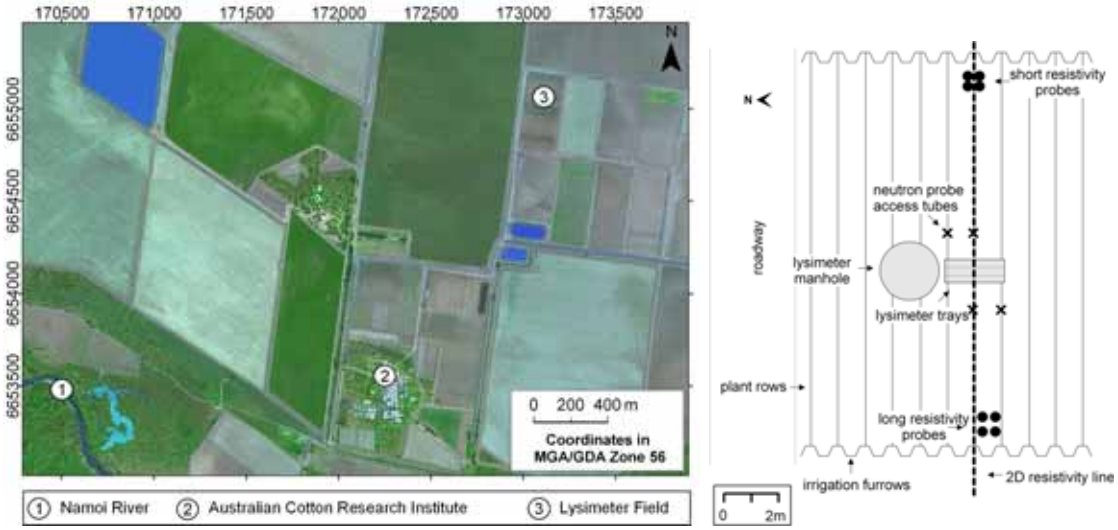

(a) (b)

Figure 7.1: Fieldsite at the Australian Cotton Research Institute near Narrabri, NSW, Australia; a: Site overview; b: Setup in the lysimeter field.

tively. The cation exchange capacity decreased from 334 mmol/kg at the top of the profile to 245 mmol/kg at 1.85 m. Located at 0.3 to 0.7 m depth was a compacted layer with a hydraulic conductivity of 0.3-0.6 mm/h, which was two magnitudes lower than that of the subsoil. The presence of this layer is likely to control the water movement to greater depth.

The ACRI site is equipped with a variable tension lysimeter, which is located south of the roadway (Figure 7.1b), halfway between the head and the tail ditch. Ringrose-Voase and Nadelko (2006) describe the lysimeters setup in detail. Variable tension lysimeters are designed to mimic the hydraulic gradient of the soil and thus not to interfere with the drainage rate. The system regularly measures the soil water potential at 2 m (measured from the low part of the furrows) and applies a vacuum equal to this potential to its six collection trays. The six collection trays are located at 2 m depth and cover a total area of 1.8 x 0.9 m .

Four neutron probe access tubes are located in the vicinity of the collection trays. The access tubes allow measurements of the soil's water content (SWC) to a depth of 2.7 m. The conversion from the neutron probe readings to volumetric SWC was based on the following calibration relationship (*A. Nadelko*, personal communication):

$$SWC_v = e^{(CR-c_1)/m_1}, \tag{7.1}$$

where SWC_v is the volumetric soil water content, and CR the count ratio, that is the ratio of the number of neutron probe counts in the soil and the number of counts in water. The two calibration parameters c_1 and m_1 vary with soil depth, below 0.2 m they are 0.3388 and 1.0058, respectively, for depth between 0.2 and 0.5 m they are 0.2826 and 0.9744, and at depths greater than 0.5 m they are 0.1816 and 0.8614. The lysimeter and neutron probe data were collected and made available for this study by ACRI personnel.

In November 2008 the short and the long sets of resistivity strings (refer to Section 5.2 for a description of the strings) were installed at the site. To allow the probes to remain in place during machine operation they were installed deeper than at the Maules Creek site described in Chapter 6. The first electrode on each of the four strings of the short set was located at 0.35 m, while the first electrodes on the long strings were located at 0.45 m. As in Chapters 3 and 6, the four strings were installed in the corners of a horizontal square. The square had a side length of 550 mm for the short set and of 730 mm for the long set, which resulted in identical ratios between the probe separation and length. Both measurement squares were arranged with their sides parallel and orthogonal to the plant rows. As indicated in Figure 7.1b, the square formed by the short probes was centred over a plant row, while the long probes were centred over an irrigation furrow. The installation of the probes was carried out as described for the Maules Creek site (Section 5.3 on page 51).

Due to a series of events that hampered plant growth, the cotton in the experimental plot was replanted three times in 2008. Initial planting took place on the 09/10/2008. As large proportions of the seeds did not germinate, the cotton was replanted on the 31/10/2008. Installation of the resistivity strings took place on the 10 and 11th of November, just after plant germination of the second planting. However, large proportions of this second planting did not survive either. Hence, a third planting was carried out on the 24/11/2008. The third planting occurred only in the

10 rows adjacent to the roadway at the north. These rows contained the measuring instruments and had the most severe plant damage. Only ∼60 % of these plants survived and the area around the two resistivity installations remained bare. Therefore manual replanting of cotton from the third planting was carried out in the probe area on the 10/12/2008.

The cotton was irrigated six times during the growing season. Due to good rains in the early parts of the season the first irrigation was not carried out until the 22/12/2008. The last irrigation took place on the 19/03/2009 before the cotton was picked on the 12/06/2009. Resistivity measurements were carried out during four of the irrigations, during irrigation 1, 2, 3, and 5, which took place during the day on the 22/12/2008, 12/01/2009, 22/01/2009, and on the 6/03/2009. These four events are in the following referred to as the monitored irrigation events. The water used for irrigation was a mixture of Namoi river water and ground water. The varying proportions of the two water types resulted in the following ECs of the applied water: 27, 39, 47, 37, 39, 38 mS/m for irrigations 1 to 6, respectively.

During the monitored events, the ABEM terrameter was connected to one probe set at a time and the short and long ERT protocol as well as the square protocol were run before and after the irrigation. In addition to this, the square protocol was run in time lapse mode, set to record in 5 minute intervals during the irrigation events. During irrigations 1 and 2, the square protocol was run at the long probes, and during irrigation 5, it was run at the short probes. As it started to rain at the onset of irrigation 3, and as vehicle access to the plot was not possible during wet conditions, no time lapse measurements were carried out during irrigation 3. Furthermore the pre-irrigation measurements with the short and the long protocol at the long set of probes were not completed before the field had to be left. One day after the irrigation, vehicle access was again possible and post-irrigation measurements were carried out.

A 2D resistivity image line was taken before and after irrigation 5. Collection of the 2D line took ∼90 minutes and was started at 12:30 and 13:30 on the days before and after the irrigation, respectively. The 2D image was collected with a Wenner

alpha array with a minimum electrode spacing of 1.25 m. The electrodes were located on the crest of the 7th plant row from the north, which cut through the centre of the short set of electrode strings (Figure 7.1b). While the electrode cables were removed during the irrigation, the electrodes themselves were left in place.

The collected 3D ρ_a data were inverted and plotted as described in Section 6.1.2. Inversion of the 2D resistivity image was carried out with the default setting of *Res2Dinv* (Loke, 2009a) using the finest model mesh for forward modelling and the true Gauss Newton optimisation method. Neither the 2D nor the 3D resistivity data were temperature corrected. Figure 6.3 on page 64 shows that diurnal temperature variations at the insertion depth of the electrode strings were only minor, as were the variations at the measurement depth of the 2D image. Even for the smallest electrode spacing of the 2D measurements half of the measurement signal came from a depth of $>$ 0.625 m. Furthermore, both 2D image lines were collected at similar times during the day (12:30 h and 13:30 h) on days which had similar air temperature ranges (11-33°C and 11-29°C).

7.2 Results and Discussion

The average pre- and post-irrigation soil water content (SWC), derived from the neutron probe readings, is shown in Figure 7.2, together with the range of SWC from the lower limit of plant abstraction (LL) to the drained upper limit (DUL). The LL and DUL are based on the minimum and maximum soil water content at the side as measured during five years of neutron probe readings (*A. Ringrose-Voase*, personal communication). Throughout the four monitored irrigation events, the pre-irrigation SWC decreases from irrigation 1 to irrigation 5. The largest change in SWC during all monitored irrigations is detected at the upper three measuring depth of 0.1,0.3, and 0.5 m. A further, moderate change in SWC is detected at 0.8 m. The SWC change at 0.8 m is especially pronounced during irrigation 5. Below 0.8 m no significant change in SWC during the irrigations was detected.

The post-irrigation SWC was measured 28, 26, 28, and 25 h after the onset of

the respective irrigations. Considering the saturated hydraulic conductivities in the upper soil profile, which are 5.9 mm/h in the plough layer and decrease to 0.3 to 0.6 mm/h for the compacted layer at 0.3 to 0.6 m depth, these infiltration depths could not have occurred based on piston flow alone. Instead, the infiltrating water must have travelled along preferential flow paths for at least part of the way.

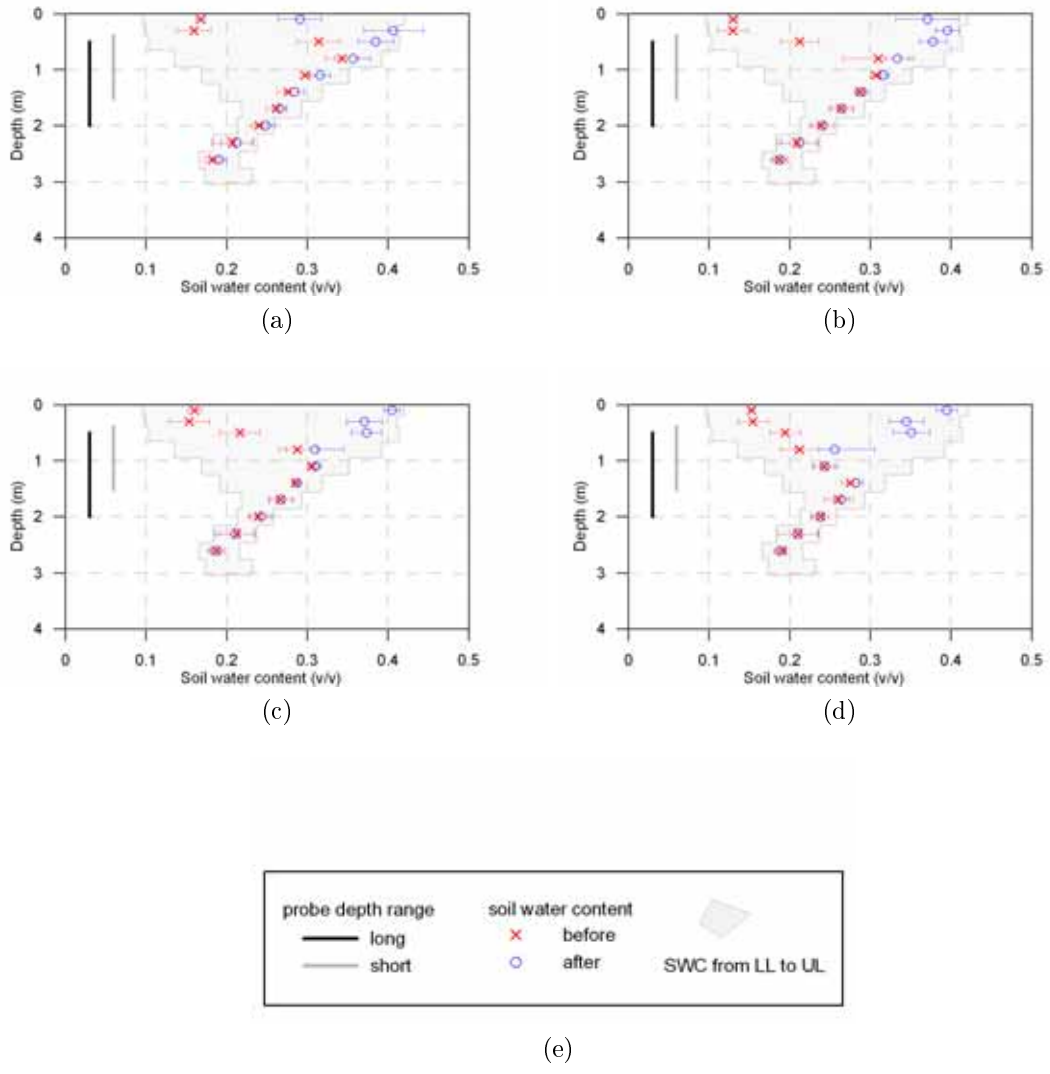

Figure 7.2: Soil water content (SWC) measured with the neutron probe before and after the four monitored irrigations; a: Irrigation 1; b: Irrigation 2; c: Irrigation 3; d: Irrigation 5 (Also shown is the measurement depth range of the short and long resistivity probe set as well as the range of SWC from the lower limit of plant abstraction (LL) to the upper drained limit(UL)).

Due to the different plant cover and growing stages that are present in the plot, it is necessary to determine whether the SWC measured with the neutron probes is representative of the SWC at the location of the long and short resistivity probes.

Investigating the 2D resistivity images that were taken before and after irrigation 5 (Figures 7.3 and 7.4) will allow this comparison. The pre-irrigation image shows that the bulk resistivity distribution is directly influenced by the extent of plant growth in the three rows closest to the image line. Full plant cover and hence full plant water abstraction is reflected in highly resistive anomalies in the root zone to a depth of 0.5 to 1.25 m. In areas where no cotton plants could be established, the soil profile is not being dried out by the roots and the highly resistive anomalies do not occur. In addition to the variation in plant cover along the 2D row, the plants were also at 3 different growing stages, which is a likely explanation for the differences in the extent of drying found within areas of full plant cover.

The observed near surface resistivity anomalies are directly related to plant cover and hence plant water uptake. Furthermore, the reduction in size and number of resistive anomalies that occurred between the pre- and the post-irrigation image is directly related to a water application. It is therefore reasonable to assume that the near surface resistivity anomalies and their changes in time are mainly due to soil water changes.

In addition to the near surface resistive anomalies, a second deeper reaching anomaly is found in both the pre- and the post-irrigation images. This anomaly is located $\sim$33 m along the image line at the height of the lysimeter trays. The lysimeter trays are made from metal and hence a conductive anomaly could be expected. However, $<$ 2 m to the north of the image line begins the concrete access shaft for the lysimeter (3 m deep, 2 m diameter). This high resistive structure is overshadowing the conductive lysimeter trays, resulting in the observed resistive anomaly.

As shown in Figure 7.3, the short and the long resistivity probes, as well as the neutron probe access tubes and the lysimeter trays are located under full plant cover in a zone of the 2D image that shows plant induced drying at the top of the profile. It is hence assumed that the SWC measured with the neutron probes is a reasonable representation of the SWC at the resistivity installations. However, the neutron probe measurements might underestimate the true range of soil moisture variation found

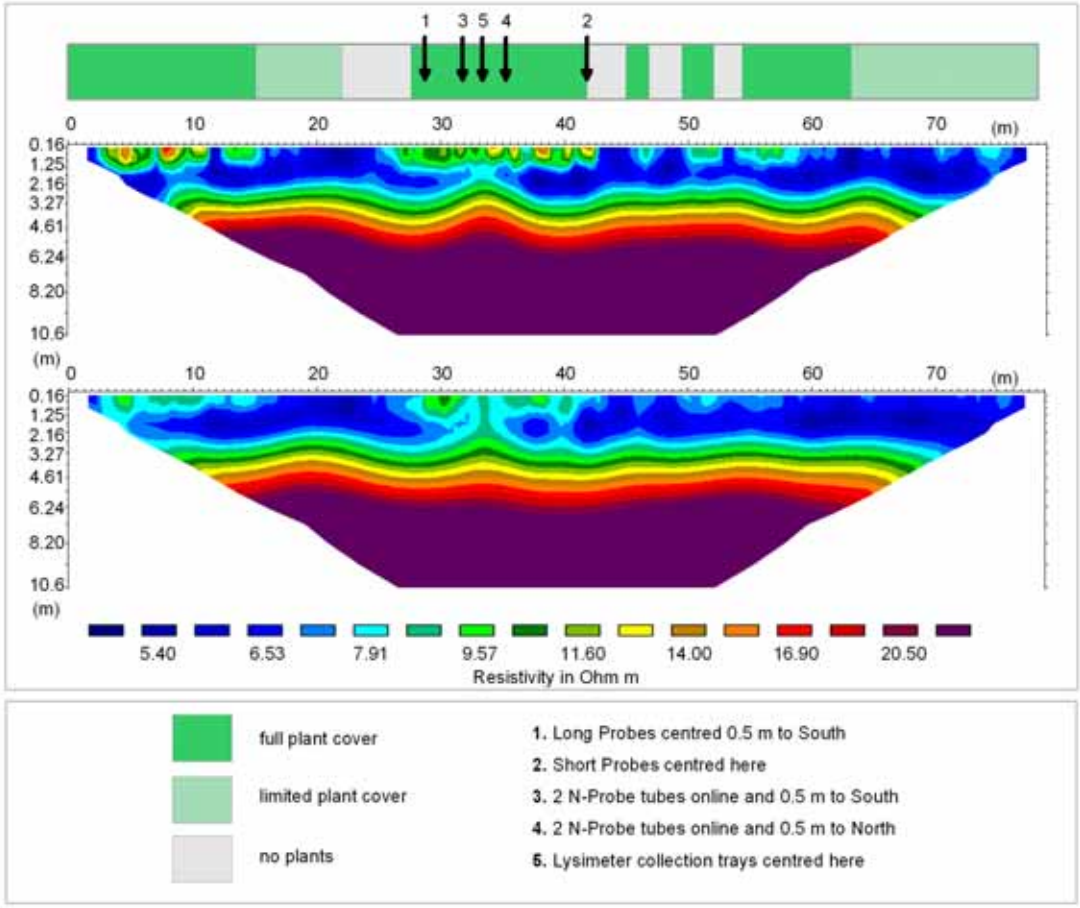

Figure 7.3: 2D image lines taken before and after irrigation 5 as well as the degree of plant cover in the three rows closest to the image line.

within areas under full plant cover, which is highlighted in the 2D image.

The smooth resistivity changes resulting from Occam's inversion (deGroot Hedlin and Constable, 1990) do not allow the detection of the exact drying depth in the pre-irrigation 2D image. Furthermore, the violation of the 2D assumption might cause a deformation of the inverted resistivity anomalies. Underlying the 2D inversion is the assumption that variations in the third dimension, in this case in north south direction, are negligible. With the plant cover varying in all directions, this assumption is violated for the near surface resistivity variations. Bentley and Gharibi (2004) and Batlle-Aguilar et al. (2009) highlighted that such a violation of the 2D assumption can result in deformation of resistivity anomalies, resulting in over or under estimation of their depth. Another factor that limits the exact detection of the drying depth in the 2D image is the electrode spacing of 1.25 m, which is relatively large compared to the

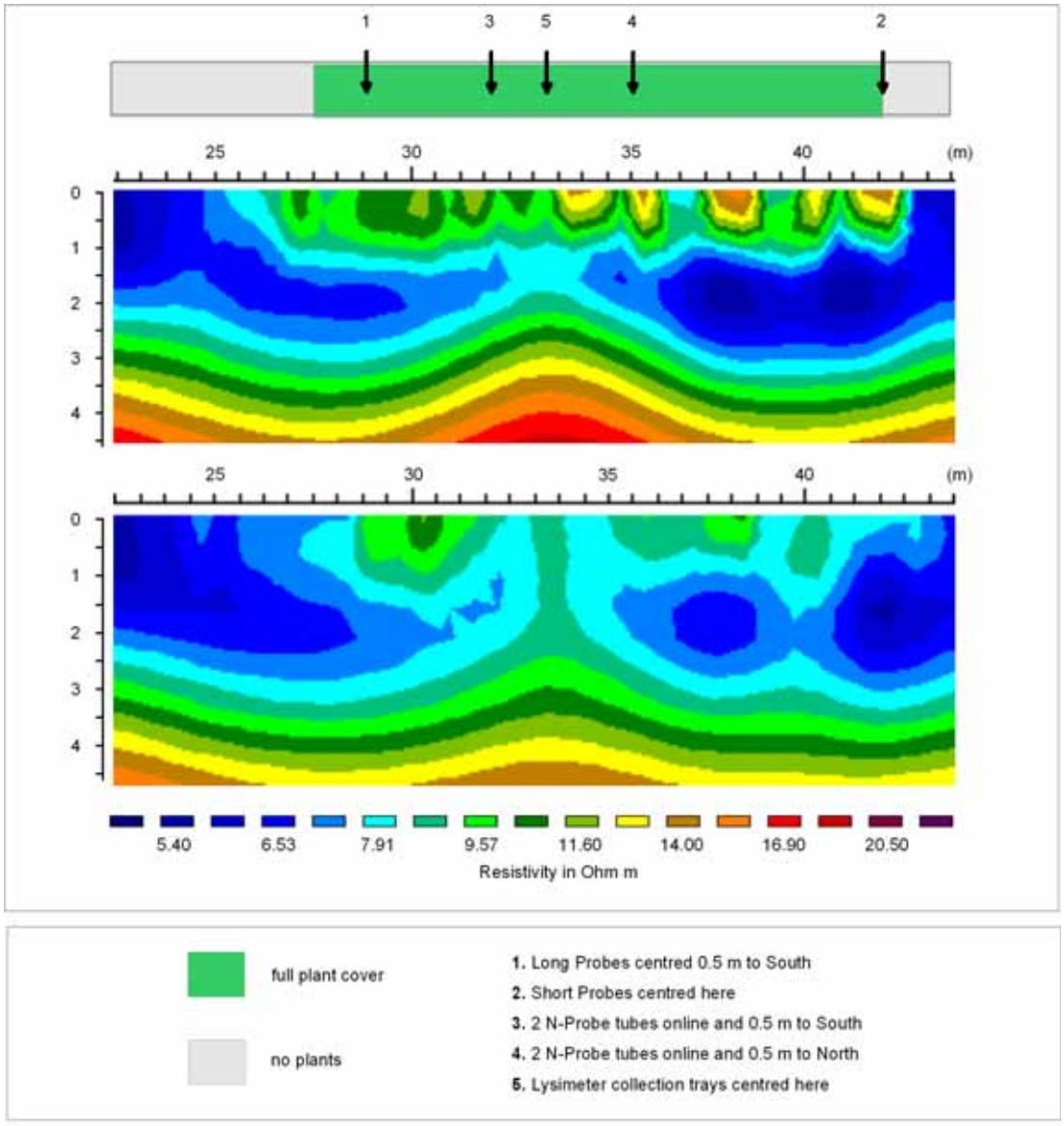

Figure 7.4: Expanded view of the 2D resistivity distribution in Figure 7.3 in the area around the measurement probes and the lysimeter.

drying depth.

The 3D ERT results are not limited by the 2D assumption, nor by a reduced image resolution due to the electrode spacing, so that the drying depth obtained in these images can safely be compared to the neutron probe readings. While the deeper installation of the resistivity probes allowed the probes to remain in place during machine operation, it did not allow the monitoring of the upper 0.35 and 0.45 m of the soil profile, where the majority of soil moisture changes occurred (Figure 7.2). Hence, no drying was visible in the pre-irrigation 3D ERT images taken before

irrigations 1 and 2. Even before irrigation 3, only minor drying is indicated (Figure 7.5a). This lack of drying in the 3D ERT images is contrary to the neutron probe readings, which detect soil drying to a depth of 0.5 m before irrigations 2 and 3. This difference could be accounted to the different growing stages of the plants over the neutron probes and the plants over the resistivity probes. At this state in the growing season, the water uptake of the re-grown plants around the resistivity probes might not yet have caught up with the water uptake of the plants around the neutron probes.

Another possible reason for the inability of the 3D ERT image to detect the drying front is the lower image sensitivity to dry and resistive zones. Figure 5.4 on page 53, shows that the sensitivity in a homogeneous half space is reduced at the upper and lower end of the measurement plane. This reduction is directly related to the lower data density in these regions, due to a lack of overlap of the electrode arrangements at the end of the probes and is typical for cross borehole measurements (Ramirez et al., 1995). This reduced sensitivity is also reflected in the increase in VOI indices towards the end of the probes as shown in Figure 5.7 on page 58. In addition, current predominantly flows in conductive zones, resulting in sensitivity patterns with lower sensitivities over resistive regions of the subsurface (Stummer et al., 2004). During soil drying, the sensitivity at the top of the profile is hence further reduced compared to the sensitivity over the homogeneous half space shown in Figure 5.4.

Before irrigation 5, the drying depth derived from the neutron probe readings is increased to 1.1 m and is clearly shown in the ERT images for both probes (Figures 7.5c and 7.6b). Taking the centre of the smooth changing zone between the high resistive red zone and the low resistive blue zone in the ERT images as the drying depth, gives a drying depth that varies between 0.60 and 0.95 m for the short ERT image and a drying depth that varies between 0.70 and 1.15 m for the long image. The inaccuracies resulting from the smooth resistivity change in the ERT images are negligible compared to the variation in drying depth within the images themselves. Differences in drying depth between the neutron probe readings (1.1 m) and the ERT images (0.60 to 0.95 m and 0.70 to 1.15 m) can be attributed to the spatial

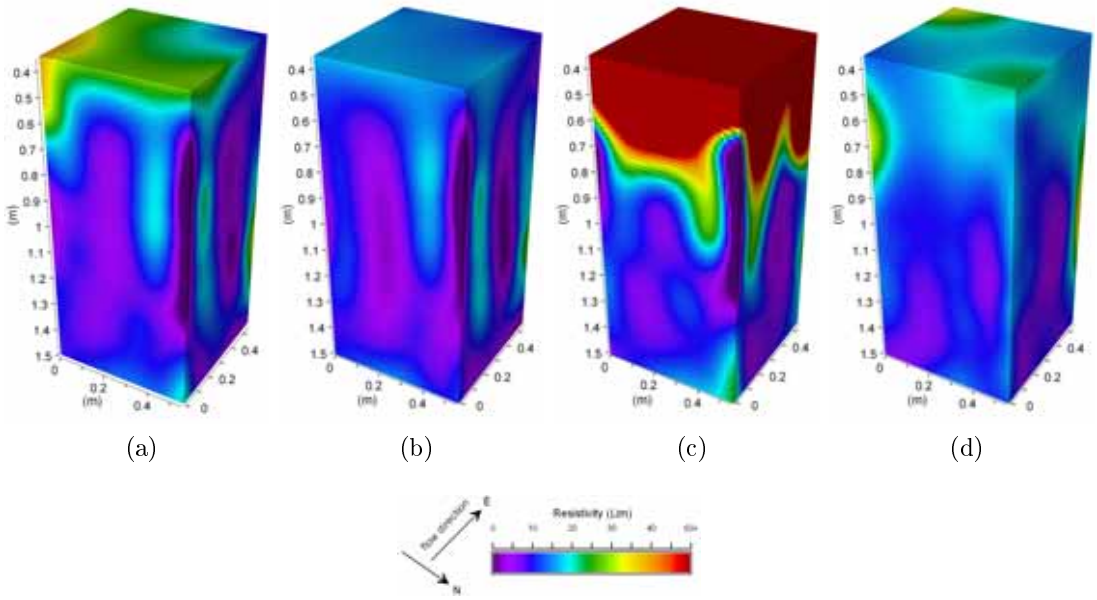

(a) (b) (c) (d)

(e)

Figure 7.5: 3D resistivity images collected with the short probes, before (a) and after (b) irrigations 3 and before (c) and after (d) 5.

variation in soil moisture that are highlighted in both the 2D and the 3D resistivity images. Comparing the drying depth highlights the limited ability of the neutron probe readings to capture the spatial variation in soil moisture content. This limitation can be attributed to the large sphere of influence of neutron probes, which varies from ∼150 to ∼300 mm in diameter from wet to dry soil conditions (Bell, 1976) and causes a much coarser resolution than that of the 3D images. In addition, the limited number of access tubes did not allow the capture of larger scale variations that could be seen in the 2D image. Spatial soil moisture variations are especially pronounced in cracking soils, where the increased evaporation along the crack walls (Johnston and Hill, 1944; Tuong et al., 1996) and the preferential soil wetting along the cracks (Topp and Davis, 1981; Wopereis et al., 1994; Yasuda et al., 2001) enhance the spatial variation of soil moisture, which is due to varying soil water uptake by the plant roots (Hupet and Vanclooster, 2005). Soil moisture measurements that are capable of capturing this spatial variability are hence especially favourable in cracking soils.

The anisotropy profiles collected with the long and short set of electrode strings are shown in Figures 7.7 and 7.8. As both probe sets are installed deeper in the soil

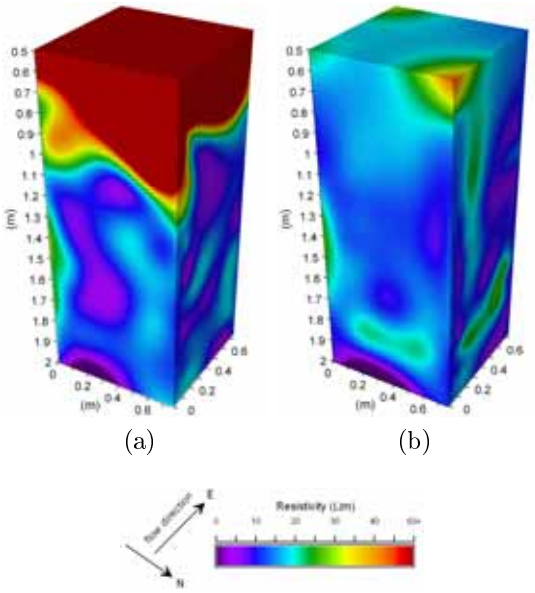

(a) (b)

(c)

Figure 7.6: 3D resistivity images collected with the long probes, before and after irrigation 5 (Note: ERT Measurements before irrigation 3 could not be completed, refer to Section 7.1).

profile than the probes at the Maules Creek site (Chapter 6), the changes in anisotropy at the top of the profile are not captured. The anisotropy profiles for both sets of probes did not show any change during irrigations 1 and 2. During irrigation 3 the long anisotropy profile, which started at 0.45 m depth, did not show any change either (Figure 7.7a). Whereas the short anisotropy profile, which started at a depth of 0.35 m, showed a moderate AI change during irrigation 3 (Figure 7.8a). Due to the dryer soil conditions both profiles recorded changes in the anisotropy during irrigation 5 (Figures 7.7b and 7.8b).

Collection of anisotropy profiles in time lapse mode for the short probes allows a detailed investigation of the AI changes during irrigation 5. The AI change occurred between 9:05 am and 9:15 am, while the AI before and after this period remained stable (Figure 7.8b). Comparing the timing of the AI changes with the arrival of the irrigation water at the probes gives information about the water flow in the cracks. Figure 7.9a shows the irrigation furrow at the north of the short probes before irrigation 5. The crack running orthogonal to the furrows in the centre of the image is intersecting the AI measurement area. Water arrived at this crack at 9:12 am and

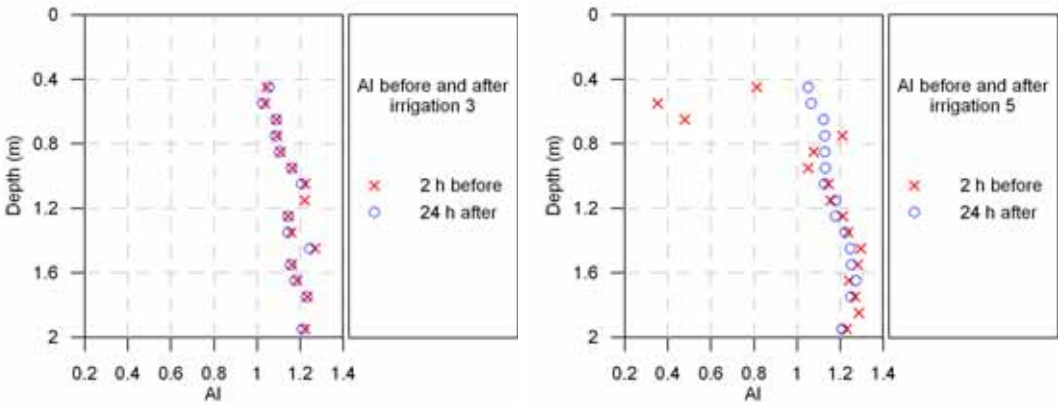

(a) (b)

Figure 7.7: Anisotropy profiles collected at the long probes, before and after irrigations 3 as well as in 5 min intervals before, during and after water arrival at the short probes during irrigation 5.

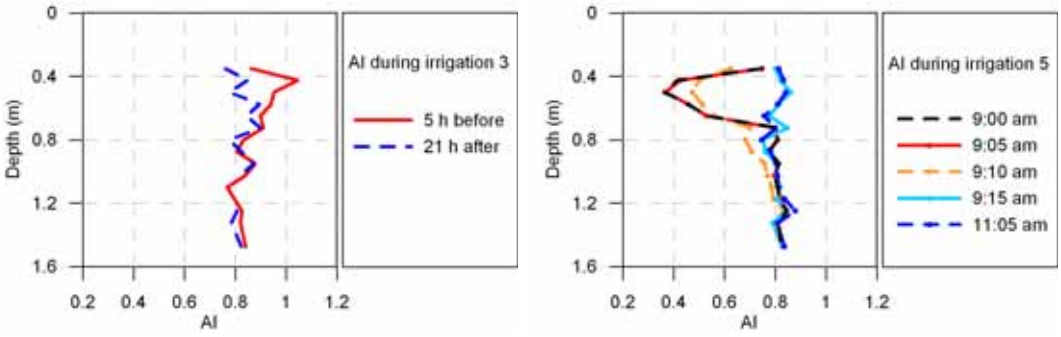

(a) (b)

Figure 7.8: Anisotropy profiles collected at the short probes, before and after irrigations 3 and 5.

kept pouring into the crack for ∼15 seconds before it continued to flow down the furrow. The first change in AI was detected before the surface water arrived at the probes at 9:10 am. This indicates that water flowing through cracks in the subsurface must have reached the probes before the arrival of the surface water. It was observed that water flowing in the cracks was preceding the surface water, which is consistent with the observations of Tuong et al. (1996). Tuong et al. (1996) noted water moving in the cracks of a flooded rice paddy was up to 7 m ahead of the surface water. Field observations during irrigation 5 indicated that the crack water exceeded the surface water flow by at least 2 m. Two images of subsurface flow in the cracks are shown in

(a) (b) (c)

Figure 7.9: Soil cracks before and during irrigation 5; a: Cracks in irrigated furrow north of the short probes, the crack running orthogonal to the furrow in the centre of the image intersects the centre of the measurement area; b+c: Water flow in soil cracks preceding the surface water flow.

Figures 7.9b and c.

Interestingly, the anisotropy profiles that were measured at the short probes, before irrigations 3 and 5 show a deviation in different directions relative to the non cracked soil conditions after the irrigation events. Before irrigation 3 the AI in Figure 7.8a deviates to the right of the moist anisotropy profile, while the AI before irrigation 5 (Figure 7.8b) deviates to the left. This difference in AI deviation is particularly interesting considering the present debate about the tendency of a soil crack to reappear at a previous crack location (refer to Section 2.1.2). Present observations on crack reappearance are based on observations of the surface crack network (Waller and Wallender, 1993; White, 2001; Wells et al., 2003; Greve et al., 2010), which might or might not be representative of the subsurface cracks. A difference in the direction of the AI deviation of a final crack network would indicate an alteration in the subsurface crack network. However, as it is not known whether the two crack networks before irrigations 3 and 5 were stable, the observed differences in the AI deviation might simply be due to differences in the two cracking stages. Even though the presented results are not conclusive, they do highlight a promising future application of the AI.

As discussed in Chapter 6, a well developed anisotropy deviation can give infor-

mation about the cracking depth range. This range lies between the depth of the last deviation maxima and the depth where the AI deviation ends and the AI returns to the AI of the non cracked soil. Before irrigation 3, the short profile indicates a cracking depth between 0.425 and 0.575 m (Figure 7.8a). The long anisotropy profile, which starts at 0.5 m depth and does not show an AI deviation, indicates a cracking depth of $<$ 0.5 m (Figure 7.7a). With the upper end of the long AI profile in the middle of the cracking depth range given by the short profile, the cracking information given by both profiles is consistent. The same consistency is observed before irrigation 5, where the short profile gives a cracking depth between 0.500 and 0.725 m and the long profile gives a depth range between 0.55 and 0.75 m (Figures 7.7b and 7.8b). Considering the different electrode spacings on the two probe sets, a better overlap of cracking depth range could not have been achieved between the two profiles.

Method	Short probes	Long probes
AI-Cracking depth range	0.5-0.725 m	0.55-0.75 m
ERT-Max depth of crack affected areas	0.55 m	0.72 m
ERT-Max depth of resisitivity change	0.95 m	1.15 m
Neutrone probe-Max depth of change in ϑ	0.8 m	

Table 7.1: Cracking depth before irrigation 5 as indicated by different methods

In Table 7.1 , this crack depth range is compared to the crack affected areas in the 3D ERT images (Figure 7.10), which is defined as in Chapter 6. Before irrigation 3, no crack affected area was located in the short image (Note: ERT measurements at the long probes were not completed before irrigation 3, refer to Section 7.1). However, for irrigation 5, a crack affected area was located in both the long and the short image. For the image taken with the short probes, the crack affected area reaches a depth of 0.55 m, while for the image taken with the long probes it goes to a depth of 0.72 m. Both depths are within the cracking depth range of the anisotropy profiles. The lack of crack affected area before irrigation 3 is not surprising considering that the cracking depth range indicated by the anisotropy profile only just entered the measurement

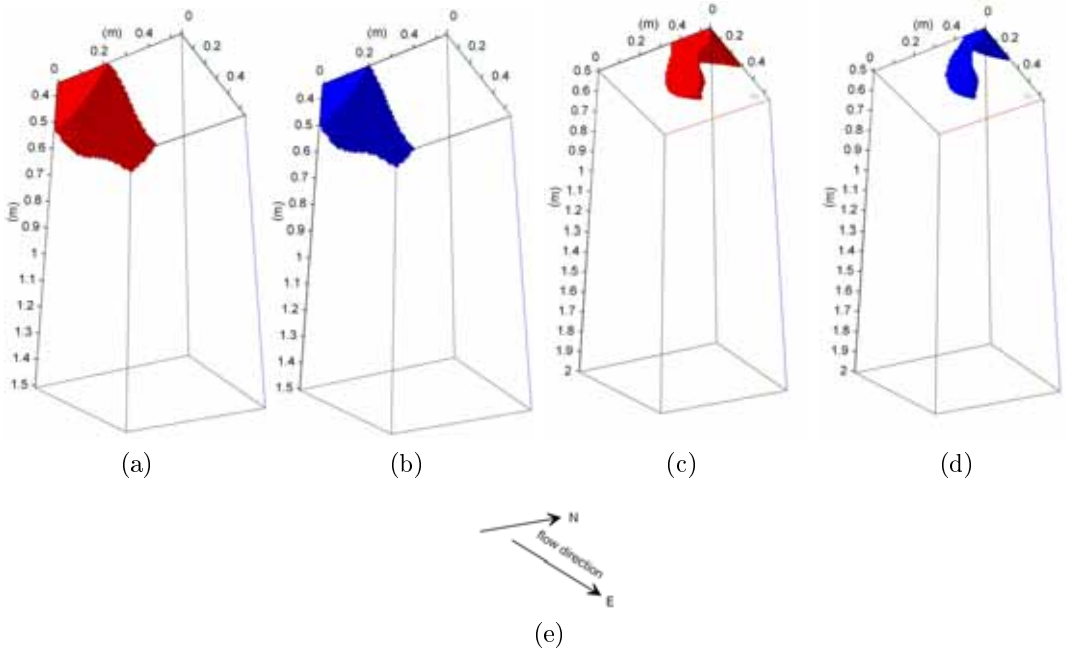

Figure 7.10: Crack affected image areas; a+c: Areas with a bulk resistivity of >100 Ωm before irrigation 5 at short and long probe set, respectively; b+d: Areas where a bulk resistivity change of >100 Ωm occurred during irrigation 5 at short and long probe set, respectively.

area and taking into account the previously discussed limited sensitivity at the top of the measurement plane.

Another indication of the cracking depth (also shown in Table 7.1) is the depth of soil moisture change observed in the neutron probe readings and the 3D ERT images. The maximum depth of soil moisture change during irrigation 5 is 0.8 m based on the neutron probe readings (Figure 7.2), 0.95 m for the short ERT image (Figure 7.5), and 1.15 m in the long ERT image (7.6). This confirms that cracks must have allowed water to percolate through the compacted soil layer between 0.3 and 0.6 m, as the low hydraulic conductivities of this layer would not have allowed water to reach the observed depth within the 25 h between water application and the post-irrigation neutron probe and ERT readings. This is consistent with the cracking depths derived from the anisotropy profiles, which also indicate that cracks penetrated the compacted layer. The observed percolation through the flow restricting soil layer highlights another management advantage of reliable crack depth detection. If the presence of a compacted and water flow restricting layers is known, the irrigation

intervals can be manipulated to allow the formation of cracks through this layer and hence water transport to the desired depth of the profile.

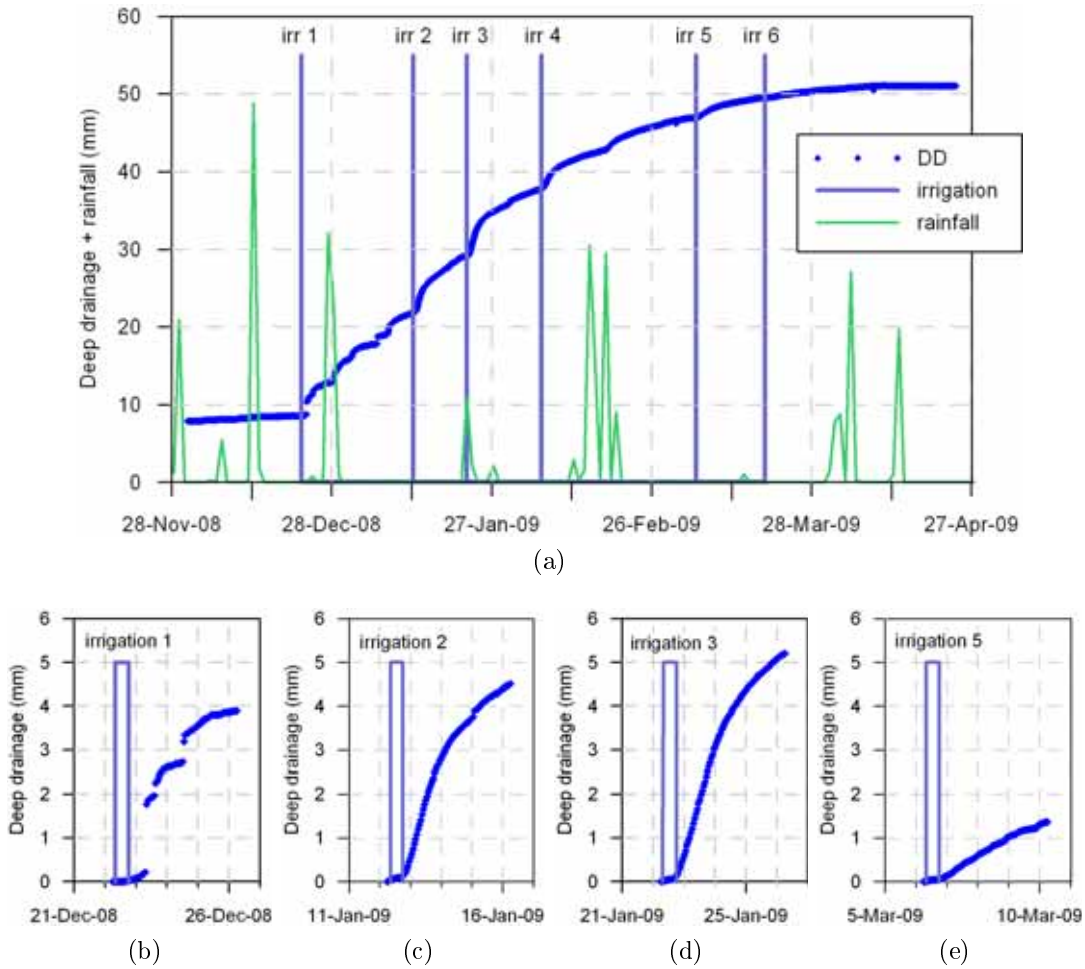

Figure 7.11: Deep drainage collected with the variable tension lysimeter; a: Accumulated drainage for the entire cotton growing season 2008-09; b-e: Detailed drainage following the four monitored irrigation events.

Figure 7.11 shows the drainage that was collected at the variable tension lysimeter at the field site. A detailed view of the drainage response for the four monitored irrigation events within four days of the start of the irrigation is shown in Figures 7.11b-e. The largest response within this time frame occurred for irrigation 3. Irrigation 1, which had the highest pre-irrigation SWC and irrigation 5, which had the lowest pre-irrigation SWC, resulted in the two lowest drainage responses. This appears counter intuitive to the proposed mechanisms of deep drainage, which would suggest deep drainage either during wet soil conditions when the irrigation exceeds the soil moisture deficit (Smith et al., 2005; Ringrose-Voase, 2008) or during dry soil

conditions when soil cracks provide deep pathways for preferential flow (Beven and Germann, 1982; Kosmas et al., 1991; Harris et al., 1994; Bronswijk et al., 1995; Lin and McInnes, 1995; Tuong et al., 1996). A closer investigation of the soil conditions might help to explain the measured deep drainage responses.

As irrigation 1 was applied to the profile with the lowest soil moisture deficit, a higher deep drainage response could have been expected (Smith et al., 2005; Ringrose-Voase, 2008). The observed moderate drainage response could be attributed to the presence of the compacted soil layer at 0.3 to 0.6 m combined with the reduced cracking depth in the relatively moist profile. The large insertion depth of the resistivity probes did not allow the detection of a cracking depth range for the profile before irrigation 1. However, considering the relatively moist soil conditions, it is likely that the soil cracks before irrigation 1 were shallower than before irrigations 2, 3 and 5. Earlier in this section it was concluded that soil cracks must have provided preferential flow paths through the compacted layer. A shallower crack system and hence a lack of preferential flow paths through the compacted layer would restrict water flow into deeper layers of the soil, which could provide an explanation for the relatively low deep drainage response after irrigation 1. Furthermore, the good rains that occured in the early part of the season would have caused soil wetting from the top of the profile, which could have sealed possible cracks at the surface.

The increased depth of soil cracking before irrigation 5 could have suggested an increased deep drainage response, which was not observed (Figure 7.11e). Deep drainage was collected at 2 m, while the cracking depth range derived from the anisotropy profiles before irrigation 5 was between 0.5 and 0.75 m. The depth of soil drying (0.95 and 1.15 m based on the two ERT images, 1.1 m based on the neutron probe readings) exceeded the cracking depth, which is a likely explanation for the low deep drainage response after irrigation 5. Preferential flow through the cracks would have re-infiltrated into the dry soil matrix below the cracks (Van Stiphout et al., 1987). Additionally, water might also have infiltrated laterally into the crack walls, however lateral infiltration is commonly assumed to be low in cracking clays (Hoogmoed and

Bouma, 1980; Bronswijk, 1988). The varying deep drainage response throughout the growing season highlights the complexity of deep drainage mechanisms in cracking soils and the need to improve our present understanding of deep drainage processes.

The growths of the cotton root system throughout the monitored period showed no significant influence on the AI measurements, which is consistent with the observations made under sorghum roots at the Maules Creek site described in Chapter 6. Similar to the measurements at the Maules Creek site, the three error measurements (tripotential, stacked, and reciprocal error) indicate good quality resistivity data. The stacked and reciprocal errors were comparable to those reported in Chapter 6, while the measured tripotential errors were elevated and reached values of up to 15 %. These high tripotential errors occurred during crack closure in irrigation 5, which indicates that changes in the resistivity during crack filling occurred faster than the ~3 s time span for the collection of the alpha, beta and gamma array at each electrode depth. However, for the remaining square array measurements the tripotential errors were $\leq$5 %, which indicated good data quality.

7.3 Conclusions

This trial further confirmed the suitability of anisotropy profiles for subsurface crack detection. Furthermore, this chapter highlights the advantages of 3D ERT tomography, which can be carried out with the same electrode array used for the collection of anisotropy profiles. 3D ERT tomography is able to capture the spatial soil moisture variations, which are especially pronounced in cracking soils. This ability is a clear advantage over other soil moisture measurements, such as neutron probe readings.

The observed variation in the deep drainage response throughout the growing season highlights the complexity of deep drainage mechanisms in cracking soils and the need to improve our present understanding of these mechanisms. Monitoring soil moisture changes, preferential flow, and cracking depth will all greatly aid in doing

so, and this chapter showed that resistivity measurements allow all of the above.

Chapter 8

Summary and Conclusions

Described in this thesis is a new approach for delineating the presence of soil cracks using an anisotropy index based on electrical resistivity measurements. The anisotropy index is the ratio of the alpha and beta apparent resistivity measured with the square array. An electrode arrangement is described that allows the collection of anisotropy indices at various depths within a soil profile. Four electrode strings are installed vertically in the subsurface forming a series of horizontal coplanar electrode squares. The series of coplanar electrode squares allows measurements of the alpha and beta apparent resistivities at each electrode depth and hence the calculation of AI depth profiles.

After the introduction of the anisotropy profiles, their ability to detect soil cracks below the soil surface was examined, first in numerical and laboratory studies on simplified and natural crack networks and later in two field studies. Due to the present lack of methods for monitoring subsurface soil cracks, another indirect crack measure was necessary to allow comparison with the AI results of the two field studies. Therefore, a short and a long 3D electrical resistivity tomography routine was developed to monitor the electrical resistivity distribution between the four electrode strings. The 3D ERT routines were designed to utilise the same electrode array as used to collect the anisotropy profiles. Monitoring the 3D bulk resistivity distribution not only gave an indication of the extent of subsurface cracking but also allowed the detection of soil drying and wetting. The short 3D ERT routine run in time lapse setting during

the water application, allowed monitoring of the infiltration of the irrigation water. Observation of preferential flow during the irrigation gave indications of the extent and depth of soil cracking, which could be compared to the results from the anisotropy profiles. Furthermore, the high resolved ERT images collected with the long ERT routine could be used to identify crack affected zones in the measurement area. Zones in the pre-irrigation image that had atypically high resistivities for clay soils were assumed to contain cracks, while areas that went through atypically high bulk resistivity changes during the irrigation events were assumed to be affected by crack closure.

Even though the measurements of the anisotropy indices and the 3D ERT images were carried out with the same instrumentation, they provided two independent crack measures, as the inverted resistivities of the resistivity tomography are independent of the electrical anisotropy that is measured with the AI method. The results of the resistivity measurements in the field were compared to: soil temperature changes due to water arrival, soil moisture changes measured with neutron probes, and deep drainage collected in a variable tension lysimeter at 2 m depth.

The numerical, laboratory and field studies confirmed the initial hypothesis that anisotropy indices can be used to monitor the depth of subsurface soil cracking. The studies of simple crack scenarios showed that the AI deviation of a single crack is a function of its location, depth, length and orientation relative to the electrode strings. If two cracks are present and intersect, the location of their intersection point and their angles to each other also become important. Two crack scenarios that could not be detected through an AI deviation were identified: Diagonal cracks that intersected the modelling area at an angel of 45° and two orthogonal cracks of identical length that cross each other in the centre of the modelling area. However, as these two scenarios are unlikely to occur in natural crack systems and as each slight variation from these two scenarios results in an anisotropy response, they do not compromise the suitability of anisotropy profiles for detecting cracks in soil.

Crack networks forming in soils show complex patterns with a lack of clear di-

rectional dependence. The investigations of natural crack scenarios showed that soil cracks cause a directional dependence of current flow even if they lack a preferred crack orientation. This causes natural crack patterns to strongly affect the anisotropy index. In addition to the qualitative crack information that can be derived from the AI, a well developed anisotropy profile with multiple local AI deviation minima and maxima enables determination of a depth range for the maximum crack depth.

Soil crack dynamics in a soil profile are inevitably driven by soil moisture changes, however the results show that it is the presence of the cracks and not soil moisture changes that dominate the AI. Furthermore, changes in sorghum and cotton root system throughout a growing season had only minor influence on the index. Even though soils cracks dominate the AI, background inhomogeneities still influence the AI deviation, so that the deviation from a crack free condition needs to be investigated rather that the AI deviation from unity.

Three dimensional ERT routines developed in this study allowed successful monitoring of soil moisture changes during irrigation events and mapping of the spatial heterogeneity in the soil water content within the root zone. Furthermore, the routines could delineate infiltration dominated by matrix flow from infiltration dominated by preferential flow.

It is concluded that electrical resistivity measurements are an excellent tool for irrigation and deep drainage management. Collection of the novel anisotropy profiles as well as of specially designed 3D ERT routines can both be carried out with the same electrode arrangement and instrumentation. Anisotropy profiles allow the monitoring of the dynamics of subsurface cracks and the measurement of the depth to which the cracks extend. 3D ERT gives information about soil moisture change, preferential flow, and the extent of the crack affected area. Even though anisotropy profiles and 3D ERT measurements are both based on resistivity measurements, their results are independent from each other as the electrical anisotropy measured with the AI is not related to the inverted resistivities from ERT. This independence, as well as the unique possibility of *in situ* monitoring of subsurface cracks and the ability to capture spatial

soil moisture variation, makes resistivity measurements with the proposed electrode array an especially unique tool for farm use and for research applications.

Continued use of the methods developed in this thesis under a variety of field conditions will further advance our knowledge about the dynamic behaviour of soil cracks and the impacts of cracking on water infiltration. Global improved water use efficiency is required for most irrigated crops, which requires an improved understanding of the interplay between irrigation scheduling, soil cracking, deep drainage and maximising crop yield with minimal water requirements. The anisotropy profiles, together with the 3D ERT routines presented in this thesis, provide a significant step towards advancing water use efficiency of irrigated crops through improved monitoring of the impacts of cracks on the water distribution to plants.

Bibliography

Acworth, R., 1999. Investigation of dryland salinity using the electrical image method. Australian Journal of Soil Research 37 (4), 623–636.

Acworth, R., Jorstad, L., 2006. Integration of multi-channel piezometry and electrical tomography to better define chemical heterogeneity in a landfill leachate plume within a sand aquifer. Journal of Contaminant Hydrology 83 (3-4), 200–220.

Alumbaugh, D. L., Newman, G. A., 2000. Image appraisal for 2-D and 3-D electromagnetic inversion. Geophysics 65 (5), 1455–1467.

Austin, N. R., Prendergast, J. B., 1997. Use of kinematic wave theory to model irrigation on cracking soil. Irrigation Science 18 (1), 1–10.

Batlle-Aguilar, J., Schneider, S., Pessel, M., Tucholka, P., Coquet, Y., Vachier, P., 2009. Axisymetrical infiltration in soil imaged by noninvasive electrical resistivimetry. Soil Science Society of America Journal 73 (2), 510–520.

Bell, J., 1976. Neutron probe practice. Institute of Hydrology.

Bentley, L. R., Gharibi, M., 2004. Two- and three-dimensional electrical resistivity imaging at a heterogeneous remediation site. Geophysics 69 (3), 674–680.

Beven, K., Germann, P., 1982. Macropores and water-flow in soils. Water Resources Research 18 (5), 1311–1325.

Bing, Z., Greenhalgh, S., 1997. A synthetic study on cross-hole resistivity imaging with different electrode arrays. Exploration Geophysics 28 (1-2), 1–5.

Bing, Z., Greenhalgh, S., 2000. Cross-hole resistivity tomography using different electrode configurations. Geophysical Prospecting 48 (5), 887–912.

Binley, A., HenryPoulter, S., Shaw, B., 1996. Examination of solute transport in an undisturbed soil column using electrical resistance tomography. Water Resources Research 32 (4), 763–769.

Boadu, F. K., Gyamfi, J., Owusu, E., 2005. Determining subsurface fracture characteristics from azimuthal resistivity surveys: A case study at Nsawam, Ghana. Geophysics 70 (5), B35–B42.

Boivin, P., 2007. Anisotropy, cracking, and shrinkage of vertisol samples - experimental study and shrinkage modeling. Geoderma 138 (1-2), 25–38.

Boivin, P., Garnier, P., Tessier, D., 2004. Relationship between clay content, clay type, and shrinkage properties of soil samples. Soil Science Society of America Journal 68 (4), 1145–1153.

Boivin, P., Garnier, P., Vauclin, M., 2006. Modeling the soil shrinkage and water retention curves with the same equations. Soil Science Society of America Journal 70 (4), 1082–1093.

Booltink, H. W. G., Bouma, J., 1993. Sensitivity analysis on processes affecting bypass flow. Hydrological Processes 7 (1), 33–43.

Bouma, J., 1981. Soil morphology and preferential flow along macropores. Agricultural Water Management 3 (4), 235–250.

Bouma, J., 1990. Using morphometric expressions for macropores to improve soil physical analyses of field soils. Geoderma 46 (1-3), 3–11.

Bouma, J., Anderson, J. L., 1977. Water and chloride movement through soil columns simulating pedal soils. Soil Science Society of America Journal 41 (4), 766–770.

Bouma, J., Dekker, L. W., 1978. Case-study on infiltration into dry clay soil 1. Morphological observations. Geoderma 20 (1), 27–40.

Bouma, J., Dekker, L. W., Wosten, J. H. M., 1978. Case-study on infiltration into dry clay soil 2. Physical measurements. Geoderma 20 (1), 41–51.

Bronswijk, J. J. B., 1988. Modeling of water-balance, cracking and subsidence of clay soils. Journal of Hydrology 97 (3-4), 199–212.

Bronswijk, J. J. B., Hamminga, W., Oostindie, K., 1995. Rapid nutrient leaching to groundwater and surface water in clay soil areas. European Journal of Agronomy 4 (4), 431–439.

Busby, J., Jackson, P., 2006. The application of time-lapse azimuthal apparent resistivity measurements for the prediction of coastal cliff failure. Journal of Applied Geophysics 59 (4), 261–272.

Campbell, R., Bower, C., Richards, L., 1949. Change of electrical conductivity with temperature and the relation of osmotic pressure to electrical conductivity and ion concentration for soil extracts. Soil Science Society of America Proceedings 13 (C), 66–69.

Carpenter, E. W., 1955. Some notes concerning the Wenner configuration. Geophysical Prospecting 3 (4), 388–402.

Carpenter, E. W., Habberjam, G. M., 1956. A tri-potential method of resistivity prospecting. Geophysics 21 (2), 455–469.

Chertkov, V. Y., 2000. Using surface crack spacing to predict crack network geometry in swelling soils. Soil Science Society of America Journal 64 (6), 1918–1921.

Chertkov, V. Y., 2003. Modelling the shrinkage curve of soil clay pastes. Geoderma 112 (1-2), 71–95.

Chertkov, V. Y., 2007. The reference shrinkage curve of clay soil. Theoretical and Applied Fracture Mechanics 48 (1), 50–67.

Chertkov, V. Y., Ravina, I., 1998. Modeling the crack network of swelling clay soils. Soil Science Society of America Journal 62 (5), 1162–1171.

Chertkov, V. Y., Ravina, I., 2000. Shrinking-swelling phenomenon of clay soils attributed to capillary-crack network. Theoretical and Applied Fracture Mechanics 34 (1), 61–71.

Coleman, E., Hendrix, T., 1949. The fiberglass electrical soil-moisture instrument. Soil Science (67), 425–438.

Colina, H., Roux, S., 2000a. Experimental model of cracking induced by drying shrinkage. European Physical Journal 1 (2-3), 189–194.

Colina, H., Roux, S., 2000b. Experimental model of saturated soils as they dry and shrink. European Journal of Soil Science 53, 105–118.

Cornelis, W. M., Corluy, J., Medina, H., Hartmann, R., Van Meirvenne, M., Ruiz, M. E., 2006. A simplified parametric model to describe the magnitude and geometry of soil shrinkage. European Journal of Soil Science 57 (2), 258–268.

Dahlin, T., 2000. Short note on electrode charge-up effects in DC resistivity data acquisition using multi-electrode arrays. Geophysical Prospecting 48 (1), 181–187.

Dahlin, T., Loke, M. H., 1998. Resolution of 2D wenner resistivity imaging as assessed by numerical modelling. Journal of Applied Geophysics 38 (4), 237–249.

Dahlin, T., Zhou, B., 2004. A numerical comparison of 2D resistivity imaging with 10 electrode arrays. Geophysical Prospecting 52 (5), 379–398.

Daily, W., Ramirez, A., Labrecque, D., Nitao, J., 1992. Electrical-resistivity tomography of vadose water-movement. Water Resources Research 28 (5), 1429–1442.

Darboux-Afouda, R., Louis, P., 1989. Contribution des mesures de l'anisotropie electique a la recherche des aquiferes de fracture an milieu cristallin au benin. Geophysical Prospecting 37, 91–105.

Day-Lewis, F., White, E., Johnson, C., Lane, J., Belaval, M., 2006. Continuous resistivity profiling to delineate submarine groundwater discharge - examples and limitations. The leading Edge 25, 724–728.

deGroot Hedlin, C., Constable, S., 1990. Occam inversion to generate smooth, 2-dimensional models from magnetotelluric data. Geophysics 55 (12), 1613–1624.

Deiana, R., Cassiani, G., Kemna, A., Villa, A., Bruno, V., Bagliani, A., 2007. An experiment of non-invasive characterization of the vadose zone via water injection and cross-hole time-lapse geophysical monitoring. Near Surface Geophysics 5 (3), 183–194.

Dey, A., Morrison, H. F., 1979. Resistivity modeling for arbitrarily shaped 3-dimensional structures. Geophysics 44 (4), 753–780.

Freud, L. B., 1998. Dynamic Fracture Mechanics. Cambridge University Press, Cambridge.

Furman, A., Ferre, T. P. A., Warrick, A. W., 2003. A sensitivity analysis of electrical resistivity tomography array types using analytical element modeling. Vadose Zone Journal 2 (3), 416–423.

Furman, A., Ferre, T. P. A., Warrick, A. W., 2004. Optimization of ERT surveys for monitoring transient hydrological events using perturbation sensitivity and genetic algorithms. Vadose Zone Journal 3 (4), 1230–1239.

Furman, A., Warrick, A. W., Ferre, T. P. A., 2002. Electrical potential distributions in a heterogeneous subsurface in response to applied current: Solution for circular inclusions. Vadose Zone Journal 1 (2), 273–280.

Gill, J., Tisdall, J., Sukartono., Kusnarta, I., McKenzie, B., 2004. Physical properties of clay loam soil mixed with sand. In: SuperSoil2004. Sydney, NSW.

Graphics, D., 2009. Earth Vision 7.5. Dynamic Graphics, INC., available from www.dgi.com (access data: Nov. 2009).

Greve, A., Andersen, M., Acworth, R. I., 2010. Investigations of soil cracking and preferential flow in a weighing lysimeter filled with cracking clay soil. Journal of Hydrology available online: DOI: 10.1016/j.jhydrol.2010.03.007.

Groenevelt, P. H., Bolt, G. H., 1972. Water retention in soil. Soil Science 113, 238–245.

Groisman, A., Kaplan, E., 1994. An experimental-study of cracking induced by desiccation. Europhysics Letters 25 (6), 415–420.

Habberjam, G., 1967. On application of reciprocity theorem in resistivity prospecting. Geophysics 32 (5), 918–919.

Habberjam, G., 1972. The effects of anisotropy on square array resistivity measurements. Geophysical Prospecting 20 (2), 249–266.

Habberjam, G., 1975. Apparent resistivity, anisotrophy and strike measurements. Geophysical Prospecting 23 (2), 211–247.

Hagrey, S., 2007. Geophysical imaging of root-zone, trunk, and moisture heterogeneity. Journal of Experimental Botany 58 (4), 839–854.

Haines, W. B., 1923. The volume changes associated with variations of water content in soil. Journal of Agricultural Science (13), 296–311.

Harris, G. L., Nicholls, P. H., Bailey, S. W., Howse, K. R., Mason, D. J., 1994. Factors influencing the loss of pesticides in drainage from a cracking clay soil. Journal of Hydrology 159 (1-4), 235–253.

Hayley, K., Bentley, L. R., Gharibi, M., Nightingale, M., 2007. Low temperature dependence of electrical resistivity: Implications for near surface geophysical monitoring. Geophysical Research Letters 34 (18).

Hearn, A., Cameron, J., Jackson, B., 1997. Water use efficiency: If you don't measure it, you can't manage it. Australian Cotton Grower 18 (6), 88–94.

Hendriks, R., Oostindie, K., Hamminga, P., 1999. Simulation of bromide tracer and nitrogen transport in a cracked clay soil with the FLOCR/ANIMO model combination. Journal of Hydrology 215 (1-4), 94–115.

Herwanger, J. V., Pain, C. C., Binley, A., de Oliveira, C. R. E., Worthington, M. H., 2004. Anisotropic resistivity tomography. Geophysical Journal International 158 (2), 409–425.

Hoogmoed, W. B., Bouma, J., 1980. A simulation-model for predicting infiltration into cracked clay soil. Soil Science Society of America Journal 44 (3), 458–461.

Hupet, F., Vanclooster, A., 2005. Micro-variability of hydrological processes at the maize row scale: Implications for soil water content measurements and evapotranspiration estimates. Journal of Hydrology 303 (1-4), 247–270.

Johnson, H. H., 1965. Calibrating electric potential method for studying slow crack growth. Materials Research and Standards 5 (9), 442–445.

Johnston, J., Hill, H., 1944. A study of the shrinking and swelling properties of renzina soils. Soil Science Society of America Proceedings 9, 24–29.

Keller, G., Frischknecht, K., 1966. Electrical Methods in Geophysical Prospecting, 1st Edition. Vol. 10 of International Series of Monographs in Electromagnetic Waves. Pergamon Press, Oxford.

Kim, J. H., Yi, M. J., Cho, S. J., Son, J. S., Song, W. K., 2006. Anisotropic crosshole resistivity tomography for ground safety analysis of a high-storied building over an abandoned mine. Journal of Environmental and Engineering Geophysics 11 (4), 225–235.

Kishne, A. S., Morgan, C. L. S., Miller, W. L., 2009. Vertisol crack extent associated with gilgai and soil moisture in the Texas gulf coast prairie. Soil Science Society of America Journal 73 (4), 1221–1230.

Koestel, J., Kemna, A., Javaux, M., Binley, A., Vereecken, H., 2008. Quantitative imaging of solute transport in an unsaturated and undisturbed soil monolith with 3D ERT and TDR. Water Resources Research 44 (12), W12411.

Koestel, J., Vanderborght, J., Javaux, M., Kemna, A., Binley, A., Vereecken, H., 2009. Noninvasive 3D transport characterization in a sandy soil using ERT: 1. Investigating the validity of ERT-derived transport parameters. Vadose Zone Journal 8 (3), 711–722.

Kosmas, C., Moustakas, N., Kallianou, C., Yassoglou, N., 1991. Cracking patterns, bypass flow and nitrate leaching in Greek irrigated soils. Geoderma 49 (1-2), 139–152.

Labrecque, D., Daily, W., 2008. Assessment of measurement errors for galvanic-resistivity electrodes of different composition. Geophysics 73 (2), F55–F64.

LaBrecque, D. J., Heath, G., Sharpe, R., Versteeg, R., 2004a. Autonomous monitoring of fluid movement using 3-D electrical resistivity tomography. Journal of Environmental and Engineering Geophysics 9 (3), 167–176.

LaBrecque, D. J., Ramirez, A. L., Daily, W. D., Binley, A. M., Schima, S. A., 1996. ERT monitoring on environmental remediation processes. Measurement Science & Technology 7 (3), 375–383.

LaBrecque, D. J., Sharpe, R., Wood, T., Heath, G., 2004b. Small-scale electrical resistivity tomography of wet fractured rocks. Ground Water 42 (1), 111–118.

Lane, J. W., Haeni, F. P., Watson, W. M., 1995. Use of a square-array direct-current resistivity method to detect fractures in crystalline bedrock in New-Hampshire. Ground Water 33 (3), 476–485.

Lecocq, N., Vandewalle, N., 2002. Experimental study of cracking induced by desiccation in 1-dimensional systems. European Physical Journal 8 (4), 445–452.

Lima, L. A., Grismer, M. E., 1992. Soil crack morphology and soil-salinity. Soil Science 153 (2), 149–153.

Lin, H. S., McInnes, K. J., 1995. Water-flow in clay soil beneath a tension infiltrometer. Soil Science 159 (6), 375–382.

Loke, M., 1996-2004. Tutorial: 2-D and 3-D electrical imaging surveys. Geotomo Software, Gelugor, Malaysia, available from www.geoelectrical.com (access data: Nov. 2009).

Loke, M., July 2002. Res2Dmod ver. 3.01. Geotomo software, Gelugor, Malaysia, available from www.geoelectrical.com (access data: Nov. 2009).

Loke, M. H., 2008. Res3Dinvx64 ver. 3.02.07. Geotomo Software, Gelugor, Malaysia, available from www.geoelectrical.com (access data: Nov. 2009).

Loke, M. H., 2009a. Res2Dinv ver. 3.58.46. Geotomo Software, Gelugor, Malaysia, available from www.geoelectrical.com (access data: Nov. 2009).

Loke, M. H., 2009b. Res3Dmodx64 ver. 3.00.09. Geotomo Software, Gelugor, Malaysia, available from www.geoelectrical.com (access data: Nov. 2009).

Loke, M. H., Acworth, R. I., Dahlin, T., 2003. A comparison of smooth and blocky inversion methods in 2D electrical imaging surveys. Exploration Geophysics 34 (3), 182–187.

Loke, M. H., Barker, R. D., 1996. Rapid least-squares inversion of apparent resistivity pseudosections by a quasi-Newton method. Geophysical Prospecting 44 (1), 131–152.

Looms, M. C., Jensen, K. H., Binley, A., Nielsen, L., 2008. Monitoring unsaturated flow and transport using cross-borehole geophysical methods. Vadose Zone Journal 7 (1), 227–237.

Mansoor, N., 2007. High-resolution geophysical imaging of shallow-water, contaminated wetlands: a novel application to kearny freshwater marsh, New Jersey Meadowlands. Ph.D. thesis, The State University of New Jersey.

MathWorks, T., 2007. Matlab R2007b. The MathWorks, available from www.mathworks.com (access data: Nov. 2009).

McGillivray, P. R., Oldenburg, D. W., 1990. Methods for calculating Frechet derivatives and sensitivities for the nonlinear inverse problem - a comparative-study. Geophysical Prospecting 38 (5), 499–524.

Merriam, J. B., 2005. Injection electrode overprinting. Journal of Environmental and Engineering Geophysics 10 (4), 365–370.

Miller, C. R., Routh, P. S., 2007. Resolution analysis of geophysical images: Comparison between point spread function and region of data influence measures. Geophysical Prospecting 55 (6), 835–852.

Miller, C. R., Routh, P. S., Brosten, T. R., McNamara, J. P., 2008. Application of time-lapse ERT imaging to watershed characterization. Geophysics 73 (3), G7–G17.

Mitchell, A. R., Vangenuchten, M. T., 1993. Flood irrigation of a cracked soil. Soil Science Society of America Journal 57 (2), 490–497.

Murdoch, L. C., 1993. Hydraulic fracturing of soil during laboratory experiments: 2. Propagation. Geotechnique 43 (2), 267–276.

Nimmer, R. E., Osiensky, J. L., Binley, A. M., Sprenke, K. F., Williams, B. C., 2007. Electrical resistivity imaging of conductive plume dilution in fractured rock. Hydrogeology Journal 15 (5), 877–890.

Nimmer, R. E., Osiensky, J. L., Binley, A. M., Williams, B. C., 2008. Three-dimensional effects causing artifacts in two-dimensional, cross-borehole, electrical imaging. Journal of Hydrology 359 (1-2), 59–70.

Oldenborger, G., Routh, P., Knoll, M., 2005. Sensitivity of electrical resistivity tomography data to electrode position errors. Geophysical Journal International 163 (1), 1–9.

Oldenborger, G. A., Routh, P. S., Knoll, M. D., 2007. Model reliability for 3D electrical resistivity tomography: Application of the volume of investigation index to a time-lapse monitoring experiment. Geophysics 72 (4), F167–F175.

Oldenburg, D. W., Li, Y. G., 1999. Estimating depth of investigation in DC resistivity and IP surveys. Geophysics 64 (2), 403–416.

Park, S. K., Van, G. P., 1991. Inversion of pole-pole data for 3-D resistivity structure beneath arrays of electrodes. Geophysics 56 (7), 951–960.

Peng, X., Horn, R., 2005. Modeling soil shrinkage curve across a wide range of soil types. Soil Science Society of America Journal 69 (3), 584–592.

Python, 2008. Python ver 2.5.2. Available from www.python.org (access data: Nov. 2009).

Ramirez, A., W.D., D., Newmark, R., 1995. Electrical resistance tomography for steam injection monitoring and control. Journal of Environmental and Engineering Geophysics 0 (1), 39–52.

Reza, F., Yamamuro, J. A., Batson, G. B., 2004. Electrical resistance change in compact tension specimens of carbon fiber cement composites. Cement & Concrete Composites 26 (7), 873–881.

Rinaldi, V. A., Cuestas, G. A., 2002. Ohmic conductivity of a compacted silty clay. Journal of Geotechnical and Geoenvironmental Engineering 128 (10), 824–835.

Ringrose-Voase, A., Sanidad, W., 1996. A method for measuring the development of surface cracks in soils: Application to crack development after lowland rice. Geoderma 71 (3-4), 245–261.

Ringrose-Voase, A. J., 2008. Water balance and deep drainage under irrigated cotton. Tech. rep., WATERpak, Narrabri, NSW :Australian Cotton CRC.

Ringrose-Voase, A. J., Nadelko, A., 2006. Quantifying deep drainage using lysimetry. Tech. Rep. 56/06, CSRIO Land and Water Science Report.

Ritzi, R. W., Andolsek, R. H., 1992. Relation between anisotropic transmissivity and azimuthal resistivity surveys in shallow, fractured, carbonate flow systems. Ground Water 30 (5), 774–780.

Rugh, D. F., Burbey, T. J., 2008. Using saline tracers to evaluate preferential recharge in fractured rocks, Floyd County, Virginia, USA. Hydrogeology Journal 16 (2), 251–262.

Said Attia al, H., 1994. Electric study of fracture anisotropy at Falkenberg, Germany. Geophysics 59 (6), 881–888.

Samouelian, A., Cousin, I., Richard, G., Tabbagh, A., Bruand, A., 2003. Electrical resistivity imaging for detecting soil cracking at the centimetric scale. Soil Science Society of America Journal 67 (5), 1319–1326.

Samouelian, A., Richard, G., Cousin, I., Guerin, R., Bruand, A., Tabbagh, A., 2004. Three-dimensional crack monitoring by electrical resistivity measurement. European Journal of Soil Science 55 (4), 751–762.

Sasaki, Y., 1992. Resolution of resistivity tomography inferred from numerical simulation. Geophysical Prospecting 40 (4), 453–463.

Saxena, A., 1980. Electrical potential technique for monitoring subcritical crack-growth at elevated-temperatures. Engineering Fracture Mechanics 13 (4), 741–750.

Sharma, P., 1997. Environmental and engineering geophysics. Cambridge University Press, Cambridge.

Shima, H., Sakashita, S., Kobayashi, T., 1996. Developments of non-contact data acquisition techniques in electrical and electromagnetic explorations. Journal of Applied Geophysics 35 (2-3), 167–173.

Shima, H., Sakayama, T., 1987. Resistivity tomography: An approach to 2D resistivity inverse problems. In: Geophysicists, S. o. E. (Ed.), 57th SEG meeting. New Orleans, pp. 59–61.

Shorlin, K. A., de Bruyn, J. R., Graham, M., Morris, S. W., 2000. Development and geometry of isotropic and directional shrinkage-crack patterns. Physical Review 61 (6), 6950–6957.

Silburn, M., Montgomery, J., 2001. Deep drainage under irrigated cotton in Australia: A review. In: Cotton Consultants Association Meeting.

Slater, L., Binley, A., Versteeg, R., Cassiani, G., Birken, R., Sandberg, S., 2002. A 3D ERT study of solute transport in a large experimental tank. Journal of Applied Geophysics 49 (4), 211–229.

Slater, L., Binley, A. M., Daily, W., Johnson, R., 2000. Cross-hole electrical imaging of a controlled saline tracer injection. Journal of Applied Geophysics 44 (2-3), 85–102.

Slater, L. D., Binley, A., Brown, D., 1997. Electrical imaging of fractures using ground-water salinity change. Ground Water 35 (3), 436–442.

Sleeman, J., 1963. Cracks, peds and their surface in some soils of the Riverine Plain, New South Wales. Australian Journal of Soil Research 1 (1), 91–102.

Smith, R. J., Raine, S. R., Minkevich, J., 2005. Irrigation application efficiency and deep drainage potential under surface irrigated cotton. Agricultural Water Management 71 (2), 117–130.

Steenhuis, T. S., Richard, T. L., Parlange, M. B., Aburime, S. O., Geohring, L. D., Parlange, J. Y., 1988. Preferential flow influences on drainage of shallow sloping soils. Agricultural Water Management 14 (1-4), 137–151.

Stirk, G., 1954. Some aspects of soil shrinkage and the effect of cracking upon water entry into the soil. Australian Journal of Agricultural Research 5 (2), 279–290.

Stummer, P., Maurer, H., Green, A. G., 2004. Experimental design: Electrical resistivity data sets that provide optimum subsurface information. Geophysics 69 (1), 120–139.

Tabbagh, J., Samouelian, A., Tabbagh, A., Cousin, I., 2007. Numerical modelling of direct current electrical resistivity for the characterisation of cracks in soils. Journal of Applied Geophysics 62 (4), 313–323.

Tada, N., Hayashi, Y., Kitamura, T., Ohtani, R., 1997. Analysis on the applicability of direct current electrical potential method to the detection of damage by multiple small internal cracks. International Journal of Fracture 85 (1), 1–9.

Talsma, T., 1977. A note on the shrinkage behaviour of a clay paste under various loads. Australian Journal of Soil Research 15, 275–277.

Tanton, T. W., Armstrong, A. S. B., Rycroft, D. W., 1996. Movement of water in restructured saline and sodic clay topsoils under a rainfall simulator. Agricultural Water Management 29 (3), 255–265.

Taylor, R. W., Fleming, A. H., 1988. Characterizing jointed systems by azimuthal resistivity surveys. Ground Water 26 (4), 464–474.

Tempany, H. A., 1917. The shrinkage of soils. The Journal of Agricultural Science 8 (3), 312–330.

Topp, G. C., Davis, J. L., 1981. Detecting infiltration of water through soil cracks by time-domain reflectometry. Geoderma 26 (1-2), 13–23.

Trewin, D., 2006a. Water account Australia 2004-05, ABS catalogue no. 4610.0. Tech. rep.

Trewin, D., 2006b. Water use on Australian farms 2004-2005, ABS catalogue no. 4618.0. Tech. rep.

Tuong, T., Cabangon, R., Wopereis, M., 1996. Quantifying flow processes during land soaking of cracked rice soils. Soil Science Society of America Journal 60 (3), 872–879.

Van Stiphout, T., Van Lanen, H., Boersma, O., Bouma, J., 1987. The effect of bypass flow and internal catchment of rain on the water regime in a clay loam grassland soil. Journal of Hyrodology 95 (1-2), 1–11.

Vervoort, W., Silburn, M., Kirby, M., 2003. Near surface water balance in the northern Murray Darling basin. Water Science and Technology 48 (7), 207–214.

Vogel, H. J., Hoffmann, H., Roth, K., 2005. Studies of crack dynamics in clay soil - I. Experimental methods, results, and morphological quantification. Geoderma 125 (3-4), 203–211.

Waller, P., Wallender, W., 1993. Changes in cracking, water content, and bulk density of salinized swelling clay field soils. Soil Science 156 (6), 414–423.

Watson, K. A., Barker, R. D., 1999. Differentiating anisotropy and lateral effects using azimuthal resistivity offset Wenner soundings. Geophysics 64 (3), 739–745.

Watson, K. A., Barker, R. D., 2005. Modelling azimuthal resistivity sounding over a laterally changing resistivity subsurface. Near Surface Geophysics 3 (1), 3–11.

Wells, R. R., DiCarlo, D. A., Steenhuis, T. S., Parlange, J. Y., Romkens, M. J. M., Prasad, S. N., 2003. Infiltration and surface geometry features of a swelling soil following successive simulated rainstorms. Soil Science Society of America Journal 67 (5), 1344–1351.

White, E. M., 1970. Giant desiccation cracks in central South-Dakota soils. Soil Science 106-111 (1), 71–73.

White, E. M., 1972. Soil-desiccation features in South-Dakota depressions. Journal of Geology 80 (1), 106–111.

White, E. M., 2001. Comments on "Using surface crack spacing to predict crack network geometry in swelling soils". Soil Science Society of America Journal 65 (5), 1573–1674.

Wilkinson, P. B., Meldrum, P. I., Chambers, J. E., Kuras, O., Ogilvy, R. D., 2006. Improved strategies for the automatic selection of optimized sets of electrical resistivity tomography measurement configurations. Geophysical Journal International 167 (3), 1119–1126.

Wopereis, M. C. S., Bouma, J., Kropff, M. J., Sanidad, W., 1994. Reducing bypass

flow-through a dry, cracked and previously puddled rice soil. Soil & Tillage Research 29 (1), 1–11.

Xu, B. W., Noel, M., 1993. On the completeness of data sets with multielectrode systems for electrical-resistivity survey. Geophysical Prospecting 41 (6), 791–801.

Yasuda, H., Berndtsson, R., Persson, H., Bahri, A., Takuma, K., 2001. Characterizing preferential transport during flood irrigation of a heavy clay soil using the dye Vitasyn Blau. Geoderma 100 (1-2), 49–66.

Zein el Abedine, A., Robinson, G., 1971. A study on cracking in some vertisols of the Sudan. Geoderma 5 (3), 229–241.

Zhe, J. P., Greenhalgh, S., Marescot, L., 2007. Multichannel, full waveform and flexible electrode combination resistivity-imaging system. Geophysics 72 (2), F57–F64.

Appendix A

Current Flow near the Ground Surface

In a homogeneous and isotropic space, current flows radially from the source in all directions so as to define a spherical surface at each distance r. If the electrodes are located on the ground surface, current flow is restricted to the lower half of the sphere, as air has an infinite electrical resistance. This leads to hemi-spherical current expansion. For subsurface measurements the current is no longer expanding hemi-spherical. The shape of the body of soil that is conducting the current depends on the burying depth of the electrodes and lies somewhere between a hemi-sphere and a sphere. The varying distance to the air-ground interface needs to be incorporated into the calculation of ρ_a.

The manner in which current travels through the ground can be compared to the nature of light rays that spread through space. For example, current density and light intensity both decrease inversely proportional to the square of the distance from their point sources. Due to this similarity, optics has been used to illustrate the flow of electrical current (Keller and Frischknecht, 1966). The optical analogy to the interface between conducting soil and non conducting air is a fully reflecting mirror. If a light source is positioned at point C_1 at a distance h below the mirror an observer at point P_1 would see two light sources, one at point C_1 and one at point $C_1^{'}$ (Figure A.1). The

light intensity J of the two light sources at P_1 would be inversely proportional to the square of $r_{P_1C_1}$ and $r_{P_1C_1^{'}}$.

Returning to Ohm's Law and replacing the light source at C_1 with a current source and the light intensity with the current density gives

$$J_{P_1} = \frac{I}{4\pi r^2_{P_1C_1}} + \frac{I}{4\pi^2_{P_1C_1^{'}}} \tag{A.1}$$

for the light intensity and

$$E_{P_1} = J_{P_1}\rho = \frac{I\rho}{4\pi r^2_{P_1C_1}} + \frac{I\rho}{4\pi r^2_{P_1C_1^{'}}} \tag{A.2}$$

for the electric field intensity. The potential at point P_1 is therefore

$$\phi = \int_{r_{P_1C_1}}^{\infty} E_{r_{P_1C_1}} dr_{P_1C_1} + \int_{r_{P_1C^{'}_1}}^{\infty} E_{r_{P_1C^{'}_1}} dr_{P_1C_1^{'}} = \frac{I\rho}{4\pi r_{P_1C_1}} + \frac{I\rho}{4\pi r_{P_1C_1^{'}}}. \tag{A.3}$$

Including this correction for the influence of C_1 into the calculation of the potential difference between P_1 and P_2 that is described in Section 2.2.2 will lead to the calculation of ρ_a values that include the influence of the ground surface.

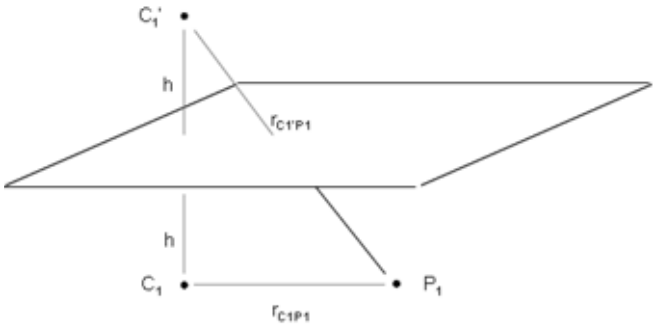

Figure A.1: Optical analogy to the interface between conducting soil and non conducting air.

Appendix B

Previous Electrode String Designs

On the first probe, the diameter of the electrode rings was only 28 mm, and the electrode diameter therefore did not significantly exceed the diameter of the plastic tube that separated the electrodes (Figure B.1a and b). This made taking the probes out of the soil easier than it is with the present design. However, it had the disadvantage that the electrical contact was lost at some electrodes, as the shrinking soil during drying moved away from the electrodes. The electrodes used in the laboratory and the field hence had a diameter of 38 mm and therefore stayed in contact with the shrinking soil for longer.

Instead of the fibreglass core that was used for the final field probes, the earlier probes used in the laboratory had a core consisting of a hollow plastic tube. This allowed leading the cables through the centre of the probes instead of through holes drilled into the electrodes. However, this string design was not sturdy enough to withstand the manual handling during deemployment of the probes. Therefore the sturdy and non conducting fibreglass core was introduced. This change also required the introduction of holes in the electrode rings to lead the cables along the strings.

The ring electrodes for the probes used in the laboratory were made from brass. While brass electrodes are economical to manufacture and have a low material related measurement error (Labrecque and Daily, 2008), it was found that exposure to the highly reactive clay soils caused rapid corrosion of the electrodes (Figure B.1b and c)

(a) (b) (c)

Figure B.1: a) first probe design with 28 mm diameter probes; b) build up on brass electrode due to corrosion process; c) build up on brass electrode due to corrosion (left) and brass electrode after sanding to remove build up.

and thus a decay of the of electrical contact over time. Electrodes for the field probes were therefore made from stainless steel grade 316, which provides a good balance between material related measurement error and corrosion resistance (Labrecque and Daily, 2008).

Taking apart the electrode strings after removal from the first field experiment showed that the silicon fill that was used to water prove the probes had not successfully filled the entire space around the insulated wires (Figure B.2a-c). To allow controlled silicon filling of the strings, a clear outer tube was used for probes of the second field experiment. Furthermore, corrosion of the electrical cables was observed under the silicon fill of the dismantled probes (Figure B.2d-e). To avoid corrosion, non-corrosive and adhesive free silicon was used in the final probe design.

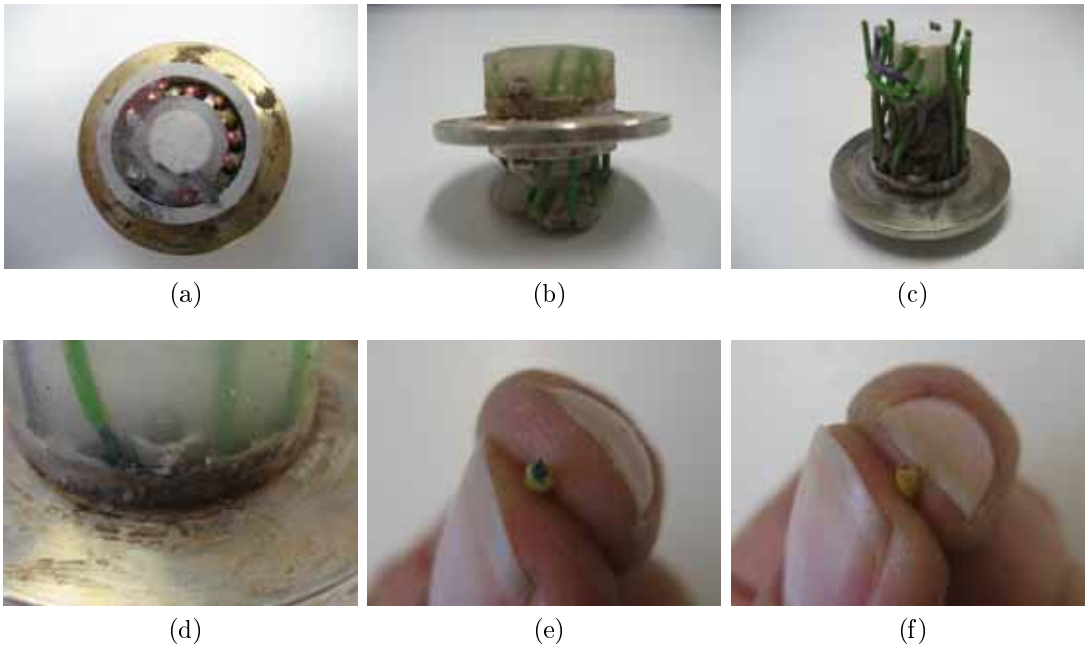

(a) (b) (c)

(d) (e) (f)

Figure B.2: A) top view on a probe section after cutting of the probe, the silicon is only partly covering the void around the cables; B) side view on probe section with the outer plastic tubing removed, the top is section is covered with silicon while the bottom section is not; C) the top electrode of an electrode string, silicon cover failed completely for all top sections; D) green build up around the cable at the connection to the electrode; E) cable that shows green build up due to corrosion; F) a freshly cut cable for comparison.